

Time-Varying Frequency Selective IQ Imbalance Estimation and Compensation

Durga Laxmi Narayana Swamy Inti

Thesis submitted to the Faculty of the
Virginia Polytechnic Institute and State University
in partial fulfillment of the requirements for the degree of

Master of Science
In
Electrical Engineering

A. A. (Louis) Beex, Chair
R. Michael Buehrer
Harpreet S. Dhillon

May 8, 2017

Blacksburg, VA

Keywords: Direct-Down Conversion Systems, IQ Imbalance, Blind Equalization,
Adaptive Filtering, Image Rejection

© 2017 Durga Laxmi Narayana Swamy Inti

Time-Varying Frequency Selective IQ Imbalance Estimation and Compensation

Durga Laxmi Narayana Swamy Inti

ABSTRACT

Direct-Down Conversion (DDC) principle based transceiver architectures are of interest to meet the diverse needs of present and future wireless systems. DDC transceivers have a simple structure with fewer analog components and offer low-cost, flexible and multi-standard solutions. However, DDC transceivers have certain circuit impairments affecting their performance in wide-band, high data rate and multi-user systems.

IQ imbalance is one of the problems of DDC transceivers that limits their image rejection capabilities. Compensation techniques for frequency independent IQI arising due to gain and phase mismatches of the mixers in the I/Q paths of the transceiver have been widely discussed in the literature. However for wideband multi-channel transceivers, it is becoming increasingly important to address frequency dependent IQI arising due to mismatches in the analog I/Q lowpass filters.

A hardware-efficient and standard independent digital estimation and compensation technique for frequency dependent IQI is introduced which is also capable of tracking time-varying IQI changes. The technique is blind and adaptive in nature, based on the second order statistical properties of complex random signals such as properness/circularity.

A detailed performance analysis of the introduced technique is executed through computer simulations for various real-time operating scenarios. A novel technique for finding the optimal number of taps required for the adaptive IQI compensation filter is proposed and the performance of this technique is validated. In addition, a metric for the measure of properness is developed and used for error power and step size analysis.

Time-Varying Frequency Selective IQ Imbalance

Estimation and Compensation

Durga Laxmi Narayana Swamy Inti

GENERAL AUDIENCE ABSTRACT

A wireless transceiver consists of two major building blocks namely the RF front-end and digital baseband. The front-end performs functions such as frequency conversion, filtering, and amplification. Impurities because of deep-submicron fabrication lead to non-idealities of the front-end components which limit their accuracy and affect the performance of the overall transceiver.

Complex (I/Q) mixing of baseband signals is preferred over real mixing because of its inherent trait of bandwidth efficiency. The I/Q paths enabling this complex mixing in the front-end may not be exactly identical thereby disturbing the perfect orthogonality of in-phase and quadrature components leading to IQ Imbalance. The resultant IQ imbalance leads to an image of the signal formed at its mirror frequencies. Imbalances arising from mixers lead to an image of constant strength whereas I/Q low-pass filter mismatches lead to an image of varying strength across the Nyquist range. In addition, temperature effects cause slow variation in IQ imbalance with time.

In this thesis a hardware efficient and standard-independent technique is introduced to compensate for performance degrading IQ imbalance. The technique is blind and adaptive in nature and uses second order statistical signal properties like circularity or properness for IQ imbalance estimation.

The contribution of this work, which gives a key insight into the optimal number of taps required for the adaptive compensation filter improves the state-of-the-art technique. The performance of the technique is evaluated under various scenarios of interest and a detailed analysis of the results is presented.

ACKNOWLEDGEMENTS

Mere thanks in few words would be highly inadequate to express my gratitude to Dr. A. A. (Louis) Beex for his exemplary guidance and encouragement during the course of these two years. I could not have imagined having a better advisor and mentor for my master's study. I would like to specially thank him for his time that he spent with me in analyzing issues and sharing various perspectives which is a great learning experience. The joy and enthusiasm he has for the subject at his age is contagious and motivational which will come long way with me.

My sincere thanks to Dr. Rich Holley of Innovative Computer Engineering (ICE) for encouraging and supporting IQI research in the Digital Signal Processing Research Laboratory (DSPRL), Wireless@VT, ECE, Virginia Tech.

I thank Dr. R. Michael Buehrer and Dr. Harpreet S. Dhillon for kindly agreeing to be part of my thesis committee and giving their valuable inputs. I am grateful to Remi Gurski and Dr. Swaroop Venkatesh of Qualcomm for offering me the summer and fall internship opportunities in their groups and leading me working on diverse exciting projects.

Besides, I would like thank my lab-mates and PhD fellows Karim Said and Tamoghna Roy for their insightful comments and enriching discussions. I cannot thank enough Ravi Teja Pulugurtha for his invaluable suggestions and wise counsel. Special thanks to my close friends for their best wishes and encouragement.

Needless to say, none of this would have been possible without the love and blessings of my parents. Special mention to my younger brother for always stretching my limits and lifting up my spirits with his innate sense of humor. Undoubtedly, it is with their endless support and undeterred faith in my abilities I am able to accomplish this today.

TABLE OF CONTENTS

Abstract.....	ii
General Audience Abstract.....	iii
Acknowledgements.....	iv
List of Figures.....	vii
List of Tables.....	x
List of Abbreviations.....	xi
Chapter 1 Introduction.....	1
1.1 Background.....	1
1.2 Objective.....	2
1.3 Organization.....	3
Chapter 2 Receiver Architectures.....	4
2.1 Super-Heterodyne Architecture.....	4
2.2 Zero-IF Architecture.....	6
2.3 Low-IF Architecture.....	7
2.4 RF/Band-Pass Sampling Architecture.....	9
2.5 Summary.....	11
Chapter 3 IQ Modeling and Image Rejection in Wireless Receivers.....	12
3.1 Real and Complex Signals.....	12
3.2 Bandpass Transmission.....	14
3.3 Ideal Down-Conversion.....	16
3.3 Frequency Independent IQ Imbalance Model.....	17
3.4 Frequency Dependent IQ Imbalance Model.....	20
3.5 Image Rejection Ratio.....	24
3.6 Multiple IF Signal Model.....	26
3.7 IQ Imbalance Effect on OFDM Signal.....	27

Chapter 4	IQ Imbalance Estimation and Compensation Techniques	29
4.1	Overview of Communication System Impairments	29
4.2	Digital Estimation and Compensation Using Test Tones	31
4.3	Digital Estimation and Compensation Using Pilots	32
4.4	Digital Estimation and Compensation Using Statistical Signal Properties	33
4.5	Scenario of Interest.....	34
Chapter 5	Blind-Adaptive Estimation and Compensation	35
5.1	Second Order Statistical Signal Properties.....	35
5.2	Stationarity of Signals	36
5.2	Circularity and Properness	37
5.3	Properness in the Context of Multicarrier IF Signals.....	39
5.4	Effects of Non-idealities on Properness	41
5.5	Theoretical Optimal Solution	47
5.6	Adaptive Filter Model	51
5.7	Image Rejection Ratio after Adaptive Filter	55
Chapter 6	Performance Simulations and Analysis	56
6.1	IQ Imbalance Parameters	56
6.2	Operating Signal Model	57
6.3	Impact of IQ Imbalance on Signal Constellation	59
6.4	1-tap and 3-Tap AF Performance Comparison	62
6.5	Optimal Filter Performance.....	66
6.6	Equalization for the Distortion Component	70
6.7	Illustration using White Gaussian Noise	73
6.8	Time-Varying IQ Imbalance	74
6.9	Error Metric Analysis	75
6.10	Illustration using Sinusoidal Inputs.....	80
6.11	Illustration using Impulse Invariant Filter Models.....	89
Chapter 7	Summary and Scope of Future Work	98
References	99

LIST OF FIGURES

Figure 2-1. Super-Heterodyne Receiver Architecture.....	5
Figure 2-2. Zero-IF Receiver Architecture.....	6
Figure 2-3. Low-IF Receiver Architecture.....	8
Figure 2-4. RF / Band-Pass Sampling Receiver Architecture.....	10
Figure 3-1. Magnitude Spectrum of a) Real and b) Complex Signals.....	13
Figure 3-2. Magnitude Spectra of Baseband and Bandpass Signals.....	14
Figure 3-3. Bandpass Transmission.....	16
Figure 3-4. Ideal Down-Conversion.....	17
Figure 3-5. Frequency Independent IQ Imbalance Model.....	18
Figure 3-6. Down Conversion in the presence of IQ Imbalance.....	19
Figure 3-7. Frequency Dependent IQ Imbalance Model.....	20
Figure 3-8. Simplified Frequency Dependent IQ Imbalance Model.....	23
Figure 3-9. Image Rejection Ratio (Magnitude).....	25
Figure 3-10. Image Rejection Ratio (Phase).....	25
Figure 3-11. IQ Imbalance Effect on Multiple IF Signal.....	26
Figure 3-12. IQ Imbalance Effect on OFDM Signal.....	27
Figure 4-1. Wireless Communication Transmitter and Receiver Impairment Model.....	30
Figure 5-1. Widely Linear IQI Compensator.....	49
Figure 5-2. Adaptive IQ Imbalance Compensator.....	53
Figure 6-1. Front-end IRR and I/Q Imbalance Filters.....	57
Figure 6-2. Operating Signal Model.....	58
Figure 6-3. Signal and Image Strengths due to IQ Imbalance.....	58
Figure 6-4. Effect of Gain and Phase Imbalances.....	60
Figure 6-5. Constellation of Signal-A at 20 dB SNR with IQI.....	61
Figure 6-6. Constellation of Signal-B at 20 dB SNR with IQI.....	62
Figure 6-7. IRR after 1-tap and 3-tap Adaptive IQI Compensators.....	63
Figure 6-8. Constellation of Signal-B after 1-tap Adaptive IQIC.....	64

Figure 6-9. Constellation of Signal-B after 3-tap Adaptive IQIC.....	64
Figure 6-10. SER Comparison of 1-tap and 3-tap Adaptive IQICs.....	65
Figure 6-11. Unit Impulse Response and Pole-Zero Plot of Optimal Filter.....	66
Figure 6-12. IRR after Optimal IQIC.....	67
Figure 6-13. SER of Optimal IQIC for 16-QAM.....	68
Figure 6-14. Adaptive vs Optimal Filter Coefficients.....	69
Figure 6-15. QPSK SER Performance.....	70
Figure 6-16. 64-QAM SER Performance.....	71
Figure 6-17. 64-QAM SER Performance after Distortion Compensation.....	72
Figure 6-18. IRR Response of Adaptive IQIC Operating on White Gaussian Noise.....	73
Figure 6-19. 3-tap AF Coefficients under Time-Varying IQI.....	74
Figure 6-20. IRR changes under Time-Varying IQI.....	75
Figure 6-21. Measure of Properness.....	76
Figure 6-22. Error Power of Fixed and Variable Step Size Adaptive Filters.....	78
Figure 6-23. Step Sizes of Fixed and Variable Step Size Adaptive Filters.....	78
Figure 6-24. Filter Coefficients of Fixed and Variable Step Size Adaptive Filters.....	79
Figure 6-25. Sinusoids Before (top) and After (bottom) IQ Imbalance.....	80
Figure 6-26. IRR Performance with Sinusoidal Input.....	81
Figure 6-27. Sinusoids after 3-tap (top) and Optimal (bottom) IQI Compensators.....	82
Figure 6-28. Modified IQ Imbalance Filters.....	83
Figure 6-29. Unit Impulse Response and Pole-Zero Plot of Optimal Filter.....	84
Figure 6-30. Image Strength Variations with Increase in Number of Taps.....	85
Figure 6-31. Average IRR vs Number of Taps.....	86
Figure 6-32. 16-QAM SER with 3-tap and 5-tap Adaptive IQI Compensators.....	87
Figure 6-33. IRR after 3-tap and 5-tap Adaptive IQI Compensators.....	88
Figure 6-34. I/Q Imbalance Filters Using Impulse Invariant Method.....	89
Figure 6-35. Sinusoids after IQI (top) and after 1-tap FI IQI Compensator (bottom).....	90
Figure 6-36. Sinusoids after 3-tap (top) and after 6-tap FD IQI Compensators (bottom).....	90
Figure 6-37. IRR Values with Adaptation on 6-Sinusoidal Input.....	91
Figure 6-38. Magnitude Response of IQI Compensator.....	93
Figure 6-39. Zoomed Magnitude Response of IQI Compensator.....	93

Figure 6-40. Phase Response of IQI Compensator.....	94
Figure 6-41. Zoomed Phase Response of IQI Compensator.....	94
Figure 6-42. Magnitude Response of Impulse Invariant System.....	95
Figure 6-43. Zoomed Magnitude Response of Impulse Invariant System.....	96
Figure 6-44. Phase Response of Impulse Invariant System.....	97

LIST OF TABLES

Table 2-1.	Comparison of Various Receiver Architectures	11
Table 4-1.	Various RF Components and their Impairments	29
Table 6-1.	Coefficient Values of FIR Approximated Optimal Filter	67
Table 6-2.	Sinusoid Signal to Image Strengths vs Front-end IRR	81
Table 6-3.	IRR Flatness Metric vs Number of Taps	86

LIST OF ABBREVIATIONS

ACF	Autocorrelation Function
ADC	Analog to Digital Converter
AF	Adaptive Filter
AWGN	Additive White Gaussian Noise
BPSK	Binary Phase Shift keying
CACF	Complementary Autocorrelation Function
CFO	Carrier Frequency Offset
DC	Direct Current
DDC	Direct-Down Conversion
EVM	Error Vector Magnitude
FD	Frequency Dependent
FI	Frequency Independent
FM	Frequency Modulation
IC	Integrated Circuit
ICI	Inter Carrier Interference
IF	Intermediate Frequency
IQI	In-Phase Quadrature-Phase Imbalance
IQIC	In-Phase Quadrature-Phase Imbalance Compensator
IRR	Image Rejection Ratio
LMS	Least Mean Squares
LNA	Low-Noise Amplifier
LO	Local Oscillator
OFDM	Orthogonal Frequency Division Multiplexing
OF	Optimal Filter
PA	Power Amplifier
PSK	Phase Shift Keying
QAM	Quadrature Amplitude Modulation

QPSK	Quadrature Phase Shift Keying
RF	Radio Frequency
RLS	Recursive Least Squares
SAW	Surface Acoustic Wave
SDR	Software Defined Radio
SER	Symbol Error Rate
SNR	Signal to Noise Ratio
SOS	Second Order Stationary
VS	Variable Step Size
WSS	Wide Sense Stationary

CHAPTER 1 INTRODUCTION

1.1 Background

The wireless communications market has seen an unprecedented growth from the first generation analog 1G to the upcoming 5G cellular technology [1]. The wireless paradigm has changed; the aim is no longer to just improve the quality of voice/data transfers but to give the user access to the new global reality of communication ubiquity. From the technology point of view, the higher data rates are achieved through novel, sophisticated communication theory techniques and advances in Integrated Circuit (IC) design [2].

In spite of radical developments there are still challenges to provide enhanced services in the emerging wireless standards [3, 4]. Meeting the ambitious goals of these new standards implies increasing demand on the underlying hardware [5]. In addition, multi-standard compatibility on a single chip and the need for smaller, flexible, low-power and cost-effective devices further increases the performance requirements for transceivers [6].

In terms of hardware, the major limitations come from the analog components in the radio front-end compared to the digital baseband [7]. Unlike digital hardware there is only a finite amount of accuracy that can be achieved by Analog/RF components. The current design strategies are therefore along the lines of reducing the analog components to the maximum extent possible and to move the ADCs as close to the antenna as possible [8]. In this way, more and more functionalities can be implemented in the digital domain with greater ease and re-configurability [9].

Considering the requirements and limitations of the RF/analog circuitry, the traditional super-heterodyne architecture is not a practical choice for multi-standard and low cost transceivers. Instead, simplified and flexible front-end architectures like Direct-Down Conversion (DDC) systems are of interest [10]. Although DDC systems have their own set of problems, the idea is to use effective and low-cost digital compensation techniques to mitigate them.

1.2 Objective

The earlier section iterated the importance of Direct-Down Conversion (DDC) systems for future multi-standard and cost-effective radios [11]. However, DDC system performance is limited by impairments like DC Offset, Phase Noise, Carrier Frequency Offset, IQ Imbalance and other Non-linearities. Although most of these are fundamental problems with any kind of RF architecture, IQ Imbalance and DC-offset are specific to the DDC systems [12].

IQ Imbalance and DC-Offset compensation techniques with respect to DDC systems are thoroughly studied and various aspects have been explored in the literature and industry [13, 14]. However, emerging standards/technologies come with greater challenges and demand enhanced techniques for better performance.

IQ Imbalance is the main interest in this thesis, so the problems corresponding to IQ Imbalance will be studied in detail. More specifically, the problems pertaining to wide-band transceivers and the time-varying nature of IQ Imbalance are addressed. The major focus will be on the receive path of the transceiver, equivalent techniques can be applied to the transmit path as well.

It is highly impossible to avoid the above-mentioned RF problems by proper system design, so they need to be accepted to a certain extent and then further compensated digitally [7]. So, the major objective of the thesis is to develop standard independent and hardware efficient digital estimation and compensation techniques for the performance degrading IQ Imbalance impairment and validate the same through computer simulations under real-time operating conditions. This in a way facilitates the end goal of realizing cheaper, multi-standard, and wide-band radio front-ends.

1.3 Organization

The thesis consists of five major chapters, each aimed at addressing one important aspect of the IQ imbalance problem. Chapter 2 starts with a brief overview of various RF receiver architectures, focusing on their implementation details and performance bottlenecks. The chapter ends by summarizing the advantages and disadvantages of these receiver architectures.

Chapter 3 starts with the real and complex representation of signals and then introduces the concept of complex mixing (I/Q mixing) which is the major fundamental building block in I/Q architectures. The IQ Imbalance (IQI) problem encountered in non-ideal I/Q mixing is then highlighted and the theory behind various aspects of IQI described in detail. The IQ Imbalance problem analysis is further extended to multi-channel and OFDM systems.

Chapter 4 starts with a brief mention of other RF impairments that coexist with IQ imbalance. Further, a detailed analysis of different IQ Imbalance estimation and compensation techniques covered in the literature to date is presented.

Chapter 5 starts with a brief review of second order statistics of complex random signals. The concepts of circularity and properness are introduced and explained as applied to this thesis. The next section of the chapter focuses on the effects of different RF impairments on circularity/properness. The concept of widely linear filtering is introduced in the context of distortion due to IQ imbalance, followed by a presentation of the widely linear adaptive filter model that facilitates blind IQ Imbalance estimation and compensation.

In Chapter 6 the performance of the various aspects of the introduced technique is validated through computer simulations. Further a detailed analysis of the results under different operating scenarios is presented.

The thesis ends with Chapter 7 where the conclusion and scope of future work are presented.

CHAPTER 2 RECEIVER ARCHITECTURES

In wireless receivers, the Radio Frequency components that form the entry level block play a vital role in the performance and reliability of the system. Any unresolved issue pertaining to this first processing block may cause serious problems for subsequent blocks. So, it is important to choose a receiver front-end architecture that is less prone to problems and fits best for the targeted application. In addition, it must be economical, with good sensitivity (offering better signal-to-noise ratio at the receiver output for a signal of given power at its input), good selectivity (better ability to separate the signals in the desired band from the ones at unwanted frequencies), and lower power consumption. In this chapter, a brief overview of most commonly used architectures is presented, emphasizing their key advantages and major drawbacks [15, 16].

2.1 Super-Heterodyne Architecture

The super-heterodyne architecture shown in Fig. 2-1 is, until recently, the most commonly used architecture due to its superior performance.

In a super-heterodyne receiver, down-conversion is done in two stages. In the first stage, the received RF signal is coarse filtered by a bandpass filter, amplified by a Low Noise Amplifier (LNA) and then down-converted to an Intermediate Frequency (IF) by real mixing with the signal from a Local Oscillator (LO). In most cases, the mixer is preceded by a high-Q image reject (IR) filter to reduce the image frequency problems occurring in RF to IF translation.

In the second stage, the signal is passed through a channel select filter to remove the out of band energy and then brought down to baseband through complex down-conversion. The signal is further processed by Analog to Digital converters (ADCs) and then sent to digital demodulation and data-decoding.

Super-heterodyne receivers have been widely used in the past two decades, especially for high quality applications, because of their sensitivity and immunity to DC effects. The super-heterodyne receiver can also provide good selectivity as the components are mostly designed for fixed operating frequencies. There is also the inherent advantage of conveniently performing most of the operations at low IF rather than high RF frequencies.

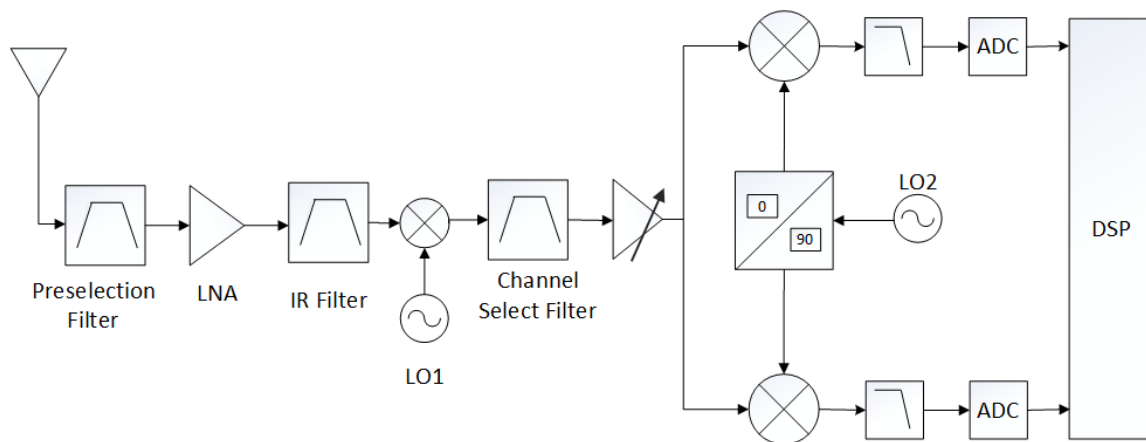


Figure 2-1. Super-Heterodyne Receiver Architecture

However, this architecture has a major disadvantage in terms of image frequency [2]. An image frequency is any second frequency that also down-converts to the same IF. This is undesirable because the noise and interference at the image frequency can potentially overwhelm the receiver. Sensitivity to the image frequency can be minimized by an image reject filter that precedes the mixer. The image reject and channel select filters used are typically implemented as high-Q discrete component filters such as Surface Acoustic Wave (SAW) or ceramic filters. Due to these discrete analog components, besides the increase in size and effective cost, on-chip integration is not possible. The off-chip placement of these filters is associated with a low filter input impedance, which then leads to increased drive requirements on the LNA preceding it.

Another drawback of the super-heterodyne receiver architecture is that despite of the additional complexity required for better performance, it works only for a particular channel thus limiting the receiver operating frequency band and making it very specific.

2.2 Zero-IF Architecture

The Zero-IF architecture also known as Homodyne or Direct-down conversion (DDC) receiver (Fig. 2-2) has been widely used recently and is becoming increasingly popular for implementing the emerging communication standards [11].

Unlike the super-heterodyne receiver, the DDC receiver converts the RF signal directly to baseband. The received signal at the antenna is passed through a broadband preselection filter for removing out-of-band energy and is then amplified by an LNA. The signal is then down converted to DC by I/Q mixers which have a phase delay of 90° between them and then further processed by ADCs and sent to digital baseband.

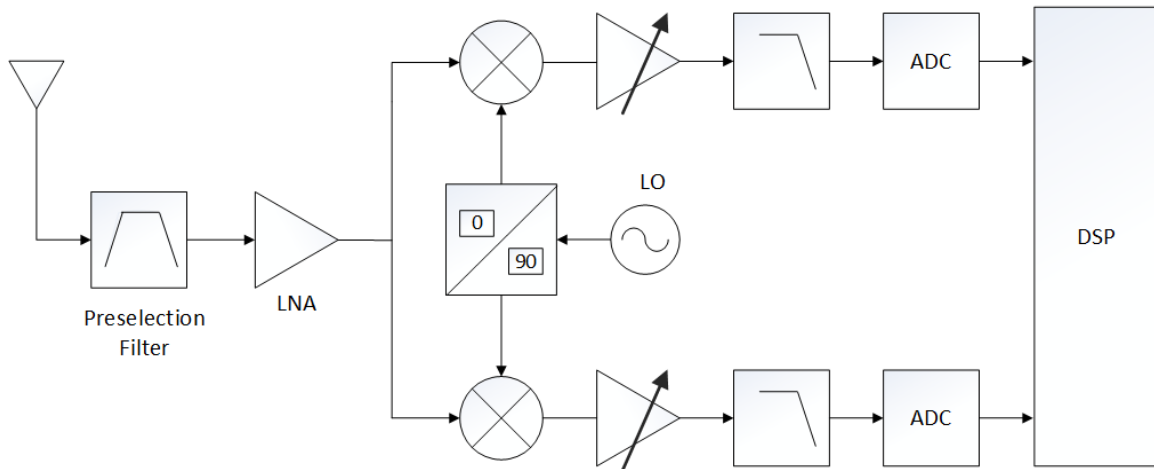


Figure 2-2. Zero-IF Receiver Architecture

The simple Zero-IF receiver structure eliminates the need for the high-Q image reject filters that are needed in the super-heterodyne receiver, thereby facilitating complete monolithic integration and reducing the severe requirements on the LNA of driving a low

impedance load. In addition, channel selection is done by simple low-pass filtering rather than by a high-Q band-pass filter.

Despite its simplicity, the DDC receiver has its own set of problems in terms of DC Offset, Flicker Noise, and IQ Imbalance.

Due to capacitive and substrate coupling there will be imperfect isolation between ports of the mixer, a small amount of signal from the LO port that will feed through to the input port of the LNA and mixer. This effect is known as “LO Leakage” and produces DC offsets in the mixer outputs and may cause saturations. Further, a strong interferer may leak through the mixer ports and appear as an additive signal component at the mixer LO port and mixing with itself, leading to a phenomenon known as “Self Mixing”. This effect also creates DC offset affecting the desired baseband signal [17].

Flicker noise, an inherent property of the devices in metal-oxide semiconductor implementations arising especially from the mixer, corrupts the baseband signal. The imperfections in the complex I/Q down-conversion due to finite precision of the analog hardware leads to imperfect rejection of the image component of the original signal; the latter problem is known as IQ Imbalance (IQI) and is discussed in detail in the next chapter.

2.3 Low-IF Architecture

The Low-IF architecture, shown in Fig. 2-3, digitizes the real bandpass channel at IF and performs quadrature frequency down-conversion to baseband in the digital domain. This is a hybrid of the super-heterodyne and DDC architectures and aims to combine the advantages of both. The received signal passes through a channel pre-selection filter at RF and is amplified by a LNA after which the signal is down-converted to a low IF using LO1. ADCs then convert the signal to the digital domain where quadrature down-conversion to baseband is done digitally using LO2. Additional signal processing is done to extract the required information.

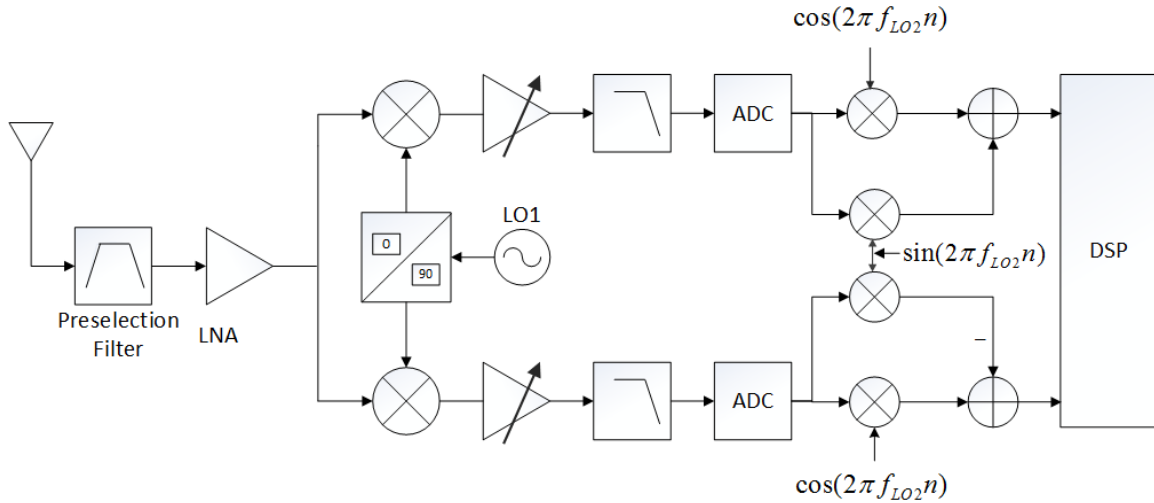


Figure 2-3. Low-IF Receiver Architecture

As the final translation to baseband is done in the digital domain, the Low-IF architecture is immune to LO leakage/mixing and therefore there are no DC offsets affecting the desired signal. Although expensive, on-chip integration is possible to some extent as the Low-IF architecture eliminates the high-Q discrete channel select filters.

However, the Low-IF receiver still suffers from image frequency and I/Q mismatch problems. The image rejection is either done in the digital domain or by image reject filters in the analog domain.

The major drawback of the Low-IF architecture is the high performance requirements on the ADCs. In the Low-IF architecture, the ADC power consumption is higher than in the super-heterodyne and DDC architectures as the ADCs need to operate on the IF signal rather than the signal at DC. In addition, operating at these IF levels makes ADCs more sensitive to clock-jitter (explanation in the next section) and increases the dynamic range requirements.

2.4 RF/Band-Pass Sampling Architecture

In the RF/Band-Pass Sampling architecture (Fig. 2-4), the received signal is first filtered by a tunable RF band-pass filter and then amplified using a wideband LNA. The signal is then converted to the digital domain by a high sampling rate ADC after which I/Q demodulation and further processing is done in the digital domain. All the previous architectures used analog circuitry to down-convert, whereas the RF/Band-Pass sampling structure down-converts the signal using intelligent sampling [18, 19]. This works on the principle that the entire energy from DC to the analog bandwidth of the ADC will be inherently folded back to the first Nyquist zone $[-f_s/2, f_s/2]$, so that the sampler does the down-conversion without the need for an explicit mixer. However the challenge is to extract the signal of interest in the presence of aliasing effects.

As most of the operations on the signal are done in the digital domain, the band-pass sampling approach is free from the impairments caused by the analog devices and improves accuracy. Further, as this architecture pushes the analog-to-digital conversion closer to the antenna, it increases receiver flexibility.

In addition, by choosing a calculated sampling frequency, it is possible to receive more than one RF signal at the same time. Another advantage of the RF/Band-Pass Sampling receiver is that the sampling frequency needed and the subsequent processing rate are proportional to the information bandwidth, rather than the carrier frequency.

However, there are many problems associated with directly sampling signals at GHz range. Although the latest ADCs have sampling rates up to 100 GSPS [20] they consume very high power. There is also a limit on the maximum bandwidth of the signal that can be efficiently sampled which is determined by the gate length of the active devices within ADCs.

In addition, the band-pass sampling architecture imposes tighter constraints on the RF band-pass filter as it plays a key role in system performance. Any unfiltered, out of band

signal/noise will alias onto the signal of interest in the first Nyquist zone and thus degrade SNR.

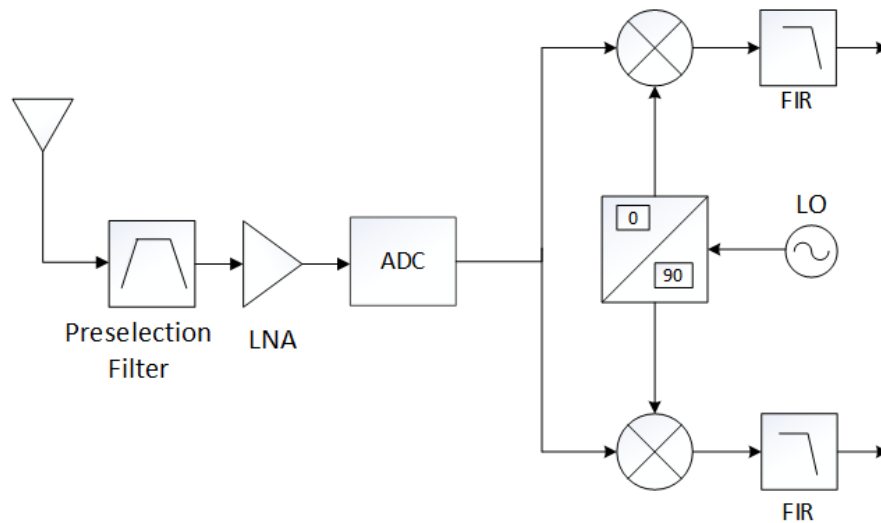


Figure 2-4. RF / Band-Pass Sampling Receiver Architecture

Sensitivity to clock jitter is another problem with the band-pass sampling architecture. Jitter can arise from various sources like frequency dividers, clock buffers, coupling effects, in addition to the internal aperture jitter of the ADC and causes variation in sampling times. This variation is coming from the error associated with the time at which the switch is opened in the sample and hold circuit of the ADC and this error is proportional to the magnitude of the jitter and the input signal slew rate. So, as the frequency of the input signal increases, the effect of jitter becomes more severe.

2.5 Summary

Every receiver architecture has its advantages and disadvantages as summarized in the table below. The choice as to which to use is therefore made depending on the target application.

Table 2-1. Comparison of Various Receiver Architectures

Architecture	Advantages	Disadvantages
Super-Heterodyne	<ul style="list-style-type: none"> - Performance - Less sensitive to DC offset 	<ul style="list-style-type: none"> - Image Frequency - High LNA requirements - Off-Chip high-Q filters - Complex Structure
Direct Down Conversion	<ul style="list-style-type: none"> - Simple Structure - On-chip integration 	<ul style="list-style-type: none"> - Less immune to DC effects - IQ Imbalance problem
Low-IF	<ul style="list-style-type: none"> - Immune to DC effects - Simple Structure 	<ul style="list-style-type: none"> - High ADC requirements. - Image Frequency - IQ Imbalance problem
RF/Band-Pass Sampling	<ul style="list-style-type: none"> - Immune to most of the analog impairments - Flexible 	<ul style="list-style-type: none"> - Clock Jitter - Power hungry ADCs

CHAPTER 3 IQ MODELING AND IMAGE REJECTION IN WIRELESS RECEIVERS

In-phase/Quadrature (I/Q) signal processing is one of the most widely used tools in communication system design because of its inherent trait of bandwidth efficiency. Although the I/Q representation is widely used to represent digital baseband signals and their operations, it also plays a key role in analog processing operations like frequency translation and the image rejection that are needed in the front-end of radio receivers [16, 21, 22].

3.1 Real and Complex Signals

Any communication signal can be represented as a variation with time t of some physical parameter and is denoted as $x(t)$. Similar to in other engineering fields, transform domains are used for convenient design and analysis of systems. The Fourier Transform is used in communications for relating $x(t)$ and its frequency domain equivalent $X(f)$.

The Fourier transform definition used here is:

$$X(f) = \int_{-\infty}^{\infty} x(t) e^{-j2\pi ft} dt \quad (3.1)$$

The corresponding inverse Fourier transform is defined as

$$x(t) = \frac{1}{2\pi} \int_{-\infty}^{\infty} X(f) e^{j2\pi ft} df \quad (3.2)$$

The Fourier transform can also be represented in terms of angular frequency $X(\Omega)$, where $\Omega = 2\pi f$. $X(f)$ will be the notation used throughout this thesis.

Signals can be majorly classified into two types: Real-Valued and Complex-Valued. Considering an $x(t)$ that is real-valued, its Fourier transform exhibits the following property.

$$X(f) = X^*(-f) \quad (3.3)$$

where $X^*(f)$ denotes the complex conjugate of $X(f)$.

The magnitude $|X(f)|$ is an even function of frequency and the phase $\angle X(f)$ is an odd function of frequency, so real-valued signals exhibit the spectral property of “conjugate symmetry” which will be referred to in short as “spectral symmetry.” The cartoon shapes in Fig. 3-1 will be used to distinguish between the spectra of real-valued and complex-valued time domain signals.

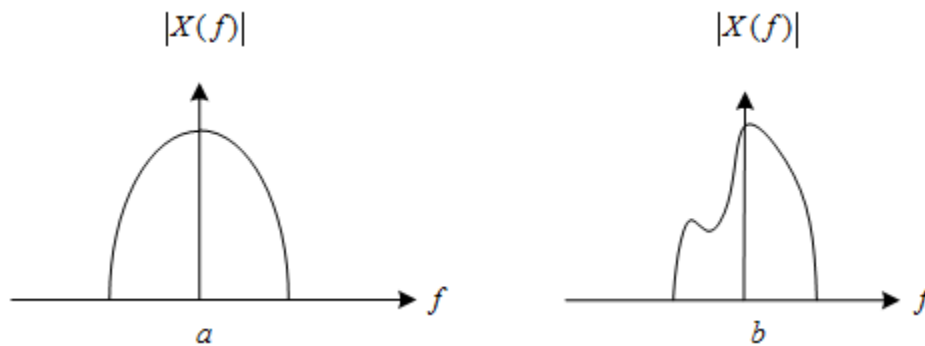


Figure 3-1. Magnitude Spectrum of a) Real and b) Complex Signals

Spectral symmetry might be a desirable property for applications like FM radio broadcasting as it facilitates single side band transmission but it is bandwidth inefficient for most commercial applications. A complex signal does not exhibit spectral symmetry and uses bandwidth more effectively. Although all signals that are physically transmitted are real in nature, a combination of them can be virtually interpreted as a complex-valued signal as shown below.

$$z(t) = z_I(t) + jz_Q(t) \quad (3.4)$$

where $z_I(t)$ and $z_Q(t)$ are two real-valued signals referred to as the In-Phase and Quadrature-Phase component respectively of the complex valued signal $z(t)$. As illustrated in Fig. 3-2a a complex-valued signal can fit two real-valued signals in the same bandwidth and thereby make more effective use of available resources whereas the real-valued signal represented in Fig. 3-2b occupies twice the bandwidth to fully transmit and recover the signal.

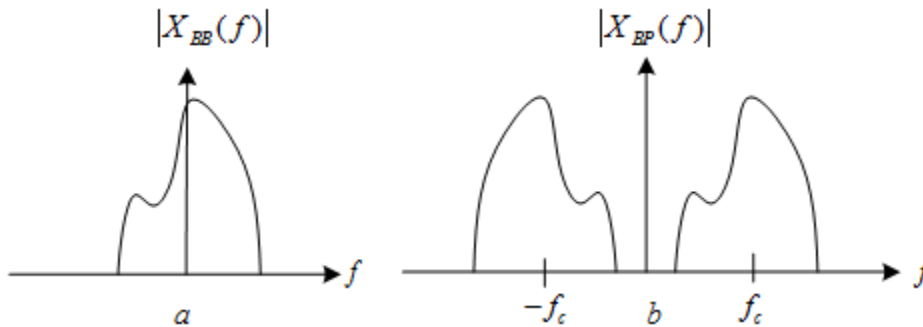


Figure 3-2. Magnitude Spectra of Baseband and Bandpass Signals

Generally in communication systems, low-pass baseband signals are represented in complex form which represents the real and imaginary parts of the signal and bandpass RF signals are real-valued. The transition from baseband to bandpass and vice versa is discussed in the next section.

3.2 Bandpass Transmission

Bandpass transmission is transmitting the signal of interest in the allotted Radio Frequency (RF) spectrum, so translating the desired baseband signal to the carrier frequency and vice-versa is one of the most important tasks of radio transceivers.

For this purpose two oscillator signals, $\cos(2\pi f_c t)$ and $\sin(2\pi f_c t)$, which have a phase difference of 90° , are used to modulate the real and imaginary components of the baseband signal $z(t) = z_I(t) + jz_Q(t)$ to the carrier frequency; this process is illustrated in Fig. 3-3. For convenience and analysis purposes these signals can be modeled as a complex oscillator $e^{j2\pi f_c t}$.

$$e^{j2\pi f_c t} = \cos(2\pi f_c t) + j \sin(2\pi f_c t) \quad (3.5)$$

The transmitted real-valued bandpass signal $r(t)$ can be represented in terms of the baseband signal $z(t)$ and carrier frequency oscillator as follows

$$\begin{aligned} r(t) &= \text{Re} \left[z(t) e^{j2\pi f_c t} \right] \\ &= z_I(t) \cos(2\pi f_c t) - z_Q(t) \sin(2\pi f_c t) \end{aligned} \quad (3.6)$$

The bandpass signal $r(t)$ can also be represented in terms of $z(t)$ and its conjugate $z^*(t)$ as

$$r(t) = \frac{1}{2} \left(z(t) e^{j2\pi f_c t} + z^*(t) e^{-j2\pi f_c t} \right) \quad (3.7)$$

The Fourier representation of the transmitted signal $r(t)$ is then

$$R(f) = \frac{1}{2} \left(Z(f - f_c) + Z^*(-f - f_c) \right) \quad (3.8)$$

where $Z(f)$ denotes the Fourier transform of $z(t)$.

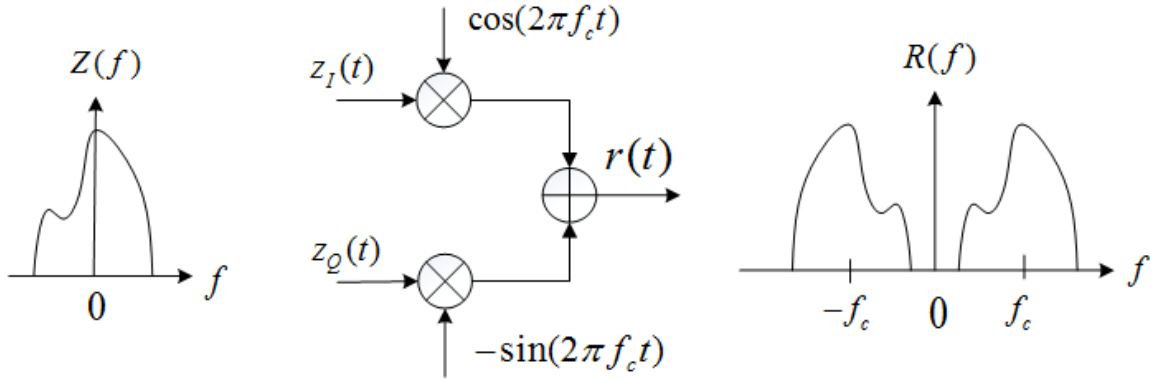


Figure 3-3. Bandpass Transmission

In the case of a Wide Sense Stationary (WSS) random signal, the frequency domain representation is given in terms of power spectra as follows

$$\Phi_R(f) = \frac{1}{4}(\Phi_z(f - f_c) + \Phi_z(-f - f_c)) \quad (3.9)$$

3.3 Ideal Down-Conversion

When everything is ideal at the receiver, the Local Oscillator signal can be modeled as

$$v(t) = \cos(2\pi f_c t) - j \sin(2\pi f_c t) \quad (3.10)$$

where $\cos(2\pi f_c t)$ and $\sin(2\pi f_c t)$ are real signals multiplied with signals from the real I and Q paths.

The down converted signal would thus be

$$\begin{aligned} r(t)v(t) &= [z(t)e^{j2\pi f_c t} + z^*(t)e^{-j2\pi f_c t}]e^{-j2\pi f_c t} \\ &= z(t) + z^*(t)e^{-j4\pi f_c t} \end{aligned} \quad (3.11)$$

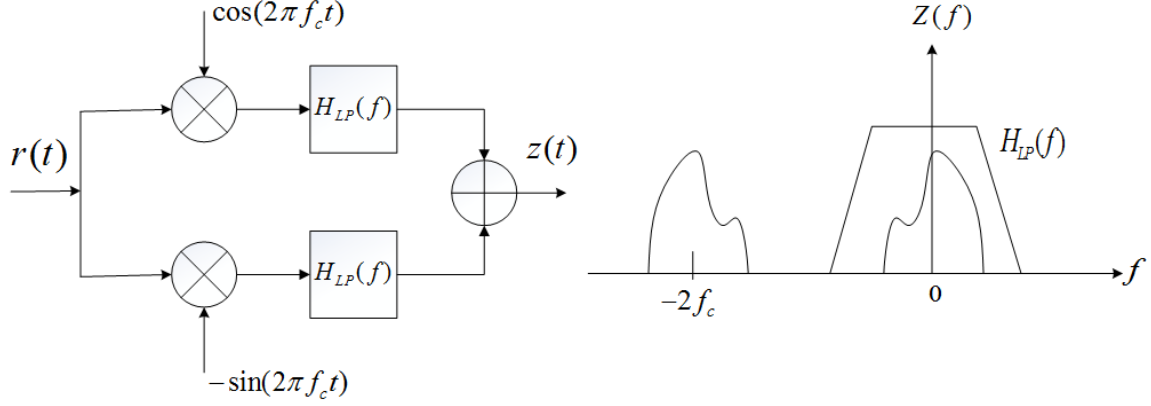


Figure 3-4. Ideal Down-Conversion

The component at the higher frequency is filtered out by the low-pass filter which leaves the original transmitted signal to be processed at baseband (Fig. 3-4).

3.3 Frequency Independent IQ Imbalance Model

As shown in the above section the ideal receiver oscillator signal is expected to be $\cos(2\pi f_c t) - j \sin(2\pi f_c t)$, however due to differences in the amplitude and phase on the I and Q paths of the radio receiver front-end arising from the LO oscillator and mixers (Fig. 3-5), the IQ imbalanced receiver oscillator signal can be modeled as follows

$$\tilde{v}(t) = l_1 \cos(2\pi f_c t + \phi_1) - j l_2 \sin(2\pi f_c t + \phi_2) \quad (3.12)$$

where l_1 and l_2 are the gains in the I and Q paths, ϕ_1 and ϕ_2 are the corresponding phases. Note that $\tilde{v}(t)$ can be rewritten as follows

$$\tilde{v}(t) = l_1 \left[\cos(2\pi f_c t + \phi_1) - j \left(l_2 / l_1 \right) \sin(2\pi f_c t + \phi_2 + \phi_1 - \phi_1) \right] \quad (3.13)$$

The relative gain (l_2 / l_1) and phase difference $(\phi_2 - \phi_1)$ are the parameters of interest for IQ imbalance calculations, so in order to simplify the notations we can assume

$l_1 = 1, l_2 = g, \phi_1 = 0$ and $\phi_2 = \phi$, substituting these values in (3.13), the receiver oscillator representation can be simplified as follows,

$$\tilde{v}(t) = \cos(2\pi f_c t) - jg \sin(2\pi f_c t + \phi) \quad (3.14)$$

Furthermore, $\tilde{v}(t)$ can be written in terms of complex phasors as follows,

$$\begin{aligned} \tilde{v}(t) &= \left(\frac{1 + ge^{-j\phi}}{2} \right) e^{-j2\pi f_c t} + \left(\frac{1 - ge^{j\phi}}{2} \right) e^{j2\pi f_c t} \\ &= k_1 e^{-j2\pi f_c t} + k_2 e^{j2\pi f_c t} \end{aligned} \quad (3.15)$$

where

$$\begin{aligned} k_1 &= \left(\frac{1 + ge^{-j\phi}}{2} \right), \\ k_2 &= \left(\frac{1 - ge^{j\phi}}{2} \right) \end{aligned} \quad (3.16)$$

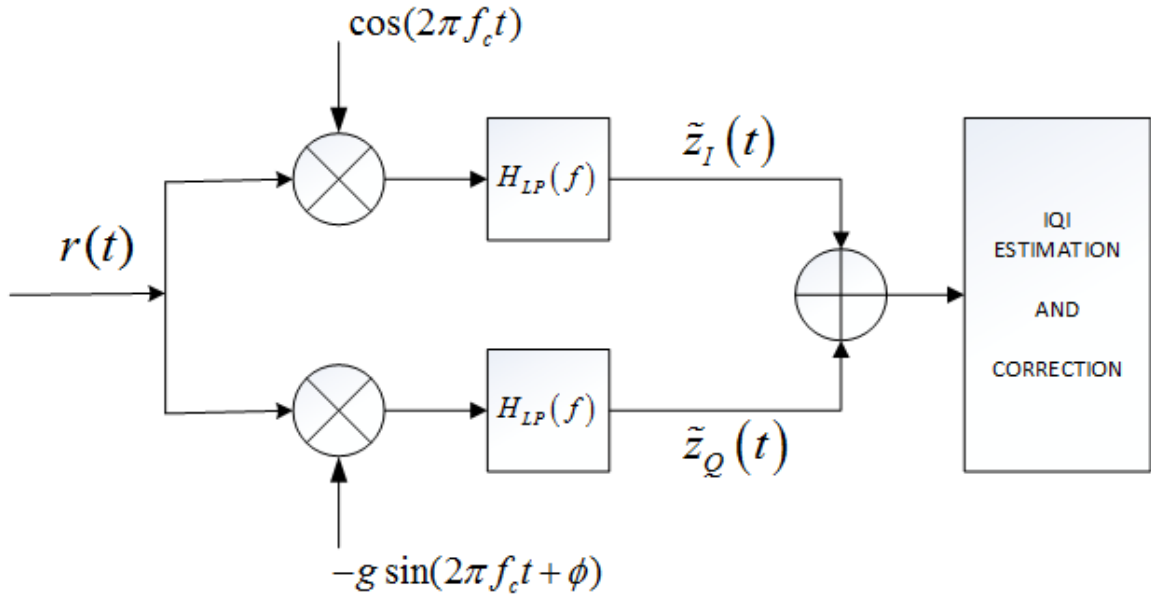


Figure 3-5. Frequency Independent IQ Imbalance Model

The signal at the output of the mixer stage is

$$\begin{aligned}
 \tilde{z}(t) &= r(t) \tilde{v}(t) \\
 &= \left(z(t) e^{j2\pi f_c t} + z^*(t) e^{-j2\pi f_c t} \right) \left(k_1 e^{-j2\pi f_c t} + k_2 e^{j2\pi f_c t} \right) \quad (3.17) \\
 &= k_1 z(t) + k_2 z^*(t) + k_1 z^*(t) e^{-j4\pi f_c t} + k_2 z(t) e^{j4\pi f_c t}
 \end{aligned}$$

Assuming ideal filtering of the double carrier frequency components

$$\tilde{z}(t) = k_1 z(t) + k_2 z^*(t) \quad (3.18)$$

where $\tilde{z}(t)$ is the received baseband signal, k_1 and k_2 are as described in (3.16).

The ratio of the power of the signal to the power of the generated image is defined as Image Rejection Ration (IRR) and is given by

$$\begin{aligned}
 M &= \frac{|k_1|^2}{|k_2|^2} \\
 &= \frac{1 + g^2 + 2g \cos \phi}{1 + g^2 - 2g \cos \phi} \quad (3.19)
 \end{aligned}$$

So unlike in the ideal case, we have an image component of potentially considerable strength corrupting the band of interest (Fig. 3-6).

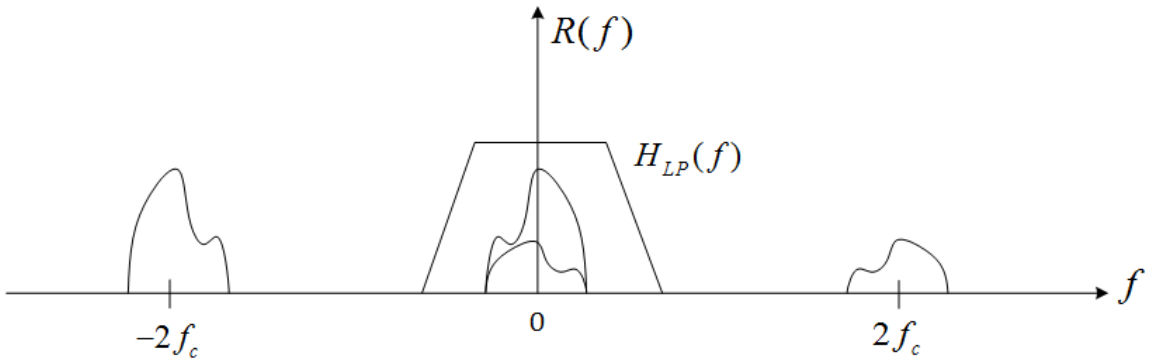


Figure 3-6. Down Conversion in the presence of IQ Imbalance

A similar sort of IQ imbalance might arise due to the analog components at the transmitter. However for the purposes of this thesis we assume that the transmitter is self-calibrated as this problem is specific to the transmitter hardware. The assumption that the transmitted signal is IQI calibrated is in line with contemporary system designs.

3.4 Frequency Dependent IQ Imbalance Model

The low-pass filters in the I and Q paths (Fig. 3-7) are not identical and have different gains, cutoff frequencies, and group delays. As a result of increases in operating bandwidth there will be increasingly tighter restrictions on these analog filters. For higher operating bandwidths the differences between these I and Q path filters will become more prominent and lead to increasingly more severe frequency selective effects on the desired signal. If the system is narrowband, the Frequency Dependent (FD) component can be ignored, but if the system is wideband – which is the case in most modern communication systems – the frequency selective part has to be estimated and compensated for. So, the overall IQ imbalance can be modeled as the sum of frequency independent components (due to mixers) and a frequency dependent component (due to the analog I and Q path filters).

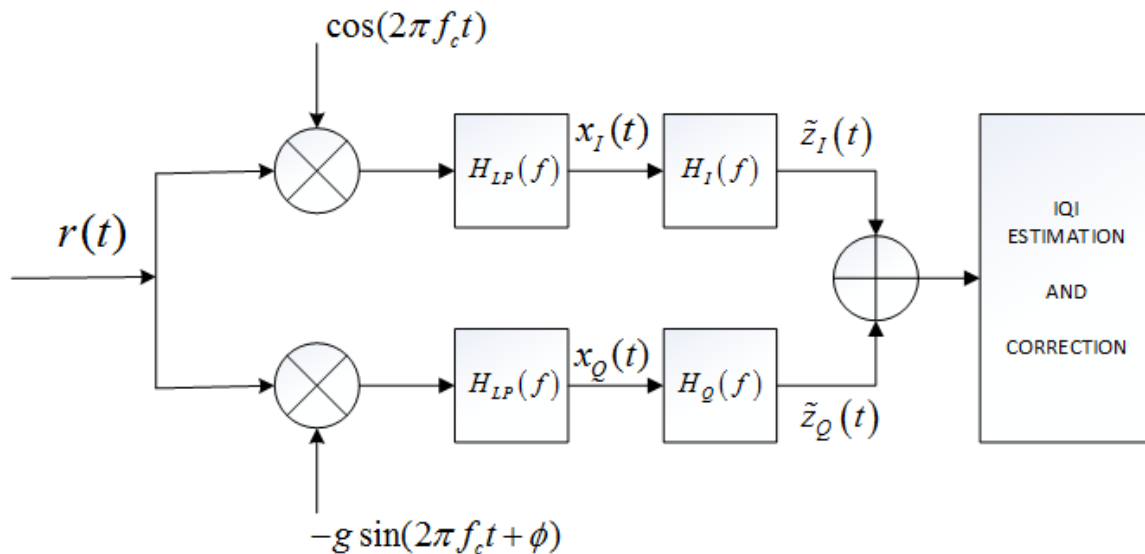


Figure 3-7. Frequency Dependent IQ Imbalance Model

Let $H_{LP}(f)$ be the low-pass filter response which is common for the I and Q paths, $H_I(f)$ and $H_Q(f)$ be the frequency response distortions of the common low-pass filter.

The frequency responses of the I and Q paths are thus modeled as follows:

$$\begin{aligned} H_{LPF,I}(f) &= H_{LP}(f)H_I(f) \\ H_{LPF,Q}(f) &= H_{LP}(f)H_Q(f) \end{aligned} \quad (3.20)$$

If for simplicity we consider $H_{LP}(f)=1$, the signal at the output of the common low-pass filter can be represented, using the result in (3.18), as

$$\begin{aligned} x(t) &= k_1 z(t) + k_2 z^*(t) \\ &= k_1 (z_I(t) + jz_Q(t)) + k_2 (z_I(t) + jz_Q(t))^* \end{aligned} \quad (3.21)$$

Substituting k_1 and k_2 from (3.16) in (3.21), $x(t)$ can be written as

$$x(t) = z_I(t) + j(g \cos(\phi) z_Q(t) - g \sin(\phi) z_I(t)) \quad (3.22)$$

The common low-pass filtered signal $x(t)$ can also be written in terms of its real and imaginary components as follows

$$x(t) = x_I(t) + jx_Q(t) \quad (3.23)$$

Comparing (3.22) and (3.23), the real and imaginary components of $x(t)$ can be written as below

$$\begin{aligned} x_I(t) &= z_I(t) \\ x_Q(t) &= g \cos(\phi) z_Q(t) - g \sin(\phi) z_I(t) \end{aligned} \quad (3.24)$$

and their frequency domain equivalents are as follows

$$\begin{aligned} X_I(f) &= Z_I(f) \\ X_Q(f) &= g \cos(\phi) Z_Q(f) - g \sin(\phi) Z_I(f) \end{aligned} \quad (3.25)$$

The final baseband signal after I and Q distortion filters is represented by $\tilde{z}(t)$ and is given as

$$\tilde{z}(t) = h_I(t) * x_I(t) + j h_Q(t) * x_Q(t) \quad (3.26)$$

The frequency domain representation of $\tilde{z}(t)$ is given as

$$\tilde{Z}(f) = X_I(f) H_I(f) + j X_Q(f) H_Q(f) \quad (3.27)$$

Substituting (3.25) in (3.27), $\tilde{Z}(f)$ can be written as

$$\begin{aligned} \tilde{Z}(f) &= Z_I(f) H_I(f) + j (g \cos(\phi) Z_Q(f) - g \sin(\phi) Z_I(f)) H_Q(f) \\ &= (H_I(f) - j g \sin(\phi) H_Q(f)) Z_I(f) + j (g \cos(\phi) H_Q(f)) Z_Q(f) \end{aligned} \quad (3.28)$$

Under FD IQI, the final baseband signal $\tilde{z}(t)$ can be written in terms of the original transmitted baseband signal $z(t)$ and its complex conjugate, or image, component $z^*(t)$ [23, 24] as follows,

$$\tilde{z}(t) = g_1(t) * z(t) + g_2(t) * z^*(t) \quad (3.29)$$

where $g_1(t)$ and $g_2(t)$ represent the impulse responses acting on $z(t)$ and $z^*(t)$ in the wideband frequency selective IQ imbalance model. By taking the FT of (3.29), $\tilde{Z}(f)$ is given as

$$\tilde{Z}(f) = G_1(f) Z(f) + G_2(f) Z^*(-f) \quad (3.30)$$

where $G_1(f)$ and $G_2(f)$ are the frequency responses acting on the signal and its complex conjugate image in the wideband FD IQI model (Fig. 3-8) . In general, the image at the mirror frequency is the effect of time domain complex conjugation.

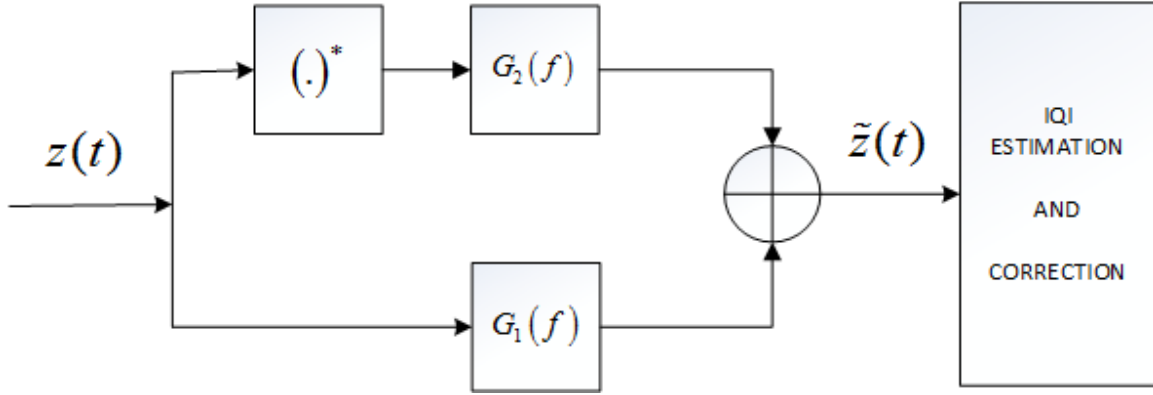


Figure 3-8. Simplified Frequency Dependent IQ Imbalance Model

Substituting $Z(f) = Z_I(f) + jZ_Q(f)$ in (3.30) ,

$$\tilde{Z}(f) = G_1(f)(Z_I(f) + jZ_Q(f)) + G_2(f)(Z_I^*(-f) - jZ_Q^*(-f)) \quad (3.31)$$

where $Z_I(f)$ and $Z_Q(f)$ are real signals, so using the property in (3.3), we get

$$\begin{aligned} Z_I(f) &= Z_I^*(-f) \\ Z_Q(f) &= Z_Q^*(-f) \end{aligned} \quad (3.32)$$

Substituting (3.32) in (3.31) yields

$$\tilde{Z}(f) = (G_1(f) + G_2(f))Z_I(f) + j(G_1(f) - G_2(f))Z_Q(f) \quad (3.33)$$

By comparing (3.33) and (3.28), we find

$$\begin{aligned}
G_1(f) + G_2(f) &= H_I(f) - jg \sin(\phi) H_Q(f) \\
G_1(f) - G_2(f) &= g \cos(\phi) H_Q(f)
\end{aligned} \tag{3.34}$$

Solving for $G_1(f)$ and $G_2(f)$, using $e^{j\phi} = \cos(\phi) + j \sin(\phi)$,

$$\begin{aligned}
G_1(f) &= [H_I(f) + H_Q(f) g e^{-j\phi}] / 2 \\
G_2(f) &= [H_I(f) - H_Q(f) g e^{j\phi}] / 2
\end{aligned} \tag{3.35}$$

The Image Rejection Ration (IRR) in case of FD IQI can then be written as follows:

$$\begin{aligned}
M(f) &= \frac{|G_1(f)|^2}{|G_2(f)|^2} \\
&= \frac{|H_I(f)|^2 + g^2 |H_Q(f)|^2 + g H_I(f) H_Q^*(f) e^{j\phi} + g H_I^*(f) H_Q(f) e^{-j\phi}}{|H_I(f)|^2 + g^2 |H_Q(f)|^2 - g H_I(f) H_Q^*(f) e^{-j\phi} - g H_I^*(f) H_Q(f) e^{j\phi}} \tag{3.36}
\end{aligned}$$

3.5 Image Rejection Ratio

The frequency dependent and frequency independent IQ Imbalances have a different kind of impact on the signal across the Nyquist range (Fig. 3-9) as analyzed in detail in the Sections 3.3 and 3.4. FI IQI has an Image Rejection Ration (IRR) that is constant over the entire Nyquist frequency range as shown in (3.19) whereas FD IQI has IIR that is frequency dependent and depends on the specific imbalances in the I and Q paths low-pass filters as given in (3.36).

As can be observed from Fig. 3-9, frequency dependent IQ Imbalance arising from minor differences in the frequency response of the filters in the I and Q paths has a detrimental effect; different components of the signal are distorted differently.

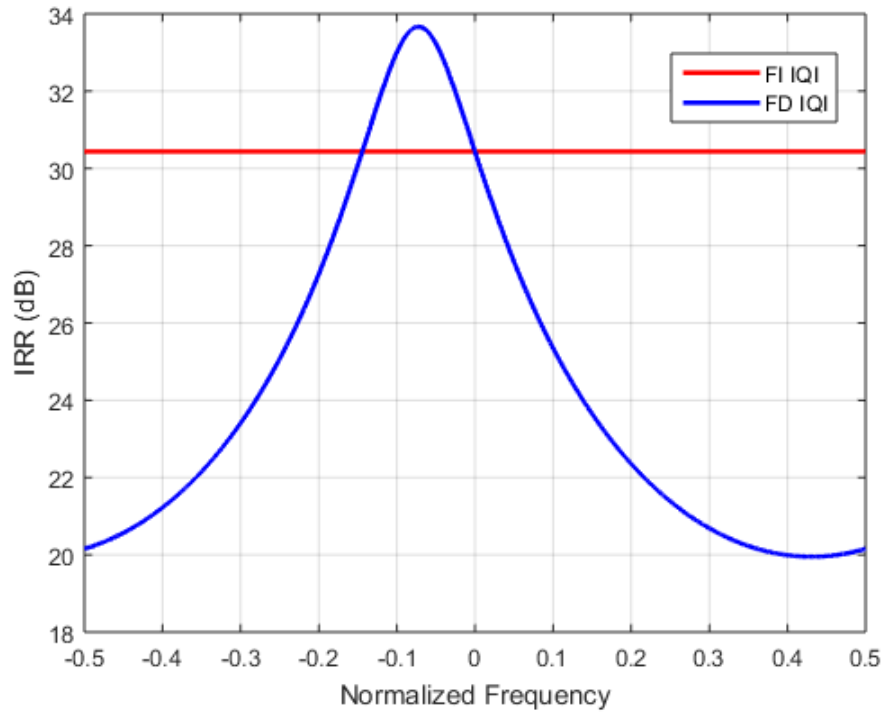


Figure 3-9. Image Rejection Ratio (Magnitude)

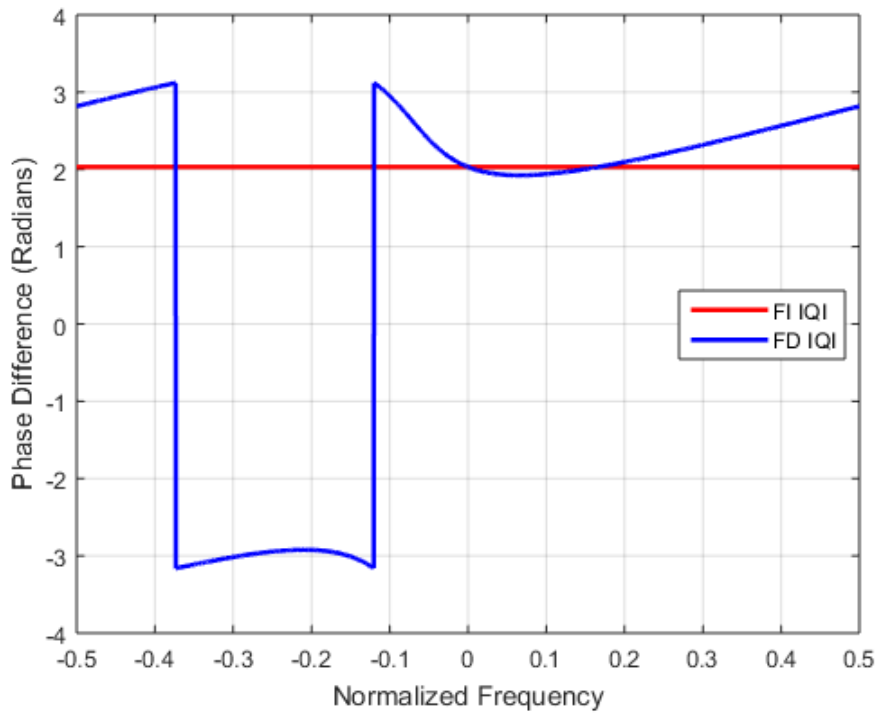


Figure 3-10. Image Rejection Ratio (Phase)

3.6 Multiple IF Signal Model

In practical systems, due to the shared use of the transmission medium, the received signal often consists of many signals in addition to the signal of interest. These signals originating from different physical sources have different power and occupy different parts of the frequency band. In this scenario, one of the challenges is to effectively decode the information from the desired signal in the presence of other signals.

As discussed in Sections 3.4 and 3.5, IQ Imbalance causes an image at the mirror frequency of the operating signal, so the signals at the mirror frequency of the desired signal will be affected. In case of a single channel at baseband, the image is directly formed on the signal itself, as it is its own mirror, whereas in the multiple channel scenario depicted in Fig. 3-11 channels at different IFs form images on the channels located at their mirror IFs. A higher signal strength at the mirror frequency of the desired signal can completely overpower/distort the signal of interest and therefore the impact of IQ Imbalance gets severe in the multiple IF scenario.

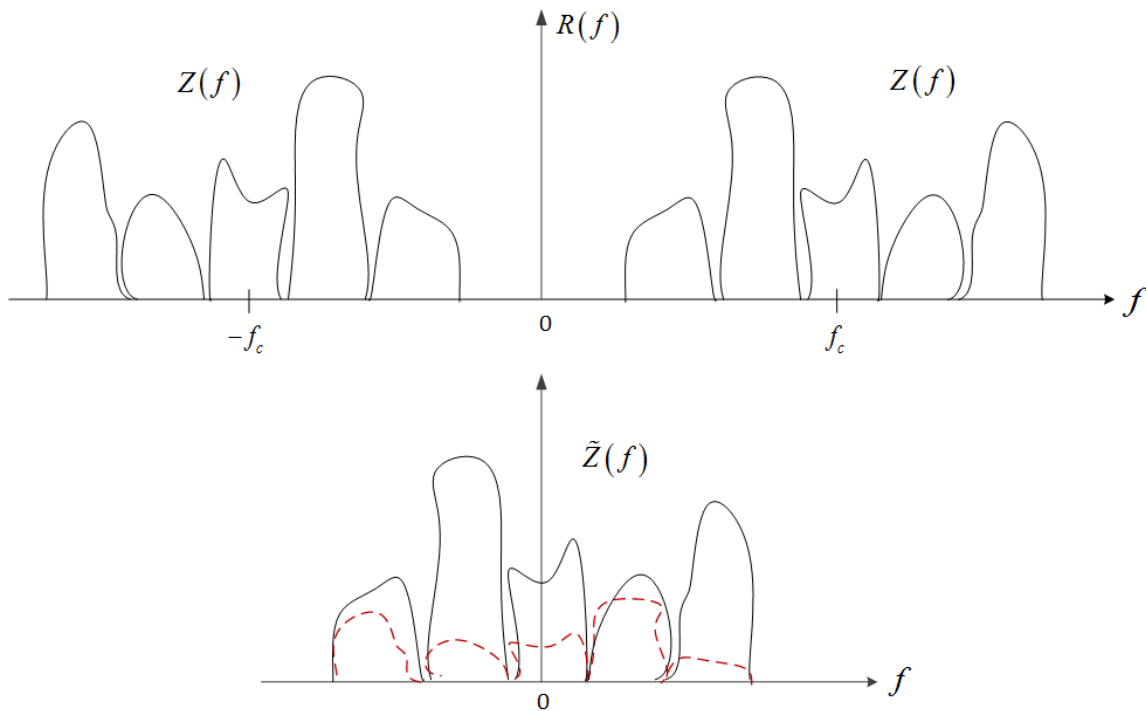


Figure 3-11. IQ Imbalance Effect on Multiple IF Signal

3.7 IQ Imbalance Effect on OFDM Signal

OFDM is a technique where information is transmitted on multiple carriers simultaneously with each of these carrier frequencies orthogonal to each other. This scenario is similar to the multiple IF described in Section 3.6 except that here all the carriers belong to one user. Considering just FD IQI and an ideal OFDM baseband signal $z(t)$, from (3.18), the imbalanced signal can be written in terms of OFDM carriers and their complex conjugate image components at the mirror carrier frequencies as,

$$\begin{aligned}\tilde{z}(t) &= k_1 z(t) + k_2 z^*(t) \\ &= k_1 \sum_{k=-\frac{N}{2}}^{\frac{N}{2}-1} s_k e^{j2\pi kn/N} + k_2 \sum_{k=-\frac{N}{2}}^{\frac{N}{2}-1} s_k^* e^{-j2\pi kn/N}\end{aligned}\quad (3.37)$$

where N is the total number of subcarriers within the OFDM symbol, s_k is the data symbol modulating the subcarrier k , k_1 and k_2 are the signal and image strengths as described in (3.16).

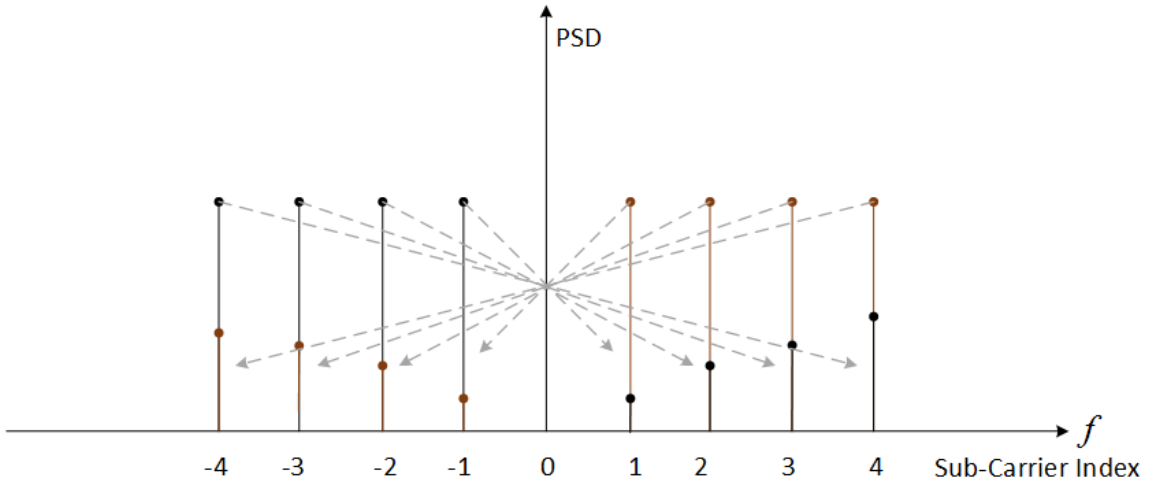


Figure 3-12. IQ Imbalance Effect on OFDM Signal

As depicted in Fig. 3-12, IQ Imbalance causes the subcarrier at index k to create an image on the subcarrier at $-k$; this effect resembles Inter Carrier Interference (ICI) as the subcarrier at k leaks into the subcarrier at $-k$ and vice-versa.

In summary, in this chapter the cause of IQI in the DDC receiver and the effects of frequency dependent and frequency independent IQ imbalances are explained in detail. In addition, the impact of IQI pertaining to multiple IF and OFDM scenarios is discussed. In the next chapter, a brief review of various IQI estimation and compensation techniques available in the literature is presented.

CHAPTER 4 IQ IMBALANCE ESTIMATION AND COMPENSATION TECHNIQUES

In Chapter 2 an overview is presented of the various RF impairments that might arise with a given kind of receiver architecture. Direct-Down Conversion systems are the focus of interest in this thesis, so that in Chapter 3 the IQ Imbalance problem specific to DDC receivers is analyzed in detail. This chapter starts with a description of possible scenarios causing IQ Imbalance from the point of view of system design and co-existence with other inherent RF impairments, after which different IQ Imbalance estimation and compensation techniques reported in the literature are covered.

4.1 Overview of Communication System Impairments

Irrespective of RF front-end architecture, wireless transceivers have inherent impairments such as Non-linear Amplification/Distortion, Carrier Frequency Offset (CFO), Phase-Noise and Sampling Frequency Offset (SFO) arising from different components (Table 4-1). In addition, DDC systems have IQ Imbalance and DC Offset problems. Consequently the co-existence effects of these impairments need to be considered when aiming to address the particular IQ imbalance.

Table 4-1. Various RF Components and their Impairments

Impairment Caused	RF Component (Major Source)
Non-Linear Amplification	Power Amplifier / LNA
Carrier Frequency Offset	Local Oscillator
Phase Noise	Local Oscillator
DC-Offset	Mixers, Local Oscillator
Sampling Frequency Offset (SFO)	ADC/DAC
IQ Imbalance	Mixers, Low-Pass Filters

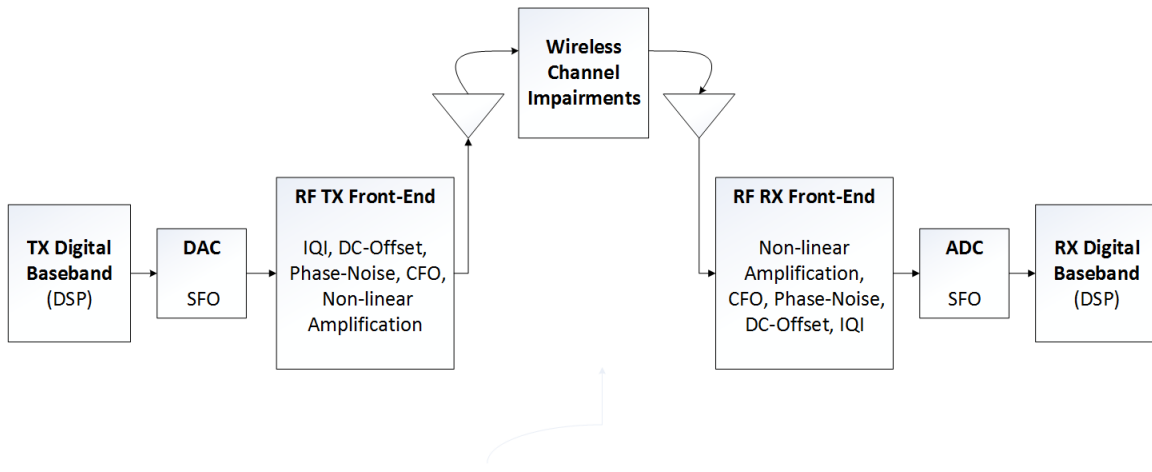


Figure 4-1. Wireless Communication Transmitter and Receiver Impairment Model

In addition to Transmitter and Receiver RF impairments, multi-path effects from the wireless channel also impact the signal (Figure 4-1). Therefore the design of the technique/algorithm for mitigating IQI depends upon the compensation model being used for the overall target system [25]. The following are the various models:

- IQI compensation only at the transmitter.
- IQI compensation only at the receiver that is inter-operable with other standard compliant transmitters.
- Joint TX and RX IQI compensation.
- IQI Compensation based on the type of transmission scheme: e.g. Single carrier systems or OFDM systems.
- IQI compensation in the presence of Frequency Offset, Phase-Noise, and DC-Offset.
- IQI compensation in the presence of a multi-path channel and/or multiple antennas.
- Any combination of the above scenarios.

Several digital estimation and compensation techniques have been proposed in the literature. Some of the most frequently used techniques in practical systems are described in detail in the following sections.

4.2 Digital Estimation and Compensation Using Test Tones

Estimation using test tones is the most frequently used method in industry. In this method locally generated test tones are passed through the system to estimate the effect of IQ imbalance. These test tones are chosen to be at a frequency close to the LO frequency and are injected just before the RF input of the mixer (right after the LNA). The output of the ADC forms the basis for characterization of the imbalance between I and Q branches. The differences between the received and known test signals are used to estimate the IQ imbalance parameters and are subsequently used for compensation [26, 27].

The advantages of using test tones are:

- Simple technique that is standard independent.
- Accurate and takes much less time for estimation compared to the other existing techniques.
- Frequency Dependent IQ imbalance can be estimated.

The disadvantages are:

- Offline, i.e. the transceiver cannot process actual data during the time of estimation.
- Needs to be estimated and calibrated for all the different ranges of operating frequencies and bandwidths.
- Risk of LO leakage due to test tone frequency.
- Additional hardware is required to generate the test tone and demands on spectral purity of the test tone further increase the overall cost of the transceiver.
- Cannot track time-varying IQ Imbalance.

4.3 Digital Estimation and Compensation Using Pilots

Instead of using test tones that are generated on the chip, this method uses known signals that are embedded in the transmitted signal. These known signals are referred to as pilots; their positions and corresponding symbols are predefined as part of the operating communication standard.

The coefficients of equalizer-type compensation structures are obtained based on the received signal at the pilot positions. This method can be used to compensate both FD and FI IQ Imbalances [28].

In standards like 802.11, LTE, pilot symbols are used for CFO, channel, and other estimations. So, the same pilots can be used for IQ imbalance estimation as well [29].

The advantages of using these existing pilot tones are:

- Online, i.e. no obstruction of the normal data processing of the transceiver as estimation happens simultaneously.
- Very fast and Frequency Dependent IQ imbalance can be estimated.

The disadvantages are:

- Complicated technique that depends on the placement of the pilot symbols being known.
- The estimation will be based on pilots that are already affected by the channel.
- Completely standard dependent.

4.4 Digital Estimation and Compensation Using Statistical Signal Properties

Estimation using Statistical Signal Properties is the preferred approach for a completely standard independent method. The system does not require pilots or test tones and relies instead on the properties of the received baseband signal. In the context of IQ Imbalance, second order properties such as circularity, or properness, are used for the estimation of compensation parameters [23]. IQ Imbalance estimation and compensation using statistical properties is used in actual GSM implementation by Elahi [30]. Most of the works reported in the literature used statistical methods to estimate frequency independent IQI, but Valkama applied a statistical method for estimation of frequency selective IQ imbalance as well [23, 24].

The advantages are:

- Online, i.e. the transceiver does not need to stop its normal data processing.
- Can be used for time-varying IQ imbalance estimation.
- Completely standard independent and works across all frequency ranges.
- Can also work on noise originating from the antenna and LNA even when there is no signal present.

The disadvantages are:

- Slow, it usually takes a longer time to come up with the compensation parameters compared to the methods discussed earlier.

4.5 Scenario of Interest

The problem statement for this thesis corresponds to the practical real time scenario in which signals with various carrier frequencies, bandwidths, and modulations – and aggregations of such signals – are received without prior information. The idea is to come up with an IQI correction or mitigation technique for such a scenario. In general, every transceiver corrects for its IQ imbalance, so a reasonable assumption of the signal being free from IQI in the transmitter end is made.

With the assumption that transmitter IQ imbalance is taken care of, the aim is to design a technique for a receiver that can track time-varying frequency selective IQ Imbalance without the need for test tone generators or pilot sequences. Furthermore this technique should work for wideband signals and any kind of modulation and/or multiplexing schemes.

IQ Imbalance distorts some of the second order statistical properties of complex base-band communication signals. So, the idea is to take advantage of the distortions introduced in the second order statistical properties and leverage the opportunity to design a scheme that would be independent of other RF impairments. Further details of this approach are discussed in the next chapter.

CHAPTER 5 BLIND-ADAPTIVE ESTIMATION AND COMPENSATION

Chapters 2, 3, and 4 gave the required background on the IQ imbalance impairment and defined the problem in detail. In this chapter, principles from the theory of random variables and adaptive signal processing are used to build a framework that can help in the estimation and compensation of IQ Imbalance [31]. A blind-adaptive technique is introduced and performance metrics used for analysis of IQI compensation are discussed.

5.1 Second Order Statistical Signal Properties

The signals and processes that are of interest to various aspects of communications system design are often random in nature rather than deterministic. Concepts from probability and stochastic processes help in understanding random signals and to build models for them. In general, mean and second order statistics are frequently used to comment on the behavior of random signals. The mean of a complex valued random signal $x(t) = x_I(t) + jx_Q(t)$ is defined as

$$\mu_x(t) \triangleq E[x(t)] = E[x_I(t)] + jE[x_Q(t)] \quad (5.1)$$

The cross-correlation function of two complex valued random signals $x(t) = x_I(t) + jx_Q(t)$ and $y(t) = y_I(t) + jy_Q(t)$ is defined as

$$\gamma_{xy}(t, \tau) \triangleq E[x(t)y^*(t+\tau)] \quad (5.2)$$

their complementary cross-correlation function is defined by

$$c_{xy}(t, \tau) \triangleq E[x(t)y(t+\tau)] \quad (5.3)$$

where t is the continuous time variable and τ is the time shift introduced. For a complete description of joint second order stationarity of the two signals, both of these moments are needed.

Using the definitions of cross-correlation and complementary cross-correlation in (5.2) and (5.3), the autocorrelation (ACF) and complementary autocorrelation (CACF) of signal $x(t)$ can be defined as

$$\gamma_x(t, \tau) \triangleq \text{E}[x(t)x^*(t + \tau)] \quad (5.4)$$

$$c_x(t, \tau) \triangleq \text{E}[x(t)x(t + \tau)] \quad (5.5)$$

The complementary autocorrelation can be viewed as the cross-correlation of $x(t)$ and its complex-conjugate $x^*(t)$ as shown below,

$$\begin{aligned} c_x(t, \tau) &\triangleq \text{E}[x(t)(x^*(t + \tau))^*] \\ &= \text{E}[x(t)x(t + \tau)] \end{aligned} \quad (5.6)$$

5.2 Stationarity of Signals

Stationarity is a quality of a signal of which (some of the) statistical properties do not change with time. Stationarity is a typical assumption made in the literature to make the analysis more tractable. Furthermore, a signal is considered wide-sense stationary (WSS) if its mean and ACF are independent of time t [32], and second-order stationary (SOS) if, in addition, its CACF is independent of t .

Under wide-sense stationarity, the ACF will only be a function of the time difference τ , as it is independent of time t , and can be formally redefined as

$$\gamma_x(\tau) \triangleq \text{E}[x(t)x^*(t + \tau)] \quad (5.7)$$

In addition to stationarity, the concept of ergodicity is of major importance while building practical estimators for random signals. Ergodicity means that the time-average moments of a random process are equal to the corresponding ensemble averages [33]. This property of ergodicity helps in using the samples collected in time to calculate mean and second order statistics of random variables and processes. Further detailed discussion on ergodicity is beyond the scope of this thesis but ergodicity along with WSS and zero-mean are assumed for all the signals from this point on throughout the course of this thesis.

5.2 Circularity and Properness

A complex random signal $x(t)$ is said to be **circular** if $x(t)$ and $e^{j\alpha}x(t)$ have the same probability distribution function for any $\alpha \in [0, 2\pi)$. This strict form of circularity is rather difficult to measure in practice and a weaker form of circularity, called N^{th} order circularity, is defined as $x(t)$ and $e^{j\alpha}x(t)$ having equal moments up to order N for any $\alpha \in [0, 2\pi)$. Strict circularity implies moment circularity but not vice-versa. The Gaussian distribution is a special case for which second-order circularity implies strict circularity [34].

Assuming $x(t)$ to be a zero-mean signal, the conditions for second-order circularity (i.e. moments till order two are equal) are as follows

$$\begin{aligned} E[x(t)] &= 0 \\ E[x^2(t)] &= 0 \end{aligned} \tag{5.8}$$

As defined earlier if a signal is WSS and if its CACF depends only on τ , it is said to be second-order stationary (SOS) and CACF in this case can be written as

$$c_x(\tau) \triangleq E[x(t)x(t+\tau)] \tag{5.9}$$

At $\tau = 0$,

$$c_x(0) \triangleq \mathbb{E}[x^2(t)] = \mathbb{E}[x(t)(x^*(t))^*] = 0 \quad (5.10)$$

Therefore from (5.8) and (5.10) it can be concluded that second-order circularity of a zero-mean complex random variable is equivalent to its CACF being zero at $\tau = 0$.

By expanding $x(t)$ in (5.10) and taking the expectation,

$$\begin{aligned} c_x(0) &\triangleq \mathbb{E}\left[(x_I(t) + jx_Q(t))^2\right] = 0 \\ &\Rightarrow \mathbb{E}\left[x_I^2(t) - x_Q^2(t) + 2jx_I(t)x_Q(t)\right] = 0 \end{aligned} \quad (5.11)$$

Equation (5.11) implies that

$$\begin{cases} \mathbb{E}[x_I^2(t)] = \mathbb{E}[x_Q^2(t)] \\ \mathbb{E}[x_I(t)x_Q(t)] = 0 \end{cases} \quad (5.12)$$

From (5.12), second-order circularity can be interpreted as the real and imaginary parts of the signal being equally powerful and mutually uncorrelated, and that this property of circularity cannot be established for real-valued signals, unless $x(t) \equiv 0$.

In the spectral domain, circularity can be interpreted as $x(t)$ and $x^*(t)$ occupying non-overlapping frequency bands which implies that $x(t)$ and its complex-conjugate $x^*(t)$ are mutually uncorrelated as described in (5.10).

A signal $x(t)$ is said to be **proper** when the CACF in (5.9) becomes zero for all τ , so that properness is a more general and stricter form of second-order circularity.

$$c_x(\tau) \triangleq \mathbb{E}[x(t)x(t+\tau)] = 0, \forall \tau \quad (5.13)$$

Properness implies that $x(t)$ and $x^*(t)$ are mutually uncorrelated for all possible time shifts τ . So, properness implies circularity but not vice-versa. In general, most of the commonly used communication signals (QAM, PSK (M>2)) are proved to be proper and therefore circular [35]. As BPSK falls under the category of real signals it cannot be proper or circular.

The concepts of second-order statistics and properness can be extended to vector-valued complex random signals such as $\mathbf{x}(t) = [x_1(t), x_2(t), \dots, x_n(t)]^T$. The $N \times N$ matrix-valued ACF of $\mathbf{x}(t)$ is defined as

$$\mathbf{\Gamma}_x(\tau) \triangleq \mathbb{E}[\mathbf{x}(t)\mathbf{x}^H(t+\tau)] \quad (5.14)$$

Similarly, the $N \times N$ matrix-valued CACF is defined as

$$\mathbf{C}_x(\tau) \triangleq \mathbb{E}[\mathbf{x}(t)\mathbf{x}^T(t+\tau)] \quad (5.15)$$

For this signal to be proper,

$$\mathbf{C}_x(\tau) = \mathbf{0}, \forall \tau \quad (5.16)$$

This means that all the individual signal elements are proper, i.e. $c_{x_i}(\tau) = \mathbb{E}[x_i(t)x_i(t+\tau)] = 0, \forall i$, as well as being jointly proper, i.e. $\mathbb{E}[x_i(t)x_j(t+\tau)] = 0, \forall i, j \neq i$.

5.3 Properness in the Context of Multicarrier IF Signals

The scenario of interest in this thesis is the reception of multiple RF channels, each appearing at their individual IFs after I/Q down-conversion. The aim is to validate the properness of the signal modulated onto an IF carrier and then to extend that to a multicarrier IF signal.

Let $z(t)$ be a complex-valued baseband signal which is proper, i.e. $c_z(\tau) = 0, \forall \tau$. The complex IF signal $s(t)$ can be denoted as follows

$$s(t) = z(t)e^{j2\pi f_{IF}t} \quad (5.17)$$

$$\begin{aligned} c_s(\tau) &= E[s(t+\tau)s(t)] \\ &= E[e^{j2\pi f_{IF}(2t+\tau)}z(t+\tau)z(t)] \\ &= E[e^{j2\pi f_{IF}(2t+\tau)}]c_z(\tau) \\ &= 0 \quad \forall \tau \end{aligned} \quad (5.18)$$

This shows that an IF signal is proper if the corresponding baseband signal is proper. Now, considering the sum of multiple synchronized IF signals.

$$\begin{aligned} s(t) &= \sum_{i=1}^N z_i(t)e^{j2\pi f_i t} \\ &= \mathbf{f}^T(t)\mathbf{z}(t) \end{aligned} \quad (5.19)$$

where $\mathbf{f}(t) = [e^{j2\pi f_1 t}, e^{j2\pi f_2 t}, \dots, e^{j2\pi f_N t}]^T$ and $\mathbf{z}(t) = [z_1(t), z_2(t), \dots, z_n(t)]^T$.

Assuming that all individual IF signals are proper as well as jointly proper, one can write that $\mathbf{C}_z(\tau) \triangleq E[\mathbf{z}(t)\mathbf{z}^T(t+\tau)] = 0, \forall \tau$ (using the concept explained below (5.16)).

From (5.15), the CACF (properness measure) of $s(t)$ is given as follows

$$\mathbf{C}_s(\tau) \triangleq E[\mathbf{s}(t)\mathbf{s}^T(t+\tau)] \quad (5.20)$$

Substituting (5.19) into (5.20) then yields

$$\begin{aligned} \mathbf{C}_s(\tau) &\triangleq \mathbf{f}^T(t)E[\mathbf{z}(t)\mathbf{z}^T(t+\tau)]\mathbf{f}(t+\tau) \\ &= \mathbf{f}^T(t)\mathbf{C}_z(\tau)\mathbf{f}(t+\tau) \\ &= 0 \quad \forall \tau \end{aligned} \quad (5.21)$$

which shows that properness remains intact in the composite IF signal.

5.4 Effects of Non-idealities on Properness

The earlier Section 5.3 showed that modulating the baseband signal with an IF carrier frequency does not affect properness, and that same concept can be logically extended to RF up-conversion as well. In this section, the effects of various RF and channel non-idealities on the properness of the baseband signal are explored [24, 31, 36, 37]. The effects are studied in their order of occurrence in the transmitter-receiver chain.

Power Amplifier Nonlinearity:

While operating in the non-linear region, a Power Amplifier (PA) distorts the signal of interest by creating signal components of higher orders. The results in [38] prove that a third-order non-linearity which has the most dominant impact in realistic operating scenarios, does not distort the properness of the signal. Similar analysis can be extended to higher order non-linearities and memory effects of a PA and one can conclude that a PA in general preserves the properness or non-properness of its input signal.

Linear Filtering and Radio Channel:

A linear time-invariant filtering operation occurs at multiple instances in the transmitter-receiver chain. The effect of time-invariant filtering is analyzed and then the impact of a more complicated time-varying radio channel is understood.

Considering a proper baseband signal $z(t) = z_I(t) + jz_Q(t)$ and filter impulse response $h(t) = h_I(t) + jh_Q(t)$, the output signal is given as follows,

$$s(t) = z(t) * h(t) \tag{5.22}$$

The CACF of $s(t)$ is given by

$$\begin{aligned}
c_s(\tau) &\triangleq \mathbb{E}[s(t)s(t+\tau)] \\
&= \mathbb{E}\left[(z(t)*h(t))(z(t+\tau)*h(t+\tau))\right] \\
&= \mathbb{E}\left[\left(\int_{-\infty}^{\infty} h(\tau_1)z(t-\tau_1)d\tau_1\right)\left(\int_{-\infty}^{\infty} h(\tau_2)z(t+\tau-\tau_2)d\tau_2\right)\right] \quad (5.23) \\
&= \int_{-\infty}^{\infty} \int_{-\infty}^{\infty} h(\tau_1)h(\tau_2)\mathbb{E}[z(t-\tau_1)z(t+\tau-\tau_2)]d\tau_1d\tau_2 \\
&= \int_{-\infty}^{\infty} \int_{-\infty}^{\infty} h(\tau_1)h(\tau_2)c_z(\tau-\tau_2+\tau_1)d\tau_1d\tau_2
\end{aligned}$$

In the above equation, when $c_z(\tau)=0, \forall \tau$, then also $c_s(\tau)=0, \forall \tau$; therefore linear time-invariant channel distortions preserve the properness of the baseband signal.

Considering a time-varying radio channel with N taps, the output signal can be represented as

$$s(t) = \sum_{k=1}^N h_k z(t - \delta_k) \quad (5.24)$$

where h_k and δ_k represent the random complex gain and fixed delay of the k^{th} multipath component [24]. Using a similar development as shown in (5.23) and assuming statistical independence of signal and channel, the CACF of output signal $s(t)$ is given as

$$\begin{aligned}
c_s(\tau) &\triangleq \mathbb{E}[s(t)s(t+\tau)] \\
&= \sum_{k_1=1}^N \sum_{k_2=1}^N \mathbb{E}\left[h_{k_1}h_{k_2}z(t-\delta_{k_1})z(t+\tau-\delta_{k_2})\right] \quad (5.25) \\
&= \sum_{k_1=1}^N \sum_{k_2=1}^N \mathbb{E}\left[h_{k_1}h_{k_2}\right]c_z(\tau-\delta_{k_2}+\delta_{k_1})
\end{aligned}$$

Thus $c_s(\tau)$ will equal zero for all τ as $z(t)$ is proper and therefore $c_z(\tau) = 0, \forall \tau$. This leads to the conclusion that the channel does not affect the properness of the signal.

By assuming independent fading paths, $E[h_{k_1} h_{k_2}] = 0, \forall k_1 \neq k_2$. Furthermore, in the case of Rayleigh fading where complex path gains are Gaussian, which means they are circular [34], i.e. $E[h_k^2] = 0, \forall k$. Combining the two assumptions implies that

$$E[h_{k_1} h_{k_2}] = 0, \forall k_1 = k_2 \quad (5.26)$$

By substituting the condition in (5.26) into (5.25), it can be concluded that with independent fading paths and circular path gains, the time-varying channel makes the signal $s(t)$ proper irrespective of the properness of $z(t)$.

Additive White Gaussian Noise:

Additive Noise is that generated by various RF devices on the circuit which can be visualized as another real valued band-pass signal. The complex envelope of this stationary real valued signal at baseband is proper [32]. As stated in Section 5.2, the addition of two proper signals results in a proper signal, so that we can conclude that AWGN does not distort the properness of the complex baseband version of an RF signal. However this is under the assumption that the major sources of this noise are the LNA and antenna and the non-proper noise that might result from mixers and ADCs due to imbalances in the I/Q paths are negligible. This assumption is often made in the literature because these I/Q components contribute very little to the overall noise figure of the device [2].

Carrier Frequency Offset:

Differences between the carrier frequencies at the transmitter and receiver ends, affect the baseband signal by rotating the constellation with time t . The baseband signal $z(t)$ with

carrier frequency offset (CFO) can be represented as $s(t) = z(t)e^{j2\pi\Delta f t}$, and its CACF can be calculated as follows

$$\begin{aligned}
c_s(\tau) &\triangleq \mathbb{E}[s(t+\tau)s(t)] \\
&= \mathbb{E}\left[e^{j2\pi\Delta f(2t+\tau)}z(t+\tau)z(t)\right] \\
&= \mathbb{E}\left[e^{j2\pi\Delta f(2t+\tau)}\right]c_z(\tau) \\
&= 0 \quad \forall \tau
\end{aligned} \tag{5.27}$$

The result in (5.27) implies that CFO does not affect properness.

Phase Offset:

Phase offset of the signal which affects perfect timing synchronization can be represented as $s(t) = e^{j\theta}z(t)$, and its CACF can be evaluated as follows

$$\begin{aligned}
c_s(\tau) &\triangleq \mathbb{E}[s(t+\tau)s(t)] \\
&= \mathbb{E}\left[e^{j2\pi\Delta f(2t+\tau)}e^{j2\theta}z(t+\tau)z(t)\right] \\
&= \mathbb{E}\left[e^{j2\pi\Delta f(2t+\tau)}\right]c_z(\tau)\mathbb{E}\left[e^{j2\theta}\right] \\
&= 0 \quad \forall \tau
\end{aligned} \tag{5.28}$$

The same analysis can be extended to understand the impact of phase noise on properness. In addition, under Wiener phase noise [38], $\mathbb{E}[e^{j2\theta}] = 0$ which implies that now there are two components in (5.28) that will be pulling $c_s(\tau)$ towards zero which is claimed to be a stronger form of properness.

DC Offset:

Effects like LO Leakage and Self-Mixing create a DC offset which clearly makes the signal non-zero mean and thereby non-proper. In addition, even-order non-linearities that create a DC component can also make the signal non-proper [13].

In general, DC offset is compensated in the analog domain using a notch filter and the residual DC is further compensated in the digital domain by subtracting the mean of the signal from the signal itself. This way, the problem of DC offset is taken care of so that it does not affect the further processing of the signal.

IQ Imbalance:

The effects of IQ imbalance on a baseband signal are discussed in detail in Chapter 3 and, from (3.29), the baseband signal resulting from the impact of generic FD IQI can be written as

$$s(t) = g_1(t) * z(t) + g_2(t) * z^*(t) \quad (5.29)$$

The property in the above equation which involves filtering operations on both the signal and its complex conjugate is termed **widely linear filtering** [37, 39, 40]. This concept of widely linear filtering is elaborated further in the next section.

The CACF of $s(t)$ is given by

$$\begin{aligned} c_s(\tau) &\triangleq E[s(t)s(t+\tau)] \\ &= E\left[\left(g_1(t) * z(t) + g_2(t) * z^*(t)\right)\left(g_1(t+\tau) * z(t+\tau) + g_2(t+\tau) * z^*(t+\tau)\right)\right] \\ &= E\left[\left(g_1(t) * z(t)\right)\left(g_1(t+\tau) * z(t+\tau) + g_2(t+\tau) * z^*(t+\tau)\right)\right] \\ &\quad + E\left[\left(g_2(t) * z^*(t)\right)\left(g_1(t+\tau) * z(t+\tau) + g_2(t+\tau) * z^*(t+\tau)\right)\right] \\ &= E\left[\left(g_1(t) * z(t)\right)\left(g_1(t+\tau) * z(t+\tau)\right)\right] \\ &\quad + E\left[\left(g_1(t) * z(t)\right)\left(g_2(t+\tau) * z^*(t+\tau)\right)\right] \\ &\quad + E\left[\left(g_2(t) * z^*(t)\right)\left(g_1(t+\tau) * z(t+\tau)\right)\right] \\ &\quad + E\left[\left(g_2(t) * z^*(t)\right)\left(g_2(t+\tau) * z^*(t+\tau)\right)\right] \end{aligned} \quad (5.30)$$

By substituting the definition of convolution, $x(t) * y(t) = \int_{-\infty}^{\infty} x(\tau)y(t-\tau)d\tau$, the expression can be written as

$$\begin{aligned}
c_s(\tau) &= \mathbb{E} \left[\left(\int_{-\infty}^{\infty} g_1(\tau_1) z(t-\tau_1) d\tau_1 \right) \left(\int_{-\infty}^{\infty} g_1(\tau_2) z(t+\tau-\tau_2) d\tau_2 \right) \right] \\
&+ \mathbb{E} \left[\left(\int_{-\infty}^{\infty} g_1(\tau_1) z(t-\tau_1) d\tau_1 \right) \left(\int_{-\infty}^{\infty} g_2(\tau_2) z^*(t+\tau-\tau_2) d\tau_2 \right) \right] \\
&+ \mathbb{E} \left[\left(\int_{-\infty}^{\infty} g_2(\tau_1) z^*(t-\tau_1) d\tau_1 \right) \left(\int_{-\infty}^{\infty} g_1(\tau_2) z(t+\tau-\tau_2) d\tau_2 \right) \right] \\
&+ \mathbb{E} \left[\left(\int_{-\infty}^{\infty} g_2(\tau_1) z^*(t-\tau_1) d\tau_1 \right) \left(\int_{-\infty}^{\infty} g_2(\tau_2) z^*(t+\tau-\tau_2) d\tau_2 \right) \right] \\
&= \int_{-\infty}^{\infty} \int_{-\infty}^{\infty} g_1(\tau_1) g_1(\tau_2) \mathbb{E} [z(t-\tau_1) z(t+\tau-\tau_2)] d\tau_1 d\tau_2 \\
&+ \int_{-\infty}^{\infty} \int_{-\infty}^{\infty} g_1(\tau_1) g_2(\tau_2) \mathbb{E} [z(t-\tau_1) z^*(t+\tau-\tau_2)] d\tau_1 d\tau_2 \\
&+ \int_{-\infty}^{\infty} \int_{-\infty}^{\infty} g_2(\tau_1) g_1(\tau_2) \mathbb{E} [z^*(t-\tau_1) z(t+\tau-\tau_2)] d\tau_1 d\tau_2 \\
&+ \int_{-\infty}^{\infty} \int_{-\infty}^{\infty} g_2(\tau_1) g_2(\tau_2) \mathbb{E} [z^*(t-\tau_1) z^*(t+\tau-\tau_2)] d\tau_1 d\tau_2
\end{aligned} \tag{5.31}$$

The first and the fourth terms are zeros as $c_z(\tau) = 0, \forall \tau$, so the expression simplifies to

$$\begin{aligned}
c_s(\tau) &= \int_{-\infty}^{\infty} \int_{-\infty}^{\infty} g_1(\tau_1) g_2(\tau_2) \mathbb{E} [z(t-\tau_1) z^*(t+\tau-\tau_2)] d\tau_1 d\tau_2 \\
&+ \int_{-\infty}^{\infty} \int_{-\infty}^{\infty} g_2(\tau_1) g_1(\tau_2) \mathbb{E} [z^*(t-\tau_1) z(t+\tau-\tau_2)] d\tau_1 d\tau_2
\end{aligned} \tag{5.32}$$

Using the definition of the ACF, $\gamma_x(t, \tau) \triangleq \mathbb{E} [x(t) x^*(t+\tau)]$,

$$\begin{aligned}
c_s(\tau) &= \int_{-\infty}^{\infty} \int_{-\infty}^{\infty} g_1(\tau_1) g_2(\tau_2) \gamma_z(\tau-\tau_2+\tau_1) d\tau_1 d\tau_2 \\
&+ \int_{-\infty}^{\infty} \int_{-\infty}^{\infty} g_2(\tau_1) g_1(\tau_2) \gamma_z(-\tau+\tau_2-\tau_1) d\tau_1 d\tau_2
\end{aligned} \tag{5.33}$$

$$\begin{aligned}
c_s(\tau) = & \int_{-\infty}^{\infty} g_2(\tau_2) d\tau_2 \int_{-\infty}^{\infty} g_1(\tau_1) \gamma_z(\tau - \tau_2 + \tau_1) d\tau_1 \\
& + \int_{-\infty}^{\infty} g_1(\tau_2) d\tau_2 \int_{-\infty}^{\infty} g_2(\tau_1) \gamma_z(-\tau + \tau_2 - \tau_1) d\tau_1
\end{aligned} \tag{5.34}$$

using $\int_{-\infty}^{\infty} x(\tau) y(t - \tau) d\tau = x(t) * y(t)$, a further simplification is obtained.

$$c_s(\tau) = g_1(\tau) * g_2(-\tau) * \gamma_z(\tau) + g_1(-\tau) * g_2(\tau) * \gamma_z(-\tau) \tag{5.35}$$

The CACF $c_s(\tau)$ in (5.35) is clearly not zero for all values of τ since it is a function of $g_1(t)$, $g_2(t)$ and $\gamma_z(t)$; consequently, generally the IQI impaired signal will thus be non-proper.

After exploring the effects of various RF and channel impairments on the properness of a signal, the conclusion is that the non-idealities acting on the signal between carrier up-conversion and down-conversion – such as non-linear amplification, wireless channel, CFO, phase offset, AWGN – do not affect the properness of the signal. Whereas non-idealities acting on the signal in the analog domain before up-conversion and after down-conversion – such as DC offset, IQ imbalance (due to mixers, low-pass filters and ADCs) – do distort the properness of the signal. Assuming DC offset is corrected, the properness measure of a signal can be used to estimate the compensation parameters for IQI, which constitutes the core idea of the thesis and is explored in further detail in the subsequent sections.

5.5 Theoretical Optimal Solution

IQ imbalance leads to a complex-conjugate image in the band of interest due to a signal in the mirror frequency band. This crosstalk between $Z(f)$ and $Z^*(-f)$ is termed

mirror frequency interference and is explained by the widely linear (linear-conjugate-linear) model [41] of IQ imbalance, given in (5.29) as $s(t) = g_1(t) * z(t) + g_2(t) * z^*(t)$.

The structure for the IQ Imbalance Compensator (IQIC) also naturally needs to be of the widely linear form [23, 24, 28, 42] and is generally referred as widely linear filtering and can be considered as follows.

$$y(t) = w_1(t) * s(t) + w_2(t) * s^*(t) \quad (5.36)$$

The motivation behind this widely linear filtering is to annihilate the complex-conjugate component present in its input signal and thereby making the widely linear filter output signal free of IQ imbalance.

Substituting the expression for $s(t)$ in (5.36), yields

$$\begin{aligned} y(t) = & w_1(t) * (g_1(t) * z(t) + g_2(t) * z^*(t)) \\ & + w_2(t) * (g_1^*(t) * z^*(t) + g_2^*(t) * z(t)) \end{aligned} \quad (5.37)$$

Writing (5.37) in terms of the actual baseband signal of interest $z(t)$ and its complex-conjugate $z^*(t)$ produces:

$$\begin{aligned} y(t) = & (g_1(t) * w_1(t) + g_2^*(t) * w_2(t)) * z(t) \\ & + (g_1^*(t) * w_2(t) + g_2(t) * w_1(t)) * z^*(t) \end{aligned} \quad (5.38)$$

The IQIC structure in (5.36) can be simplified by assuming $w_1(t) = \delta(t)$ and $w_2(t) = w(t)$ which leads to the IQIC structure described below and shown in Fig. 5-1.

$$y(t) = s(t) + w(t) * s^*(t) \quad (5.39)$$

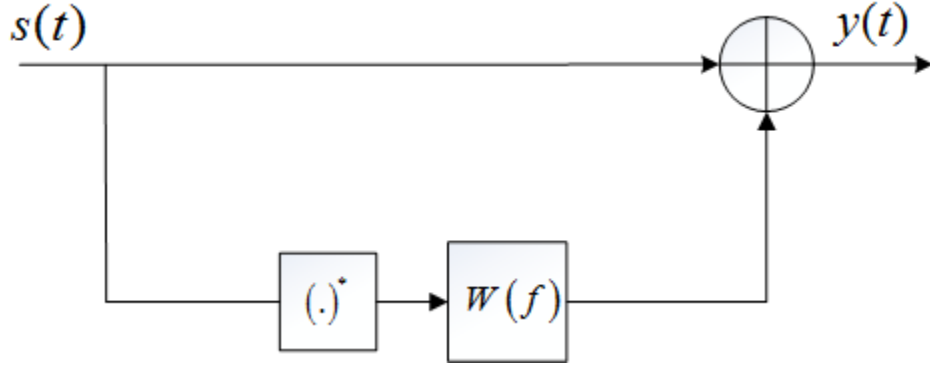


Figure 5-1. Widely Linear IQI Compensator

Using the same choices for $w_1(t)$ and $w_2(t)$, the output of the IQIC given in (5.38) can now be written as

$$y(t) = (g_1(t) + g_2^*(t) * w(t)) * z(t) + (g_1^*(t) * w(t) + g_2(t)) * z^*(t) \quad (5.40)$$

The frequency domain representation of the IQIC output $y(t)$ is as follows

$$Y(f) = (G_1(f) + G_2^*(-f)W(f))Z(f) + (G_1^*(-f)W(f) + G_2(f))Z^*(-f) \quad (5.41)$$

In order to make the signal free of $Z^*(-f)$, the kernel in the above expression that operates on it should go to zero, which gives the optimal IQI compensation filter frequency response as below

$$W(f) = W_{OPT}(f) = \frac{-G_2(f)}{G_1^*(-f)} \quad (5.42)$$

where $G_1(f) = [H_I(f) + H_Q(f)ge^{-j\phi}]/2$ and $G_2(f) = [H_I(f) - H_Q(f)ge^{j\phi}]/2$ from (3.35).

The output of the IQIC is obtained by substituting (5.42) in (5.41) and is given by

$$Y(f) = \left(G_1(f) - G_2^*(-f) \left(\frac{G_2(f)}{G_1^*(-f)} \right) \right) Z(f) \quad (5.43)$$

Therefore the output of the optimal IQIC, as expected, is free of mirror frequency interference, but with some amplitude and phase distortions. This effect is similar to that of a wireless channel and can be mitigated along with channel equalization, which is done later in the receiver chain. $G_1(f)$ and $G_2(f)$, as shown in (3.35), are functions of gain, phase, and I/Q filter imbalances. The impact of the distortions, considering realistic values of these imbalance parameters, is analyzed in Section 6.5.

The optimal solution is derived by nullifying the kernel of the mirror frequency interference term; however, this is tough to realize in practical systems as $G_1(f)$ and $G_2(f)$, are not constant and not known in advance, so the associated statistical property, i.e. the CACF of the output signal, is forced to zero so that the signal and mirror interference component become uncorrelated.

The output of the IQIC as given by (5.40) is

$$y(t) = (g_1(t) + g_2^*(t) * w(t)) * z(t) + (g_1^*(t) * w(t) + g_2(t)) * z^*(t).$$

Now calculating the CACF for $y(t)$ as described in (5.35), the CACF at the output of the IQIC is given by

$$c_y(\tau) = \hat{g}_1(\tau) * \hat{g}_2(-\tau) * \gamma_z(\tau) + \hat{g}_1(-\tau) * \hat{g}_2(\tau) * \gamma_z(-\tau) \quad (5.44)$$

where $\hat{g}_1(t) = g_1(t) + g_2^*(t) * w(t)$ and $\hat{g}_2(t) = g_1^*(t) * w(t) + g_2(t)$.

So, the CACF will go to zero if either of $\hat{g}_1(t)$ or $\hat{g}_2(t)$ is zero; setting $\hat{g}_2(t) = 0$ yields

$$W(f) = \frac{-G_2(f)}{G_1^*(-f)} \quad (5.45)$$

which is again the optimal solution derived in (5.42).

By setting $\hat{g}_1(t) = 0$,

$$W(f) = \frac{-G_1(f)}{G_2^*(-f)} \quad (5.46)$$

This is the (inverse) conjugate solution $W(f) = 1/W_{OPT}^*(f)$, that nullifies $z(t)$ and recovers $z^*(t)$. So practical systems built based on the properness of the signal should estimate the $W_{OPT}(f)$ rather than its conjugate solution in order to extract the signal of interest.

5.6 Adaptive Filter Model

The focus of this section is to come up with practically implementable methods to realize the optimal compensation filter in the digital domain that mitigates IQ imbalance by nullifying the mirror interference component that is present together with the baseband signal of interest.

As the compensation is done after analog to digital conversion, the first step is to formulate the optimal solution that can be achieved in the discrete domain and this can be written from the result in (5.42) as

$$W_{OPT}(z) = \frac{-G_2(z)}{G_1^*(z^*)} \quad (5.47)$$

This ideal optimal discrete solution can be visualized as the central copy of the continuous time domain optimal filter created at baseband after sampling and assumed to be acceptably free of aliasing, i.e. the signal was sufficiently filtered and sampled at a sufficiently high rate.

For the case of frequency independent IQ imbalance, the optimal solution can be written as

$$W_{OPT} = \frac{-K_2}{K_1^*} \quad (5.48)$$

Therefore in the simplified case of FI IQI, a single-tap compensator would be sufficient, whereas the optimal solution for the generic FD IQI case has both poles and zeros (it is an IIR filter) and would thus ideally require an infinite number of FIR taps for the ideal compensator.

For simpler analysis, by modeling the analog I/Q imbalance filters as short length FIR filters, $G_1(z)$ and $G_2(z)$ will also be short length FIR filters. $W_{OPT}(z)$ will be an IIR filter and can be approximated as an FIR filter $W(z)$ of some length N . The detailed analysis regarding the optimal choice for N is presented in Section 6.4.

The output of the IQIC in the discrete domain from the result in (5.39) can now be written as

$$y(n) = s(n) + \mathbf{w}^T(n) \mathbf{s}^*(n) \quad (5.49)$$

where $\mathbf{w}(n) = [w(0), w(1), \dots, w(N-1)]^T$, $\mathbf{s}(n) = [s(n), s(n-1), \dots, s(n-N+1)]^T$, and N is the number of FIR filter taps.

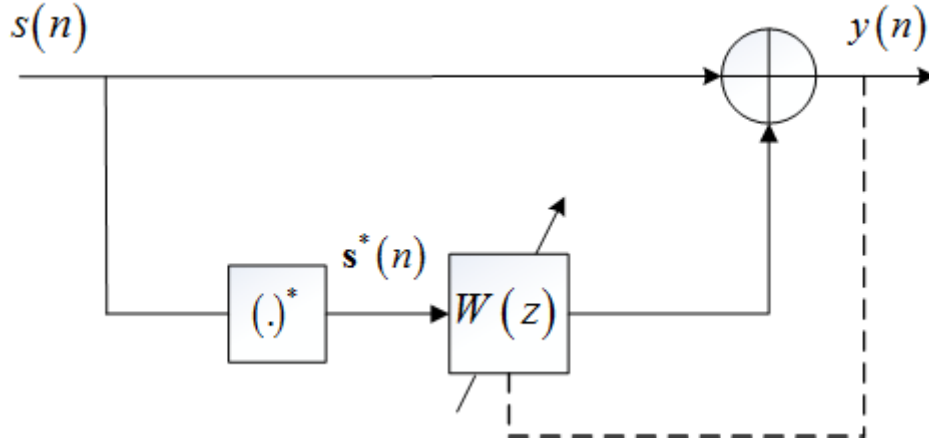


Figure 5-2. Adaptive IQ Imbalance Compensator

Now, the problem boils down to finding the coefficients of the IQI compensation filter. The optimal solution for the IQI compensation filter in Section 5.5 is derived by making the signal at the output of the IQIC proper. So, the idea is to realize a blind-adaptive filter as shown in Fig. 5-2 that updates its coefficients and makes the IQIC output proper, i.e. $E[y(n)y(n+l)] = 0, \forall l$.

The error metric used to update the filter coefficients $\mathbf{w}(n)$ is the difference between the CACF of the signal calculated over the lags equal to the number of filters taps and the expected ideal value of a “zero vector”. The following is the filter coefficient update equation.

$$\mathbf{w}(n+1) = \mathbf{w}(n) - \mu(E[\mathbf{y}(n)y(n)]) \quad (5.50)$$

where μ is the step-size and $\mathbf{y}(n) = [y(n), y(n-1), \dots, y(n-N+1)]$. Approximating $E[\mathbf{y}(n)y(n)]$ with instantaneous values of $\mathbf{y}(n)y(n)$, leads to an LMS like algorithm [23].

$$\mathbf{w}(n+1) = \mathbf{w}(n) - \mu \mathbf{y}(n) y(n) \quad (5.51)$$

By choosing individual step sizes rather than the same μ , the step size matrix can be written as

$$\mathbf{D}(\boldsymbol{\mu}) = \text{diag}[\mu_1, \mu_2, \dots, \mu_N] \quad (5.52)$$

where $\mu_{\min} < \mu_i < \mu_{\max}$ and $\mu_{\max} < \frac{1}{\lambda_{\max}}$, with λ_{\max} being the maximum eigenvalue of the autocorrelation matrix of the input signal \mathbf{s}_n^* to the adaptive subsystem of the IQIC. μ_{\min} is chosen according to the desired steady state misadjustment [43, 44]. Using individual step sizes provides faster convergence and less misadjustment than using a constant μ for this LMS style algorithm [43]. Algorithms that achieve faster convergence, such as RLS, are hardware intensive for a larger number of taps, and this individual step size based algorithm improves the convergence speed with minimal increase in the hardware complexity [44].

The final blind-adaptive algorithm is summarized as below.

$$\begin{aligned} y(n) &= s(n) + \mathbf{w}^T(n) \mathbf{s}^*(n) \\ \mathbf{w}(n+1) &= \mathbf{w}(n) - \mathbf{D}(\boldsymbol{\mu}) \mathbf{y}(n) y(n) \end{aligned} \quad (5.53)$$

The convergence of the algorithm towards the optimal solution $W_{OPT}(z)$ instead of $1/W_{OPT}^*(z^*)$ is guaranteed by initializing all the taps with zeros [23]. From Fig. 5-2, observe that the output is made proper by passing the conjugate version of the signal through the adaptive filter and then adding the adaptive filter output to the IQ imbalanced signal. Inherently during the addition, the image component present in the signal is being cancelled by the output of the adaptive filter. So, the error criterion is decreasing with time from the value it started with when all filter taps were zeros. The optimal solution is where the error criterion achieves its minimum on the convex surface traced by the algorithm, so the adaptive solution always converges to the optimal solution.

5.7 Image Rejection Ratio after Adaptive Filter

Ideally the image rejection of the RF front-end must be infinite but as shown in Sections 3.4 and 3.5, IQ imbalance leads to finite IRR values, thus limiting the performance of the transceivers. The adaptive filter model works towards regaining the lost properness of the signal due to IQI which directly correlates to image suppression. So, the IRR after IQIC is used as a measure of performance.

From (5.41), the IRR after IQIC can be written as

$$IRR_{AF}(f) = \frac{|G_1(f) + W(f)G_2^*(-f)|^2}{|G_2(f) + W(f)G_1^*(-f)|^2} \quad (5.54)$$

In summary, a method is introduced in this chapter that utilizes second order statistical signal properties like circularity and properness, and blindly estimates the IQI compensation parameters, i.e. without the need of any known sequence or signal generators. In addition, the method introduced is online, i.e. it happens in parallel without obstructing the normal functioning of the transceiver. The adaptive nature of the solution makes it capable of tracking the time varying changes in IQI due to temperature and component aging effects. In this next chapter, the performance of the technique that was introduced is validated through computer simulations.

CHAPTER 6 PERFORMANCE SIMULATIONS AND ANALYSIS

In this chapter, a detailed performance analysis of the IQI estimation and compensation technique discussed in Chapter 5 is presented. The Image Rejection Ratio (IRR) is used as the primary performance metric as it quantifies the amount of image suppression achieved. The suppression of the image improves the signal quality and therefore can be correlated to the symbol error rate (SER), which is another metric used in the analysis.

6.1 IQ Imbalance Parameters

IQ Imbalance limits the image rejection capabilities of transceivers, so transceivers will not be able to reject image spectral content completely and practical values of IRR fall in the range of 20-40 dB. The aim in this section is to choose appropriate IQ imbalance parameters so that the front-end IRR values lie in the practical range of 20-40 dB.

Gain mismatch of 3% and mixer phase mismatch of 3° are assumed for all the simulations which contribute to the frequency independent IQI. $H_I(z) = 0.98 + 0.03z^{-1}$ and $H_Q(z) = 1 - .005z^{-1}$ are considered for the I/Q path filter non-idealities which cause FD IQI (Fig. 6-1). In practice, these I/Q filters are generally 3rd to 5th order analog filters, Butterworth or Chebyshev, but in simulations their effects are approximated using short length FIR filters in order to create a similar equivalent imbalance effect (Fig. 6-1).

The front-end image rejection ratio given the imbalance sources introduced is shown in Fig. 6-1. The frequency responses of the I/Q imbalance filters are also shown in Fig. 6-1 and can be shown to closely replicate the differences between the monotone passband behaviors of very similar analog Butterworth filters.

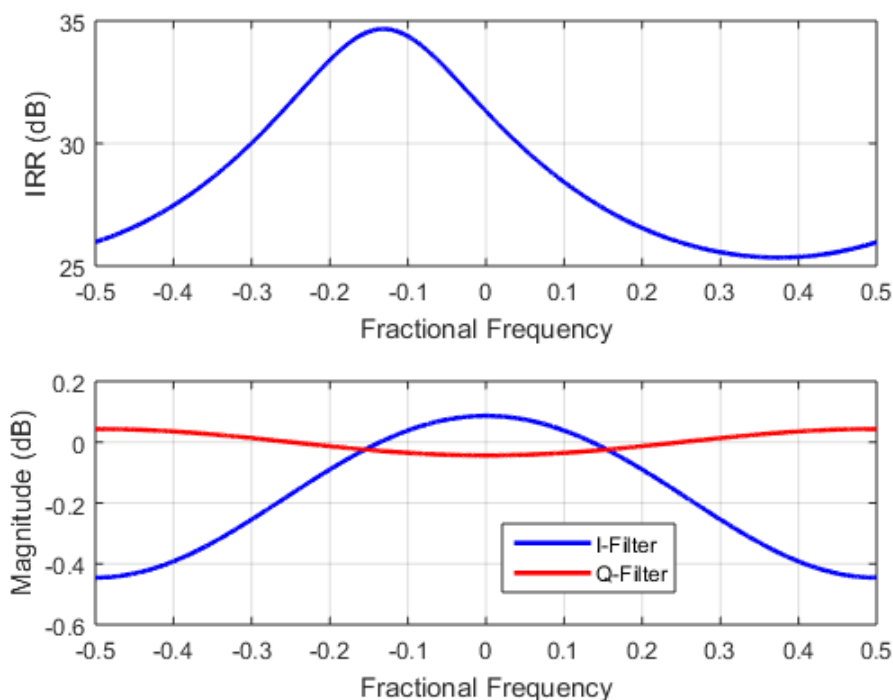


Figure 6-1. Front-end IRR and I/Q Imbalance Filters

6.2 Operating Signal Model

In the case of a single channel with carrier at baseband, the signal will be affected by its own image. The variations in the strength of this image across the band of the signal is dictated by the front-end IRR. However due to strong DC effects, signals are not often transmitted with the carrier at baseband. So, the major source of an image in an IQI scenario would be from the mirror carrier frequency.

The wide band RF bandpass filter simultaneously allows signals at multiple carrier frequencies and due to IQ imbalance all these signals form images at their mirror carrier frequencies. In general these signals tend to have different powers and different bandwidths. A model with two signals at mirror carrier frequencies is considered for the simulations. The two signals as shown in Fig. 6-2 are wideband and are of equal bandwidth, together occupying around 70% of the Nyquist range. The power difference between the two signals is 20 dB.

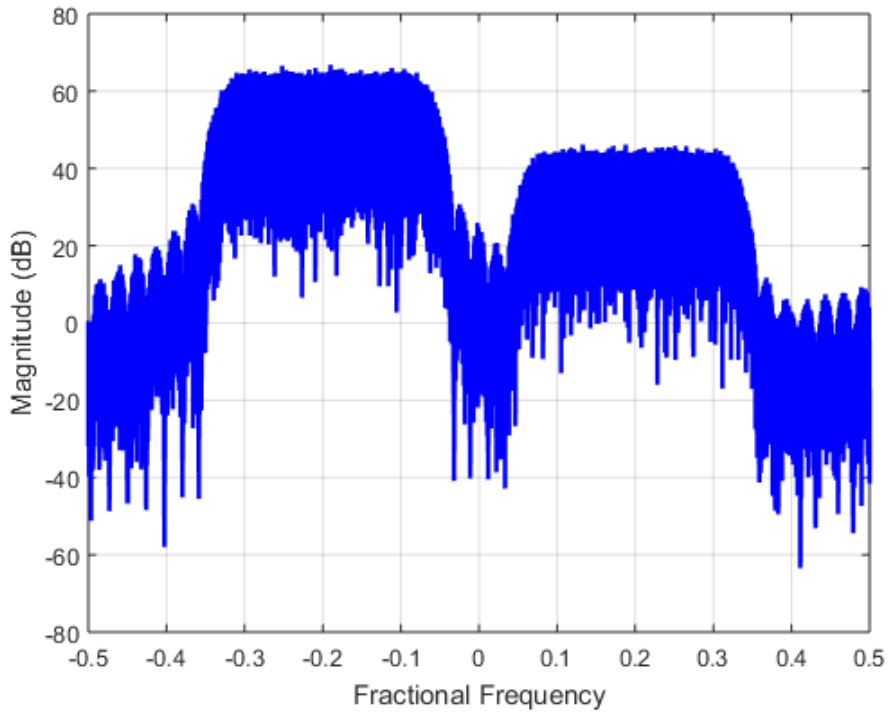


Figure 6-2. Operating Signal Model

The signal carriers being exact mirror frequencies, a very severe and challenging IQ Imbalance scenario is created as illustrated in Fig. 6-3.

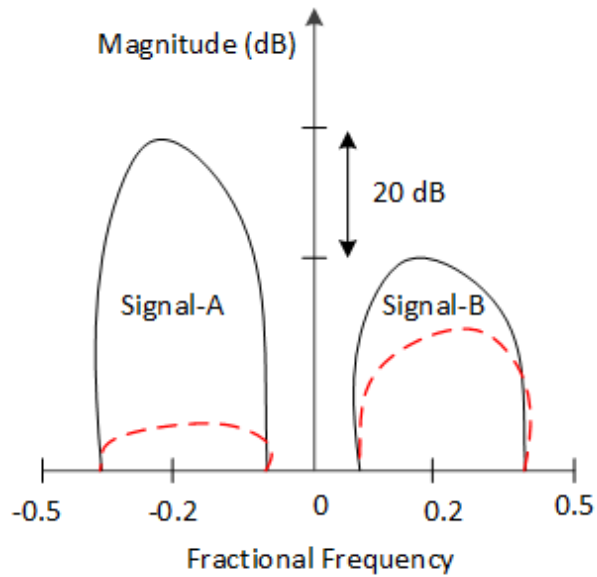


Figure 6-3. Signal and Image Strengths due to IQ Imbalance

Figure 6-3 shows the relative strengths of signal-A and signal-B, and their corresponding image strengths. The image of signal-A is of significant strength and has a detrimental effect on signal-B whereas the image of signal-B has relatively minor impact on signal-A. The primary focus is to recover signal-B as it has been greatly affected by the mirror image interference.

For most of the performance analysis, the 16-QAM modulation scheme is considered for both signals, with raised cosine pulse shaping of 25% roll-off factor. The SNR mentioned is always with respect to the signal of interest.

6.3 Impact of IQ Imbalance on Signal Constellation

Error Vector Magnitude (EVM) is the most commonly used metric to quantify the impact of RF impairments on the constellation of the baseband signal. EVM is a measure of how far the constellation points of the distorted signal are from their ideal positions. So smaller EVM implies better signal quality.

In higher order modulation schemes, like 64 QAM, the distance between the constellation points is less so for the same amount of distortion, higher order modulation schemes require better EVM in comparison to lower order modulation schemes, like QPSK.

Before discussing the impact of IQ imbalance on signal constellations in the scenario under consideration, the effects of generic phase, gain, phase-gain imbalances are shown in Fig. 6-4. Relatively high values for gain imbalance (15%) and phase imbalance (10^0) are considered in order to visually depict their impact on the constellations.

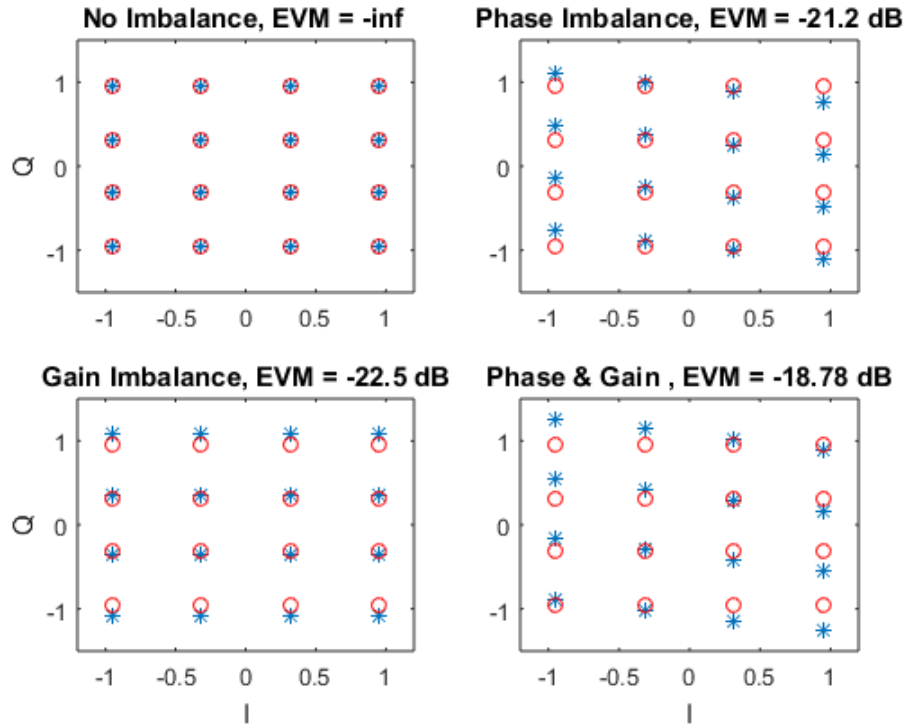


Figure 6-4. Effect of Gain and Phase Imbalances

The theoretical value for EVM because of IQ imbalance is given by [16]

$$EVM_{IQ} = \sqrt{\frac{(g-1)^2 + \phi^2}{4}} \quad (6.1)$$

where g and ϕ are the relative gain and phase imbalances as defined in (3.14).

In Fig. 6-4, calculated EVM values are shown in the title above the corresponding constellations. Observe that the image signal formed during IQI distorts the signal constellation by both rotating (phase imbalance) and shifting (gain imbalance) which results in the degradation of EVM by moving constellations away from their ideal locations (the red circles in Fig. 6-4).

Gain imbalance of 3% and phase imbalance of 3° are considered for the simulations of the considered scenario, the resultant EVM with both gain and phase imbalance is

-30.477 dB which is exactly equal to the frequency independent IRR value (Fig. 3-9). IQ imbalance originating from I/Q lowpass filters because of its frequency selective nature impacts EVM of the signal differently at different parts of the Nyquist range. In this way image rejection can be quantitatively related to the distortion on the signal constellation (EVM). In practice it is not possible to calculate IRR values as IRR is a function of IQI impairments introduced by the operating hardware, so EVM can serve as the proxy measure of performance of the IQIC.

The following Fig. 6-5 shows the constellation of signal-A after introducing IQ imbalance.

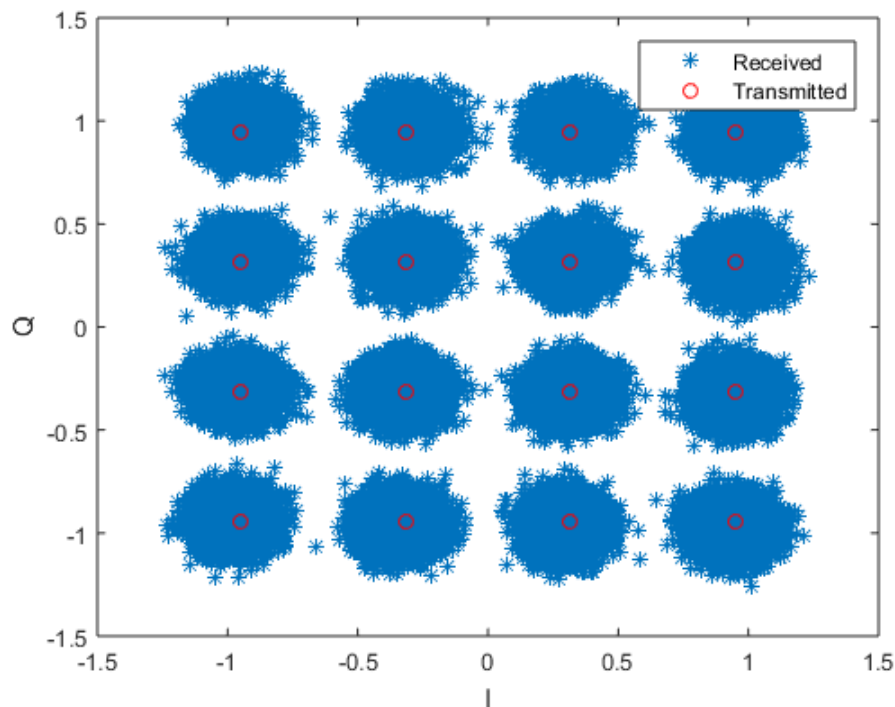


Figure 6-5. Constellation of Signal-A at 20 dB SNR with IQI

As can be observed from Fig. 6-5, signal-B's image has only a minor effect on signal-A's constellation whereas the effect of the stronger image of signal-A on signal-B's constellation is clearly evident from Fig. 6-6.

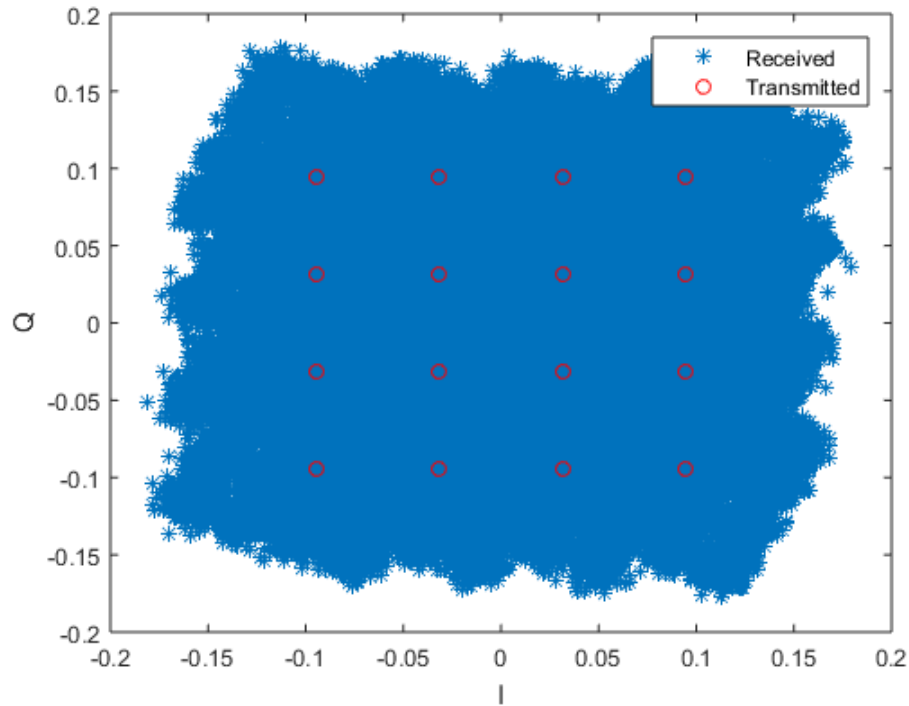


Figure 6-6. Constellation of Signal-B at 20 dB SNR with IQI

The aim of the adaptive filter would be to improve the quality of the weaker signal by providing sufficient image rejection and thereby bringing corresponding improvements to the SER performance of 16-QAM. Later in Section 6.6, with the achieved image rejection, the SER performance improvements on other modulation schemes, like QPSK and 64-QAM, is evaluated.

6.4 1-tap and 3-Tap AF Performance Comparison

In order to mitigate the effects of IQ Imbalance depicted in Sections 6.2 and 6.3, the IQI affected signal is fed to the IQIC described in Section 5.6. The performance resulting from 1-tap and 3-tap adaptive IQI compensators is evaluated based on the image rejection provided. Furthermore, the evaluation is extended with SER as the metric.

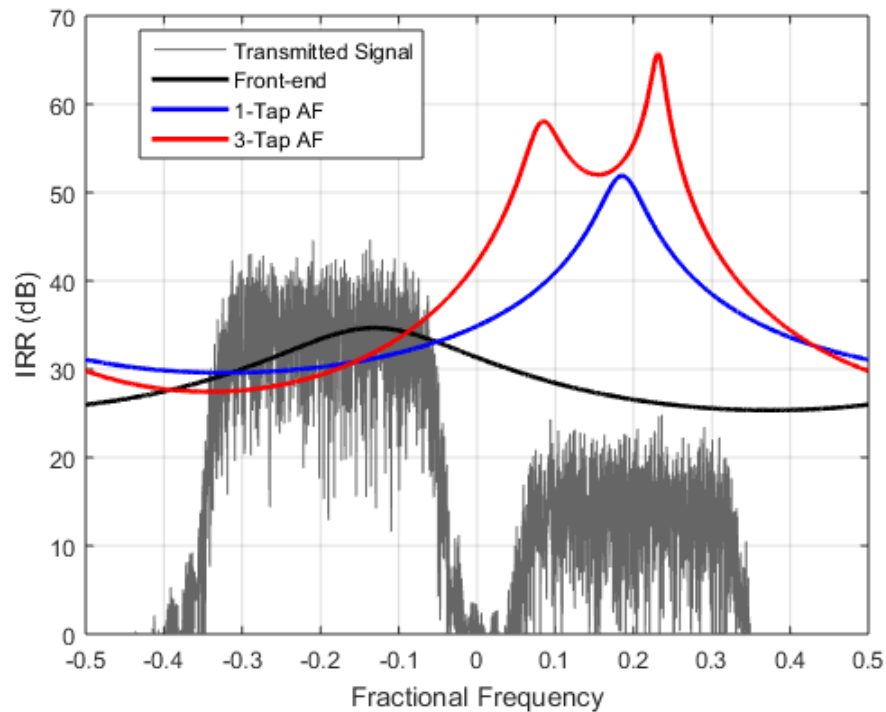


Figure 6-7. IRR after 1-tap and 3-tap Adaptive IQI Compensators

From Fig. 6-7, it is interesting to note that the adaptive IQI compensators improve the IRR values at the frequencies where the signal is severely distorted by IQI, which can be directly attributed to the properness criterion of the signal on which the adaption is based. The component signals are depicted in the background of Fig. 6-7 to indicate their location in the frequency spectrum; the y-axis scale (dB) corresponds to their relative, not absolute, strength.

The 3-tap adaptive IQIC boosts the IRR values across the complete range of signal-B (the weaker signal). The 1-tap adaptive IQIC on the other hand, although producing good IRR values, is more limited in its range. So, one can conclude that a 1-tap adaptive IQIC works for narrowband signals whereas a higher number of taps is required for wideband signals with frequency selective IQ imbalance. Figures 6-8 and 6-9 show the constellations of signal-B after 1-tap and 3-tap adaptive IQI compensators.

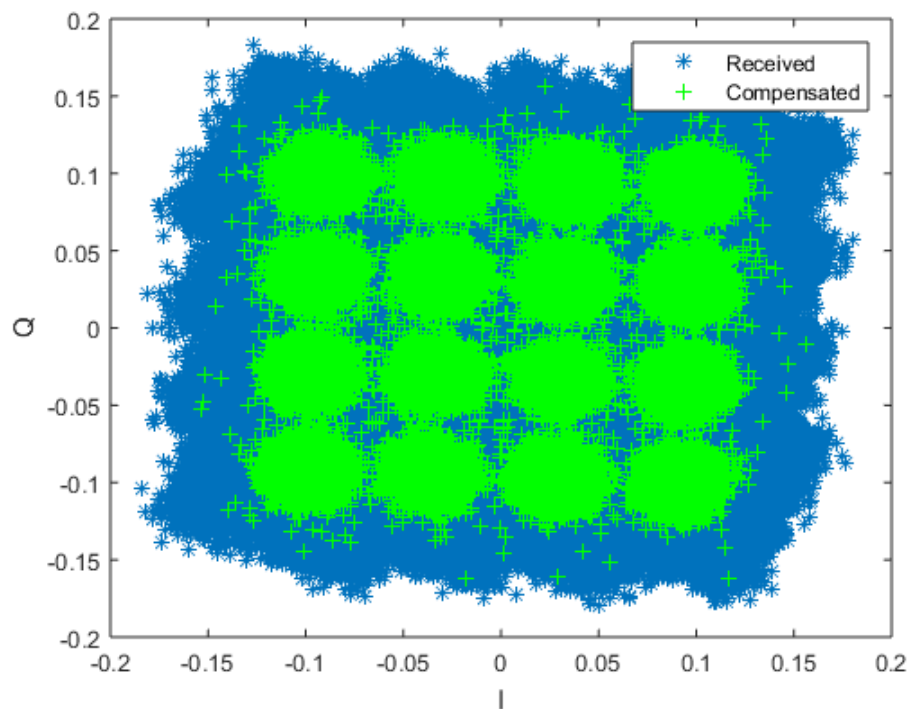


Figure 6-8. Constellation of Signal-B after 1-tap Adaptive IQIC

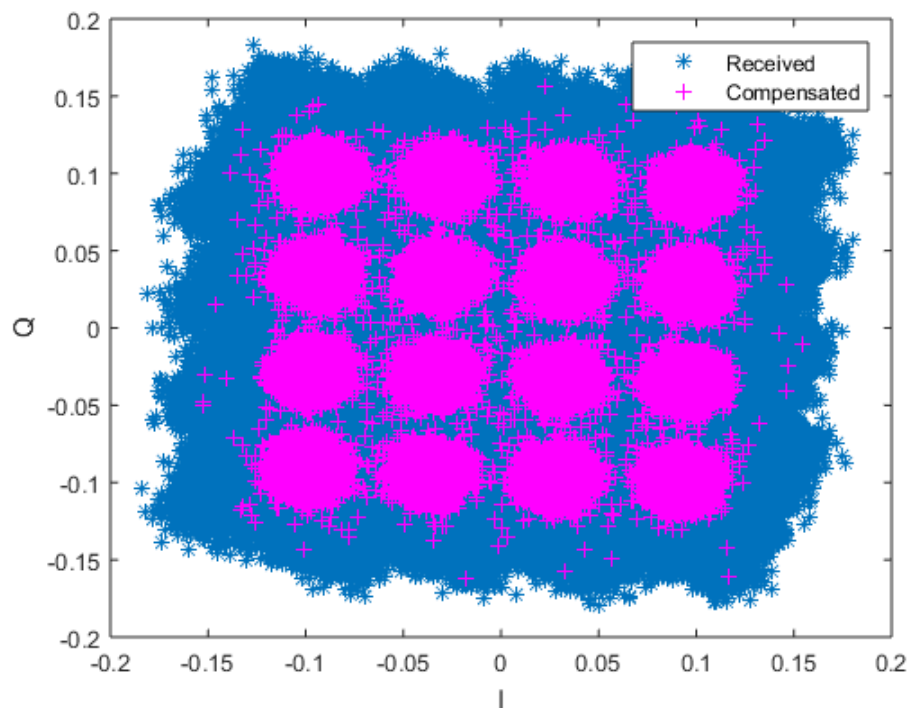


Figure 6-9. Constellation of Signal-B after 3-tap Adaptive IQIC

The constellations of signal-B in Figures 6-8 and 6-9 show clear improvement compared to the IQI distorted constellation in Fig. 6-6 which can be directly correlated to an increase in the image rejection ratio over the frequency band of signal-B. In Fig. 6-10, the SER of signal-B with and without IQI compensation is compared with AWGN 16-QAM performance.

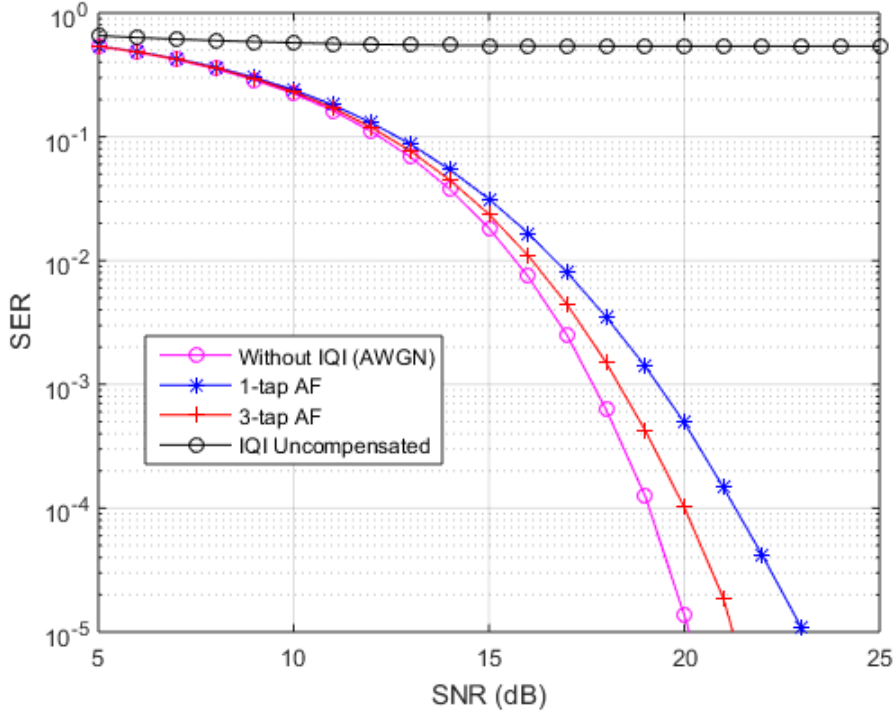


Figure 6-10. SER Comparison of 1-tap and 3-tap Adaptive IQICs

The SER performance (Fig. 6-10) based on the IQI compensated signal is limited by the distortion term discussed in Section 5.5; this is the reason for the 3-tap Adaptive Filter (AF) IQIC not being able to match AWGN performance even after achieving sufficient IRR for 16-QAM. This distortion is equalized and the corresponding results are presented in Section 6.6. The rationale behind choosing 3-taps for the adaptive filter is explained in the next section.

A step size of $10^{-4}/P$ and step size matrix $\mathbf{D}([1, 0.5, 0.5])10^{-4}/P$ are used for the 1-tap and 3-tap adaptive filters respectively [23], where P is the power of the signal input to IQIC.

6.5 Optimal Filter Performance

In Section 6.3, the performance after 1-tap and 3-tap adaptive IQI compensators is evaluated. The idea in this section is to come up with the (near) optimal number of taps required for the FIR approximation of the optimal solution discussed in Section 5.5. The optimal solution that completely removes the image component is a function of the specifics of the IQ imbalance introduced. Substituting the introduced impairment parameters in the expression of the optimal solution given in (5.47) results in an IIR filter as shown below.

$$\begin{aligned}
 W_{OPT}(z) &= \frac{-G_2(z)}{G_1^*(z^*)} \\
 &= \frac{(0.0486+0.0539i) + (-0.0593-0.0005i)z^{-1} + (0.0372 + 0.0004i)z^{-2}}{(2.0086+0.0539i) + (0.0407 - 0.0005i)z^{-1} + (-0.0228 + 0.0004i)z^{-2}}
 \end{aligned} \tag{6.2}$$

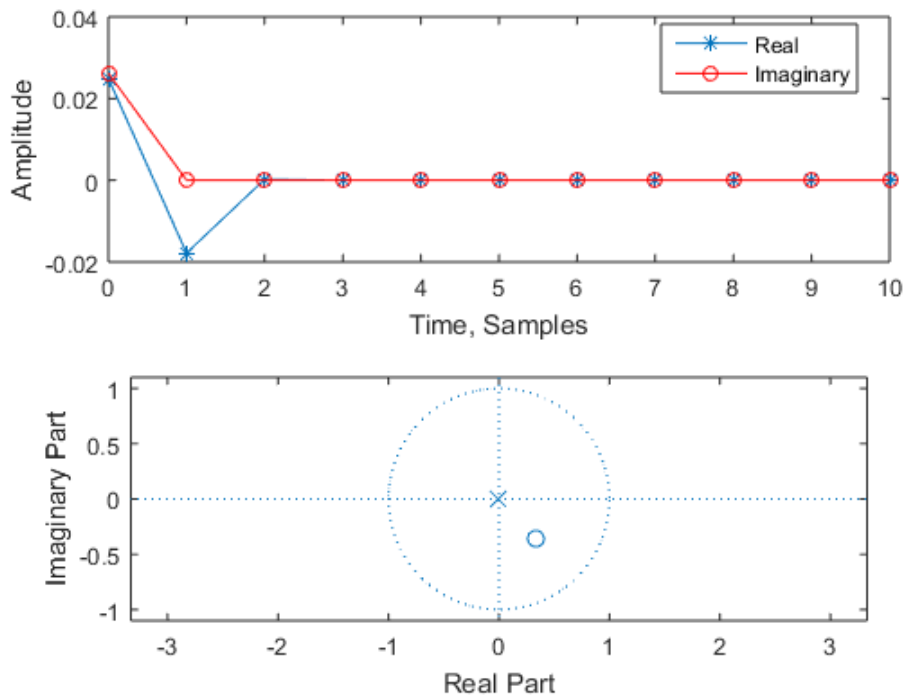


Figure 6-11. Unit Impulse Response and Pole-Zero Plot of Optimal Filter

Figure 6-11 shows the impulse response, and the poles and zeros, of the optimal IIR filter. Observe that the pole is very close to the z-plane origin and that the unit pulse response has effectively only three significant coefficients, thereby leveraging the opportunity to accurately approximate the optimal IQI compensator using a 3-tap FIR filter. Table 6-1 shows the three significant complex coefficients of the optimal filter.

Table 6-1. Coefficient Values of FIR Approximated Optimal Filter

Coefficient	b_0	b_1	b_2
Value	$0.0249 + 0.0262i$	$-0.0178 + 0.0000i$	$0.0002 - 0.0000i$

The image rejection ratio after optimal IIR IQI compensation would be infinite but the IRR after the compensator with 3-tap FIR approximation of the optimal filter will not be infinite, as there will still be a residue of the image. The effect of the residual image is reflected in the IRR simulation results shown in Fig. 6-12.

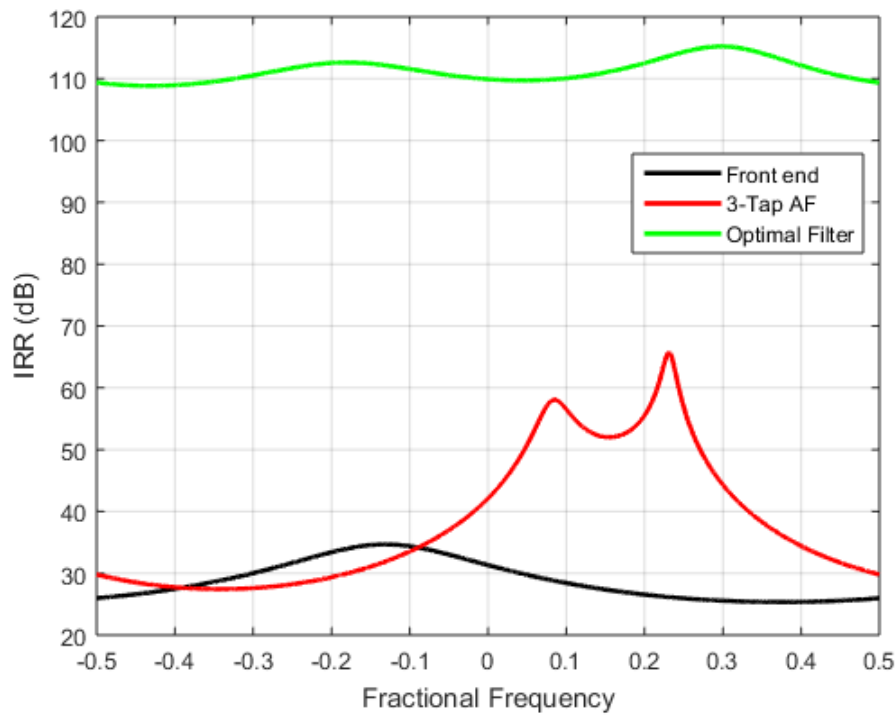


Figure 6-12. IRR after Optimal IQIC

The compensator with 3-tap FIR approximation of the optimal filter has an IRR value of around 110 dB across the entire frequency range. Furthermore, an IRR value of 110 dB which corresponds to EVM value of -110 dB is sufficient to successfully decode even higher order modulation schemes like 256 QAM [16, 45]. The latter implies that – for now – it is enough to build compensators that aim to approximate this FIR version of the optimal filter rather than the more complex IIR version.

The 3-tap FIR approximation of the optimal filter is referred to as the optimal filter (OF) from this point onwards. In Fig. 6-13 the SER performance of the optimal IQIC and the 3-tap adaptive IQIC are compared for a wideband 16-QAM input.

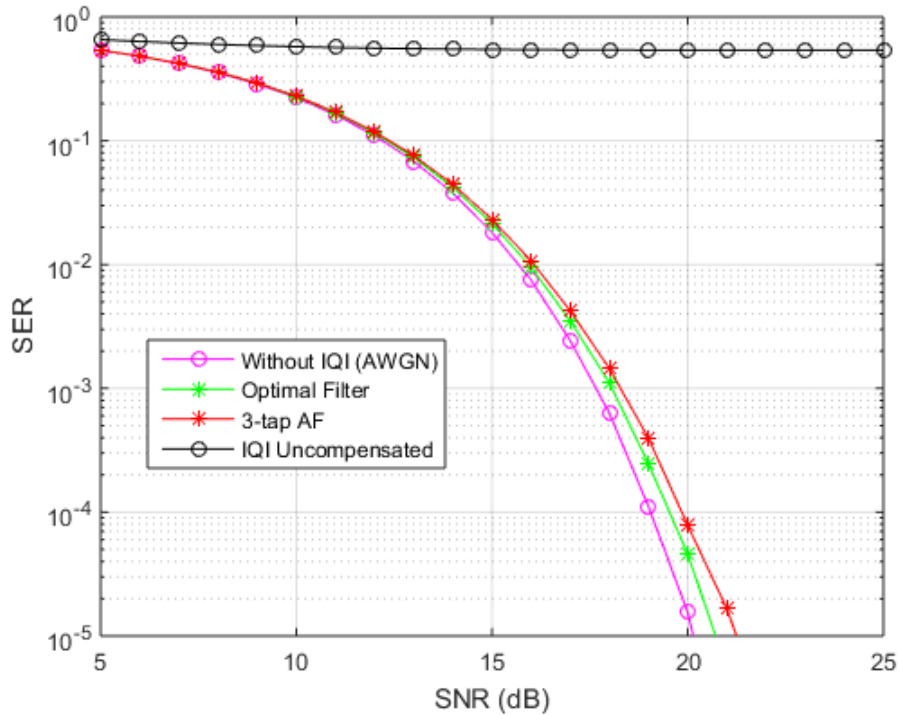


Figure 6-13. SER of Optimal IQIC for 16-QAM

It is interesting to note that even with such high IRR values the SER of the optimal IQIC is not equal to the AWGN performance for 16-QAM. As mentioned in Section 6.3, this is due to the distortion component acting on the signal of interest. Furthermore, the optimal

IQIC and the 3-tap adaptive IQIC produce SER that are very close, indicating that the IRR value of 55 dB achieved by the adaptive IQIC filter is sufficient for 16 QAM.

IRR values obtained after adaptive IQIC presented up until this point are based on the adaptive filter coefficients in the steady state. For the input signal in Fig. 6-2, the 3-tap adaptive filter takes around 20,000 samples (Fig. 6-14) to converge. Assuming a moderate sampling frequency of 20 MHz, the time will be approximately 1 millisecond.

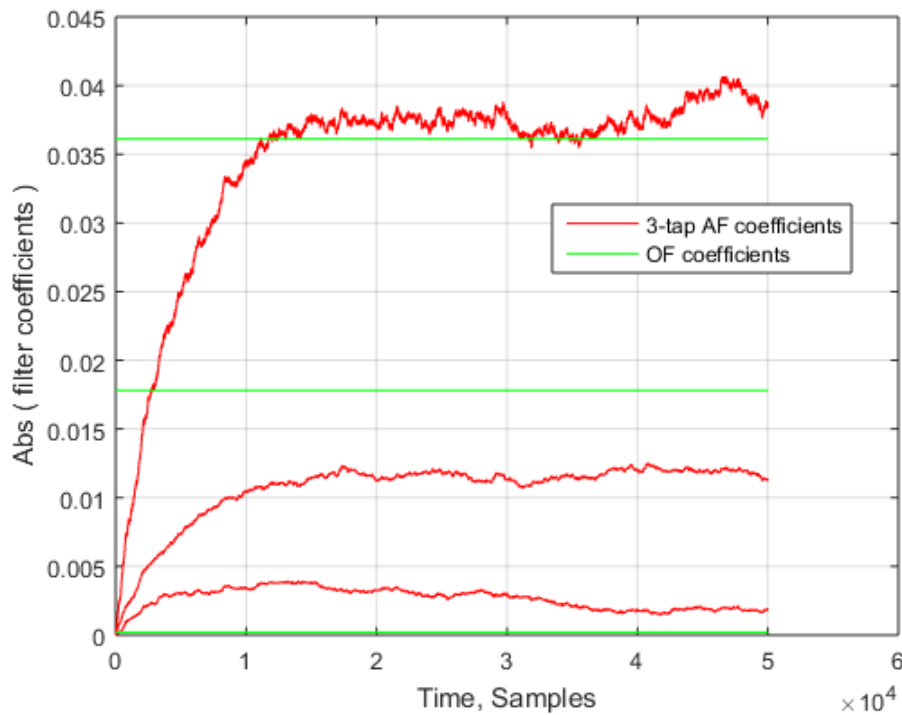


Figure 6-14. Adaptive vs Optimal Filter Coefficients

From Fig. 6-14, observe that the coefficients of the adaptive filter do not necessarily approach the coefficients of the optimal filter; this is because the adaptive filter updates its coefficients based on the input signal, and the input signal in this scenario is limited in its spectral content, i.e. the spectral content is not rich enough to drive the adaptation perfectly towards the optimal filter coefficients. The reason behind the jitter in the steady state of the adaptive filter is explained in Section 6.10.

6.6 Equalization for the Distortion Component

As observed in Sections 6.5 and 6.6, the SER performance resulting from the optimal and adaptive IQI compensators is affected by the distortion component acting on the signal of interest, given in (5.43) as

$$Y(f) = \left(G_1(f) - G_2^*(-f) \left(\frac{G_2(f)}{G_1^*(-f)} \right) \right) Z(f)$$

The following Fig. 6-15 shows the SER performance of the compensators for a QPSK modulated signal.

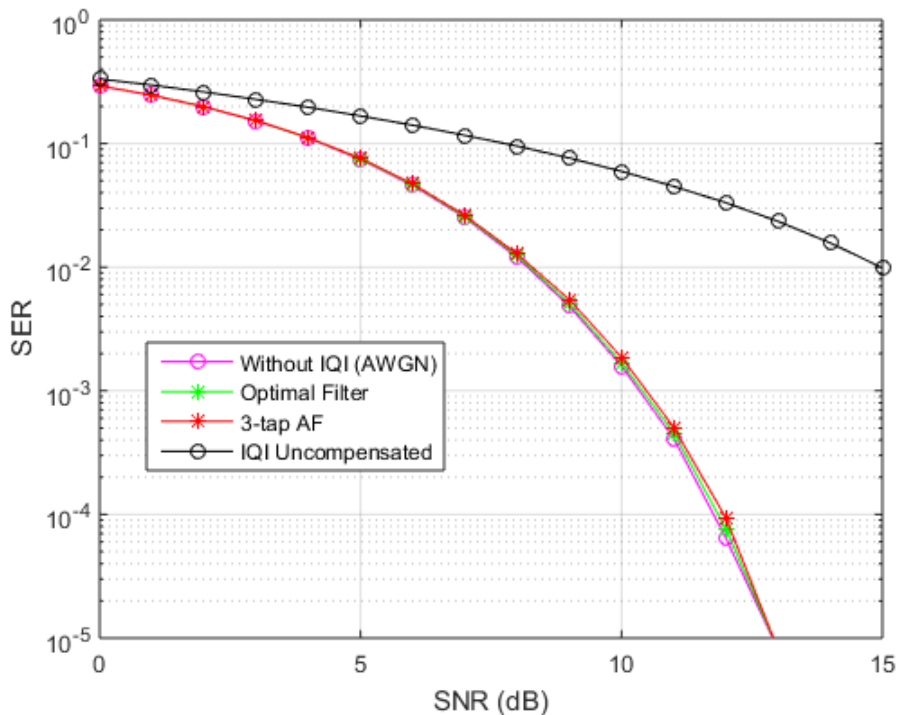


Figure 6-15. QPSK SER Performance

The effect of distortion is not significant on QPSK (Fig. 6-15) as there is enough distance between the symbols in its constellation and QPSK is thus very robust to distortion. Similar to distortion, the constellation of QPSK is less sensitive to image frequency

interference, so that the IRR achieved with a 3-tap adaptive IQIC is good enough for its SER performance to be on par with optimal and AWGN scenarios.

The distortion shows its impact more for higher order modulation schemes, as is evident in the 16-QAM case illustrated in Fig. 6-13, with a loss of around 0.7 dB with optimal IQIC. As expected, the effect of distortion increases for 64-QAM (Fig. 6-16).

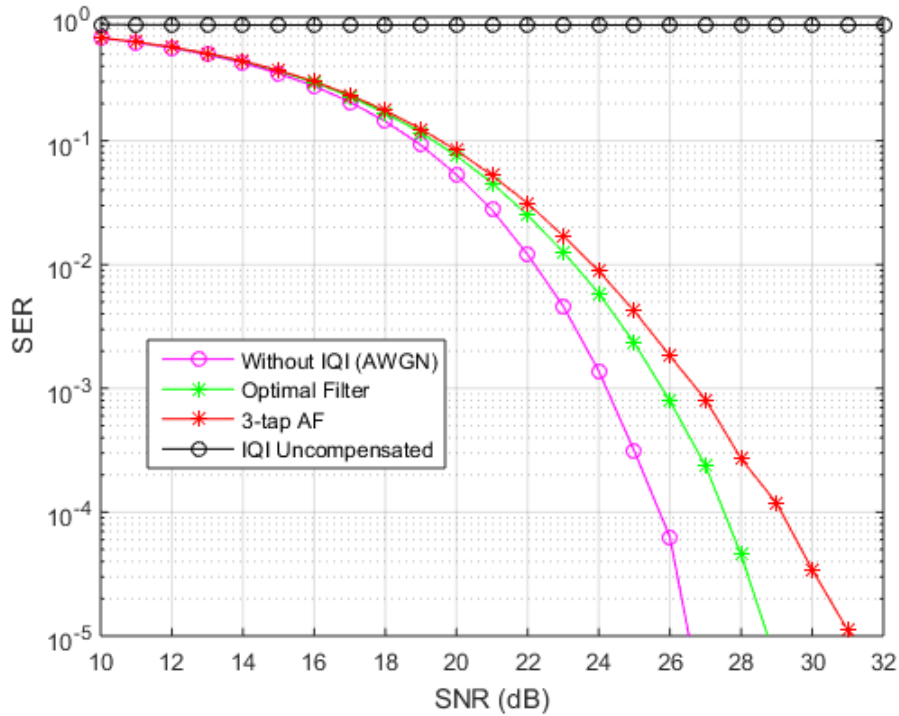


Figure 6-16. 64-QAM SER Performance

Observe that 64-QAM is very sensitive to the distortion, with a loss of around 2 dB with respect to the optimal IQIC. The distortion equalized SER performance is shown in Fig. 6-17. Similar improvement can be shown in the 16-QAM case as well. If desired, in practice, this distortion mitigation may inherently be done simultaneous with channel equalization.

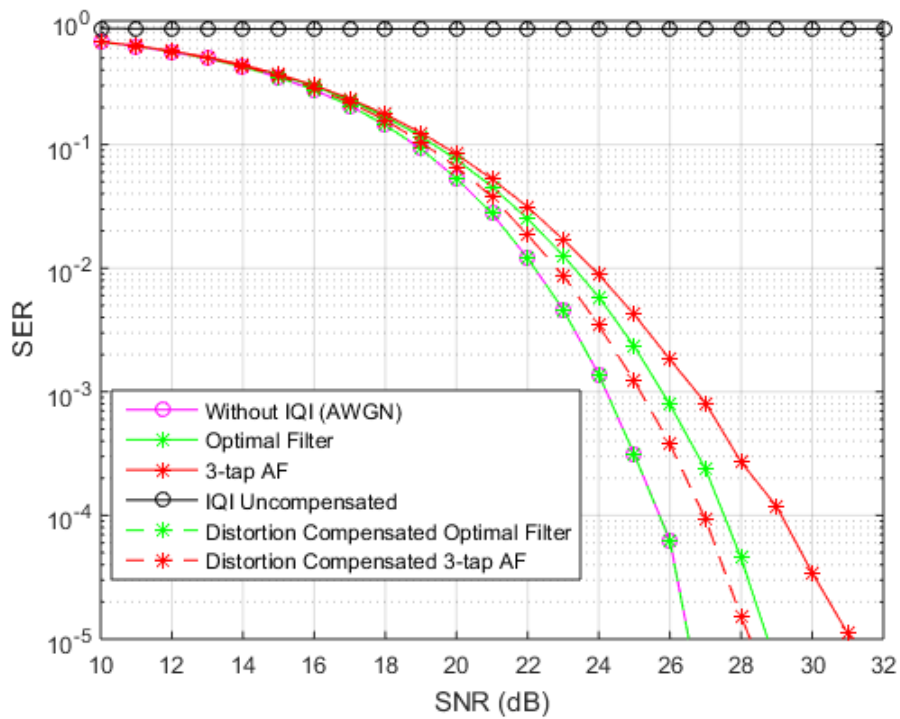


Figure 6-17. 64-QAM SER Performance after Distortion Compensation

As can be observed from Fig. 6-17, an improvement of 2 dB and 3 dB in SER is realized for the optimal IQIC and 3-tap adaptive IQIC respectively after distortion compensation.

6.7 Illustration using White Gaussian Noise

In this section, the behavior of the adaptive IQIC on IQI affected white Gaussian noise which has uniform power across all frequencies, is of interest.

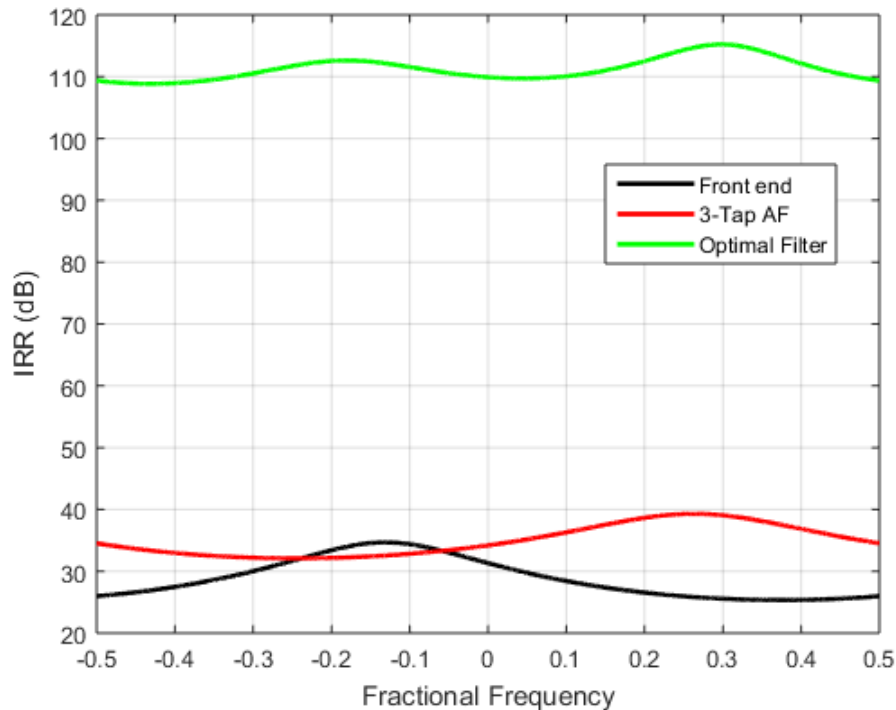


Figure 6-18. IRR Response of Adaptive IQIC Operating on White Gaussian Noise

In this case, the image is spread all across the band as the original signal is present at all frequencies. The image distorts the signal according to the frequency selective nature of the front-end, so as expected, the adaptive filter tries to keep the IRR constant by boosting it at the frequencies where it is affected more (Fig. 6-18). This proves that the adaptive technique can even work on white Gaussian noise originating from the RF circuitry itself for IQI calibration. The adaptive filter coefficients obtained by acting on WGN may not be quite as effective as for a signal with significantly higher image interference (Fig. 6-3); however, the resulting parameters could serve as an intermediate point to continue the adaptation from.

6.8 Time-Varying IQ Imbalance

In this section, the performance of the 3-tap adaptive IQIC under time-varying IQI is validated. Considering the time at which the adaptive filter reaches convergence as t_1 . For the input signal shown in Fig. 6-1, t_1 is around 20,000 samples, as shown in Section 6.5.

After 40,000 samples, the input is changed by swapping the carrier frequencies of signal-A and signal-B, causing a corresponding instantaneous change in the adaption of the filter coefficients from the moment of change in the input signal, as observed in Fig. 6-19.

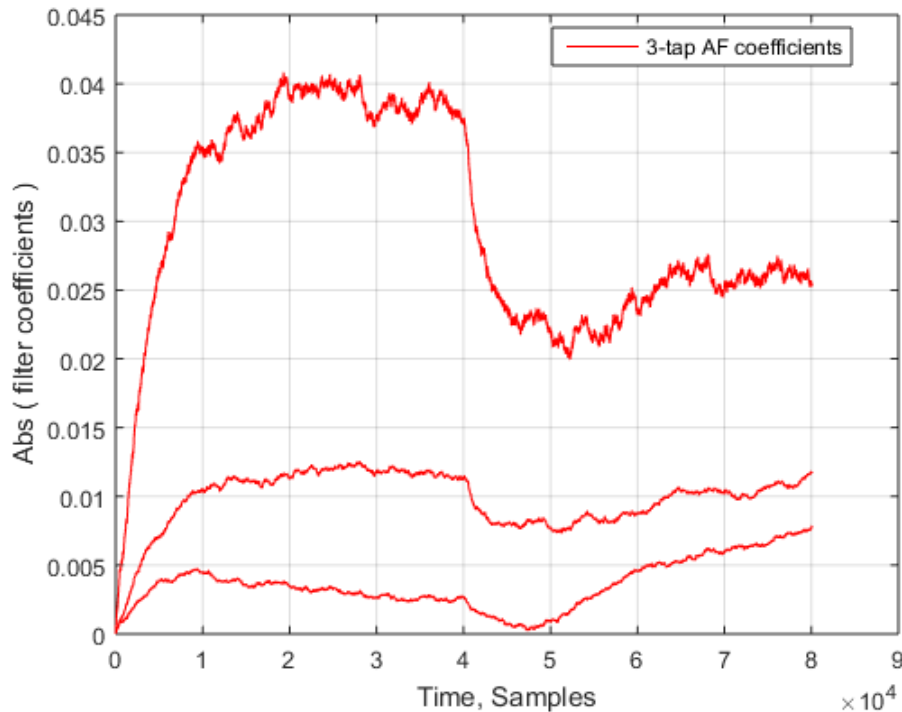


Figure 6-19. 3-tap AF Coefficients under Time-Varying IQI

For the new input, the lower strength signal-B is now centered at negative fractional frequency of -0.2 and will be distorted more due to IQ imbalance; the expectation is that the adaptive filter will then boost the IRR around this frequency of -0.2 instead of around the positive fractional frequency of 0.2. The latter behavior is indeed observed in Fig. 6-20, where the IRR is shown evaluated at several time instants $t_1 < t_2 < t_3 < t_4$. Note that

the IRR boost shifts with time towards the desired frequency range. Here, t_4 is the time when the IQIC produces desired IRR for the new input and occurs around 65,000 samples. t_2 , t_3 are intermittent time values at 45,000 samples and 55,000 samples respectively.

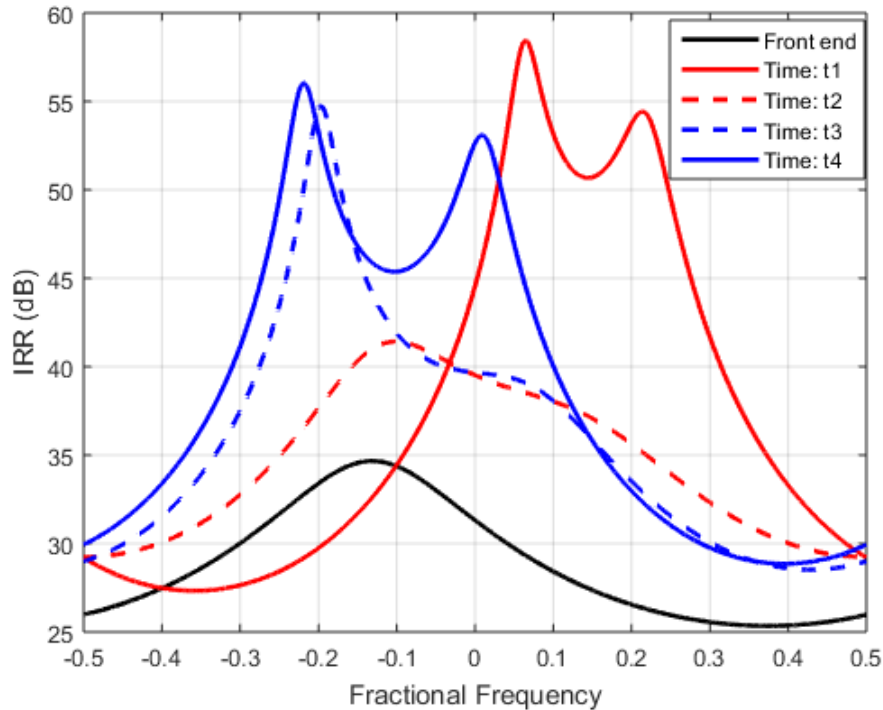


Figure 6-20. IRR changes under Time-Varying IQI

6.9 Error Metric Analysis

All the simulation results presented in the earlier sections are considering fixed step size (of 10^{-4}) for the adaptive algorithm. In this section, the feasibility of a variable step size algorithm is tested for possible advantages it might offer.

The adaptive metric of the implemented adaptive algorithm, i.e. $\mathbf{y}(n)y(n)$, always has some amount of random error associated with it because of the instantaneous approximation of properness $E[\mathbf{y}(n)y(n)]$, so the error power is fluctuating in nature

rather than monotonically decreasing. In this context, a new metric which gives a better estimate of properness is introduced.

Properness at time instant n , can be approximated as

$$E[\mathbf{y}(n) \mathbf{y}(n)] \approx \frac{1}{n} \sum_{i=1}^n \mathbf{y}(i) \mathbf{y}(i) \quad (6.3)$$

where $\mathbf{y}(i) = [y(i), y(i-1), \dots, y(i-l+1)]$ and l is the number of lags considered.

By considering $l=15$, the defined metric is used to measure the extent of properness achieved with time by the IQI compensated signals at the output of optimal and 3-tap adaptive IQI compensators. The same metric is used to measure the properness of the signal without IQI and signal with IQI but uncompensated. All the calculated values of the metric are plotted versus time in Fig. 6-21.

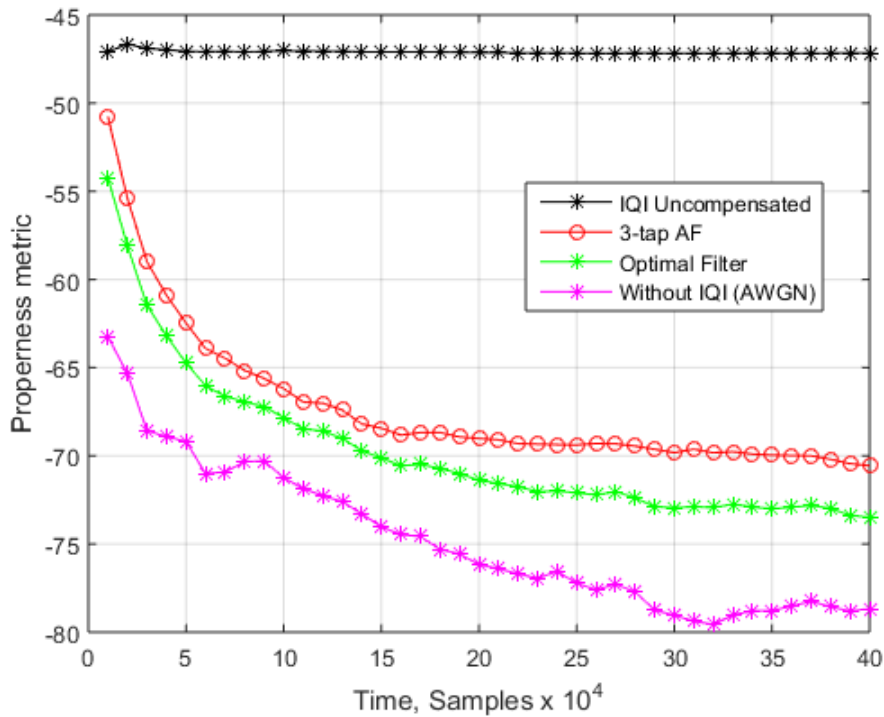


Figure 6-21. Measure of Properness

As expected, the uncompensated IQI signal has comparatively high values for the properness measure for all time whereas the optimal and 3-tap adaptive IQI compensators are making the signal more proper with time. The extent of properness achieved by the IQI compensators can be inversely related to their corresponding IRR values (Fig. 6-12).

A variable step size adaptive algorithm is developed using the metric defined in (6.3) as the error measure for properness (instead of the instantaneous approximation), as shown below

$$\begin{aligned}
 y(n) &= s(n) + \mathbf{w}^T(n) \mathbf{s}^*(n) \\
 \mu_n &= \alpha \mu_{n-1} + \frac{1}{l} \left\| \frac{1}{n} \sum_{i=1}^n \mathbf{y}_l(i) y(i) \right\|^2 \\
 \mathbf{w}(n+1) &= \mathbf{w}(n) - \frac{\mu_n}{n} \sum_{i=1}^n \mathbf{y}(i) y(i)
 \end{aligned} \tag{6.4}$$

where $\mathbf{y}_l(i) = [y(i), y(i-1), \dots, y(i-l+1)]$, l is the number of lags considered, $\mathbf{y}(i) = [y(i), y(i-1), \dots, y(i-N+1)]$, and N is the number of filter taps, while α is the forgetting factor.

A fixed step size value of $10^{-4}/P$ is considered, where P is the power of the input signal to the IQI compensator. $\alpha = 0.9$ is considered for the variable step size algorithm.

Figure 6-22 shows the behavior of error power in the fixed and variable step size adaptive filters. As expected the error power in the variable step size algorithm decreases with time unlike the error power in the fixed step size algorithm.

Figure 6-23, depicts the adaptation of step size values in accordance with the changes in the error power. Observe by comparing Fig. 6-23 with Fig. 6-22, that the step size values are initially high when the error power is high and then tend to very low values when the error power decreases.

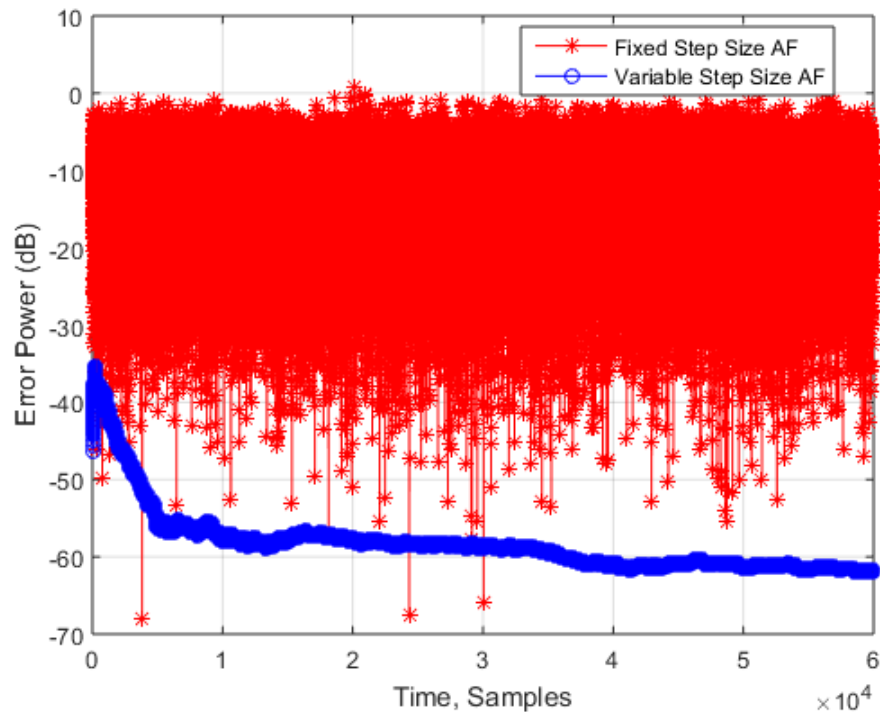


Figure 6-22. Error Power of Fixed and Variable Step Size Adaptive Filters

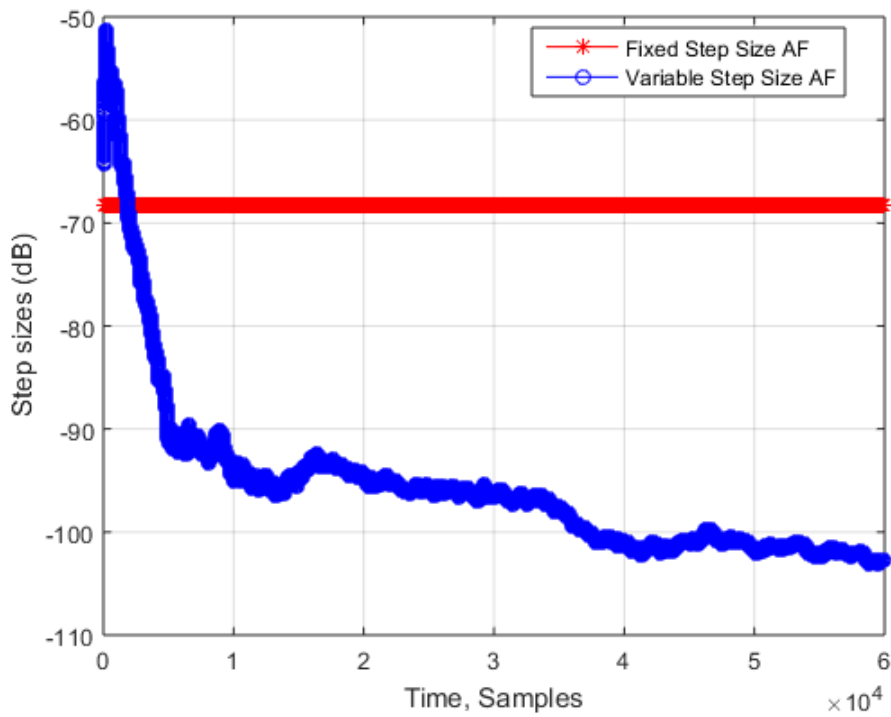


Figure 6-23. Step Sizes of Fixed and Variable Step Size Adaptive Filters

Figure 6-24 shows the adaptation of the filter coefficients with time.

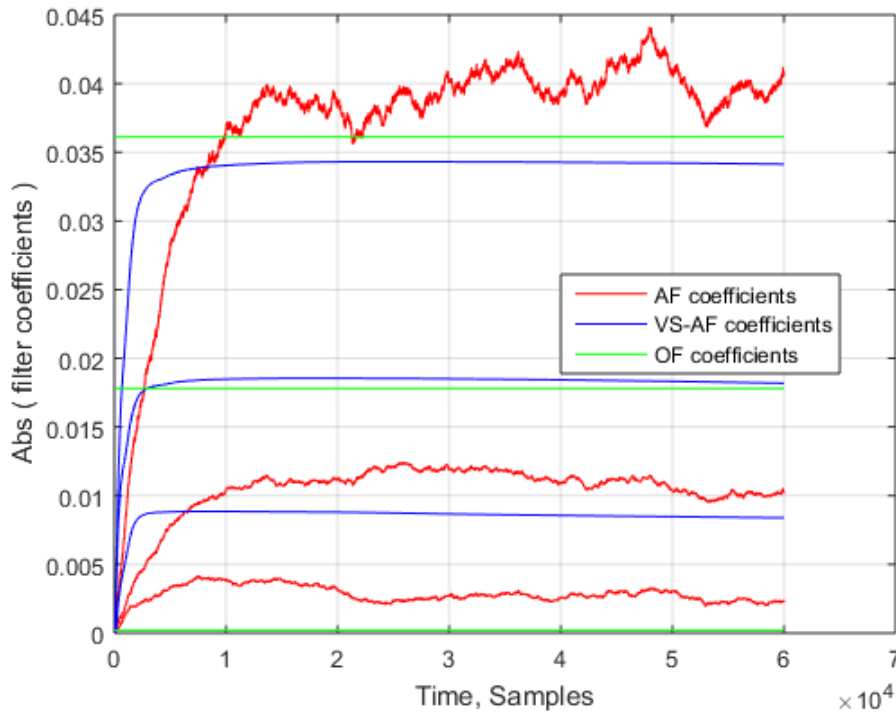


Figure 6-24. Filter Coefficients of Fixed and Variable Step Size Adaptive Filters

Observe from Fig. 6-24 that the VS-AF reaches a certain stage in the adaptation process very fast compared to the fixed step size adaptive filter. However with time, its step sizes and error powers reach extremely low values so that the product that is used to update the filter coefficients gets down to the range of 10^{-12} , and because of these highly insignificant values the adaptation literally stops without ever reaching the best possible state of the coefficients, thus leading to inferior performance.

The fixed step size adaptive algorithm delivers the desired performance and is very hardware efficient. It takes only 20,000 samples to reach the stable state and, in addition, the ability to adapt on noise from RF components reduces the time to reach the steady state. The value of step size can be carefully chosen based on the bit-width of the underlying hardware.

6.10 Illustration using Sinusoidal Inputs

In this section, a signal consisting of a sum of sinusoids spread across the Nyquist range is used as the input and the performance of adaptive IQI compensators using this sinusoidal input is evaluated. The individual sinusoids are chosen such that none of them coincide with any of their mirror frequencies. Figure 6-25 shows sinusoids before and after IQ imbalance.

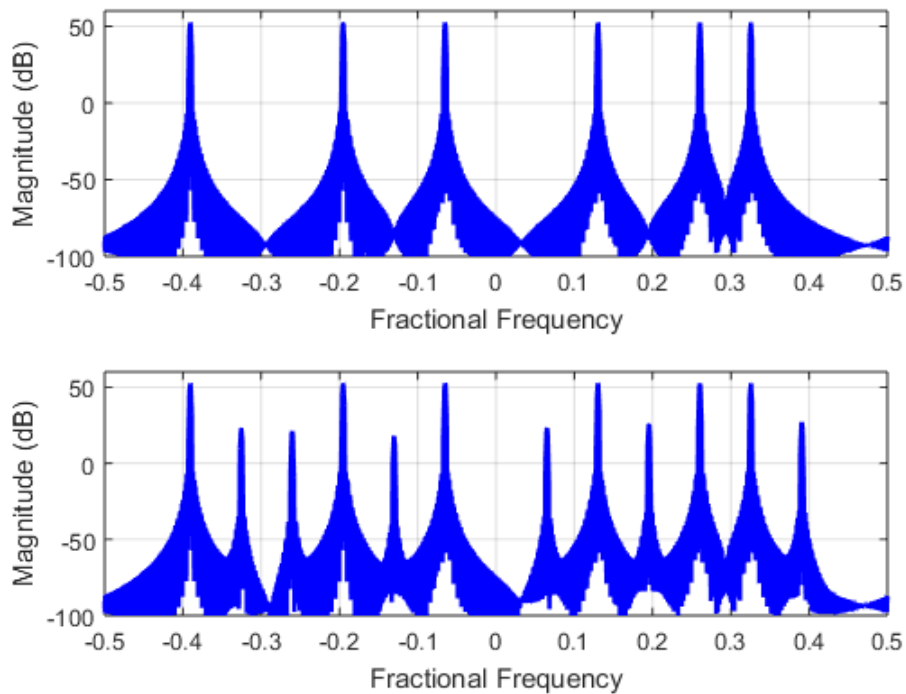


Figure 6-25. Sinusoids Before (top) and After (bottom) IQ Imbalance

The powers of the image components formed due to IQI are about 30 dB lower than the powers of the sinusoids comprising the signal of interest. These relative signal to image strengths are dictated by the front-end IRR as shown in Fig. 6-26. At fractional frequencies where images are formed, image strengths are subtracted from their source signal strengths and compared to corresponding front-end IRR value at those fractional frequencies, the calculations are shown in Table 6-2.

Table 6-2. Sinusoid Signal to Image Strengths vs Front-end IRR

Fractional Frequency	Image (dB)	Signal (dB)	Signal – Image (dB)	IRR (dB)
-0.32	23.18	52.41	29.23	29.2293
-0.26	21.14	52.41	31.27	31.2745
-0.13	17.9	52.41	34.51	34.5129
0.06	23.26	52.41	29.15	29.1525
0.20	25.92	52.41	26.49	26.4914
0.39	27.05	52.41	25.36	25.3612

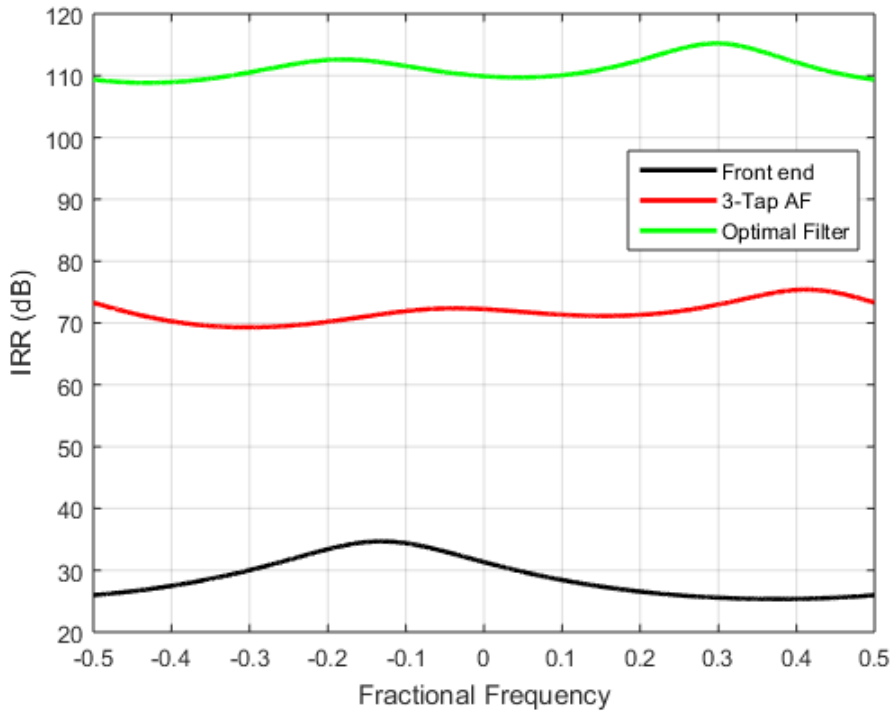


Figure 6-26. IRR Performance with Sinusoidal Input

With sinusoidal inputs, the IRR values obtained by the 3-tap adaptive IQIC are similar across the Nyquist range (Fig. 6-26). The relatively flat IRR response of the 3-tap adaptive IQIC is due to the fact that the sinusoidal input has spectral content spread across the Nyquist range and the fact that the 3-tap AF coefficients can approach the optimal filter coefficients.

The output of the 3-tap adaptive IQIC shown in Fig. 6-27 is during the period when the adaptive filter coefficients are locked to steady state values and the filter is not continuously adapting. The sinusoidal outputs after the 3-tap and optimal IQI Compensators are shown in Fig. 6-27.

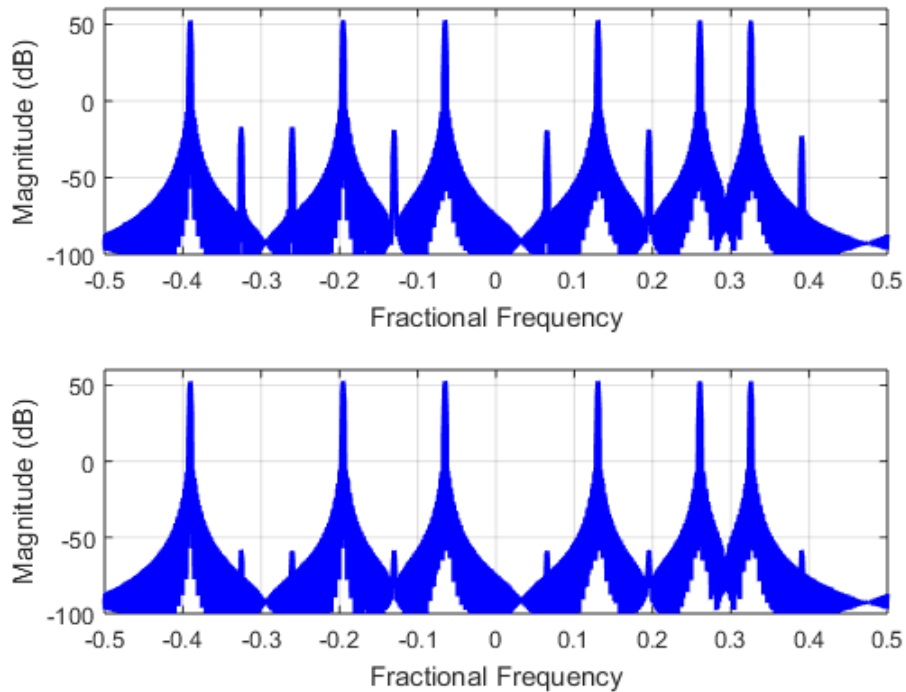


Figure 6-27. Sinusoids after 3-tap (top) and Optimal (bottom) IQI Compensators

The powers of the image components at the output of the adaptive IQIC are about 70 dB less than the powers of the sinusoids of interest, which is exactly equal to the IRR obtained (Fig. 6-26). Similarly the relative signal to image strength of all the sinusoids after optimal IQIC is around 110 dB.

The performance comparison between 1-tap and 3-tap adaptive IQI compensators in Section 6.4 showed that for the best possible results, the number of taps of the adaptive filter needs to be equal to that of the optimal filter. The filter will not be able to track the frequency selectivity if the number of taps is less. Also, having a higher number of taps than needed for the optimal case increases complexity without any additional gains.

In real-time operating scenarios, the IQI parameters are not known in advance and it is not feasible to calculate the number of taps of the optimal filter. So, it is important to have a measure that gives an idea of the number of taps required for the adaptive filter. The sinusoidal test described in this section can be used to give a key insight regarding the optimal number of taps required.

Figure 6-28 shows a new pair of I/Q imbalance filters and the aim is to estimate the optimal number of taps required with the modified IQ impairment parameters.

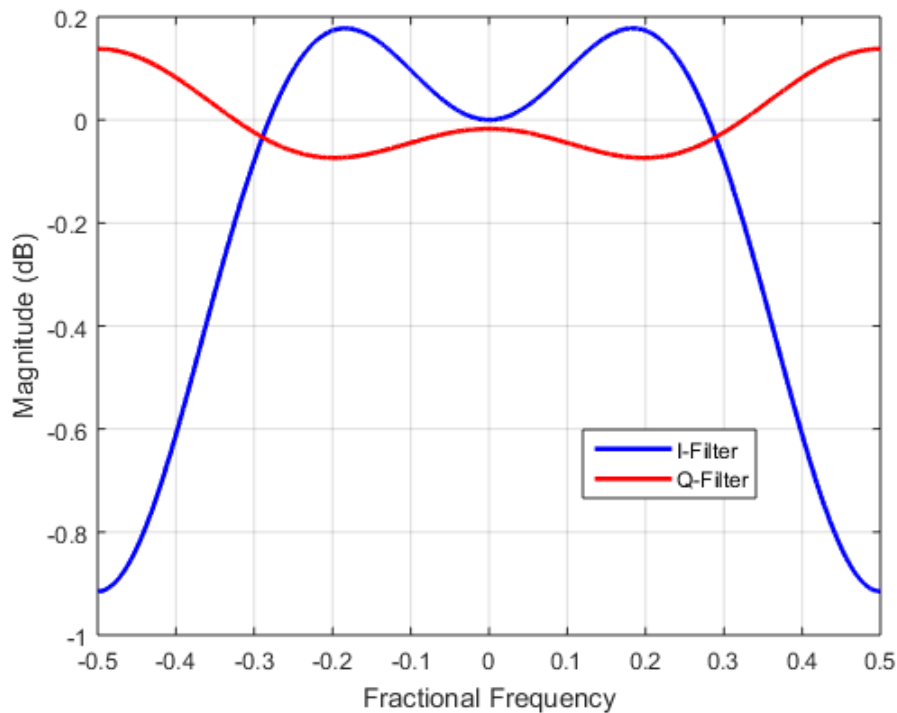


Figure 6-28. Modified IQ Imbalance Filters

$H_I(z) = 0.98 + 0.05z^{-1} - 0.03z^{-2}$ and $H_Q(z) = 1 - 0.009z^{-1} + 0.007z^{-2}$ are considered the new pair of I/Q imbalance filters (Fig. 6-28). These filters have extra ripple (trying to replicate the passband of Chebyshev filters) compared to the earlier (Fig. 6-1) ones which closely represented the passband of Butterworth filters.

The unit impulse response and poles and zeros of the optimal filter corresponding to the modified I/Q imbalance filters are shown in Fig. 6-29.

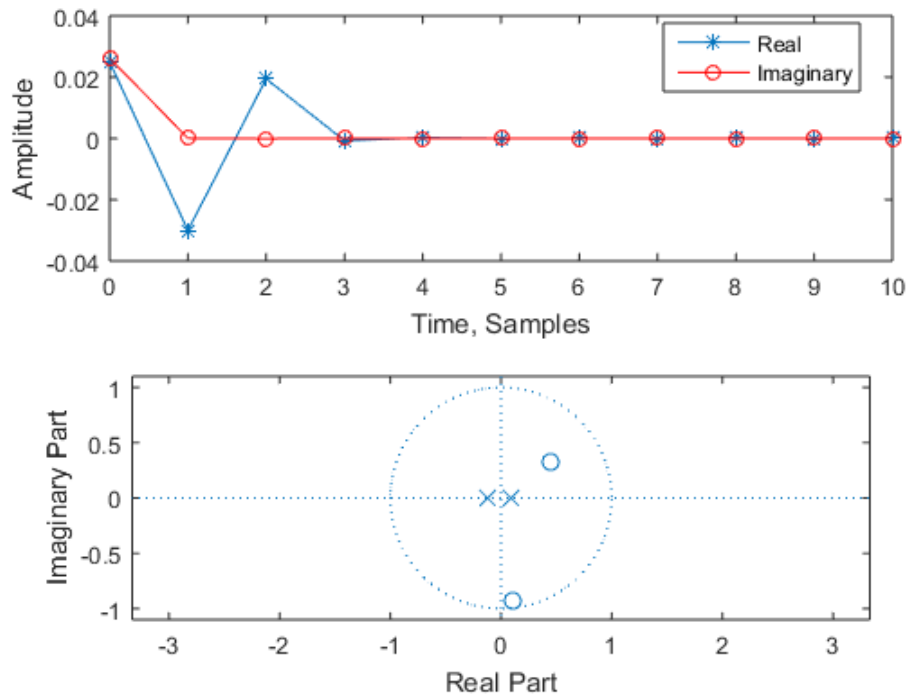


Figure 6-29. Unit Impulse Response and Pole-Zero Plot of Optimal Filter

From Fig. 6-29, it can be observed that the unit pulse response of the new optimal filter has five visibly non-zero coefficients. So, the best possible performance from the adaptive filter will be obtained by having five taps. A procedure for estimating this optimal number in practice is described below.

With a sinusoidal input that contains frequency components which cover the entire Nyquist range, the adaptive filter approaches the optimal filter behavior when it has the number of taps exactly equal to the number of taps in the optimal filter. So, one can observe almost equal suppression of image components from all the sinusoids only when the number of taps in the adaptive filter is at least equal to that of the optimal filter.

The sinusoidal input shown in Fig. 6-25 is fed to the adaptive IQIC and its output is observed for the behavior of almost equal image suppression by increasing the number of taps starting from one. Figure 6-30 shows the image strengths at the output of the adaptive IQI compensator for the number of taps varying from one to six.

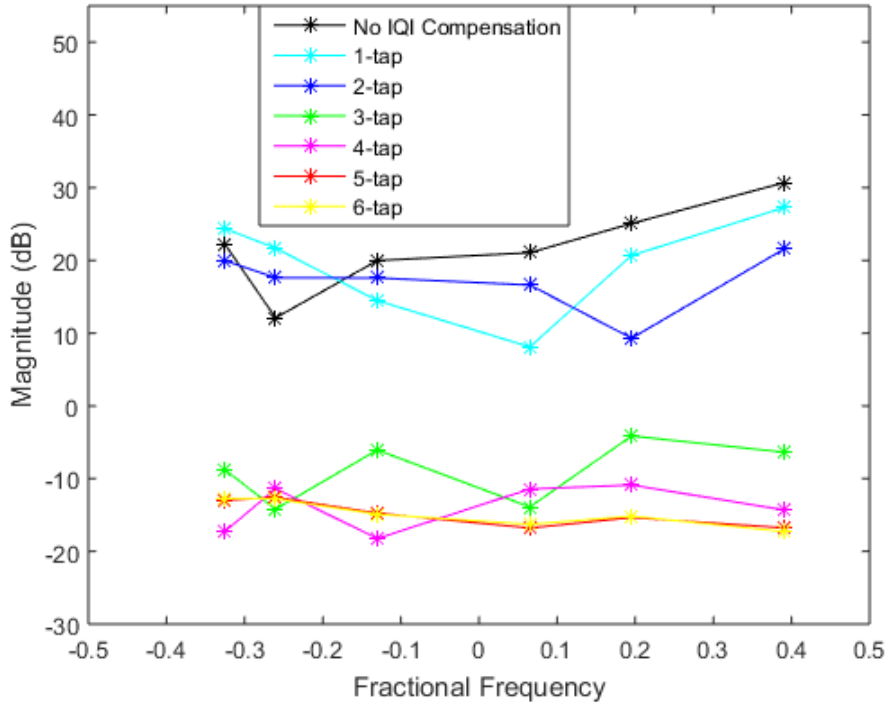


Figure 6-30. Image Strength Variations with Increase in Number of Taps

It can be observed from Fig. 6-30 that 5-tap and 6-tap adaptive filters produce almost equal image suppression across all sinusoids. The sum of absolute values of the difference of consecutive image strengths can be used as a quantitative IRR flatness metric, measuring the extent of flatness of IRR, and is defined below.

$$F = \sum_{k=1}^{N-1} |I_k - I_{k+1}| \quad (6.5)$$

where I_k is the strength of the k^{th} sinusoid, and N is the total number of sinusoids.

For a perfectly flat output, the value of the IRR flatness metric would be zero. However, the output of the IQI compensator is not perfectly flat even in the case of the optimal filter because of the distortion component discussed in Section 6.6.

Table 6-3 shows the values of the IRR flatness metric for the number of taps varying from one to six.

Table 6-3. IRR Flatness Metric vs Number of Taps

Number of Taps	IRR flatness Metric (F)
0	28.7700
1	35.4340
2	22.9480
3	33.4190
4	23.5400
5	7.4700
6	7.2300

In Table 6-3, IQI compensators with a 5-tap adaptive and 6-tap adaptive filter have lower values for the defined metric which is in agreement with the flatness curves in Fig. 6-30. The average image suppression achieved across all the image components for a different number of taps is an equally important measure to decide on the optimal number of taps. The values of average IRR for various number of taps is shown in Fig. 6-31.

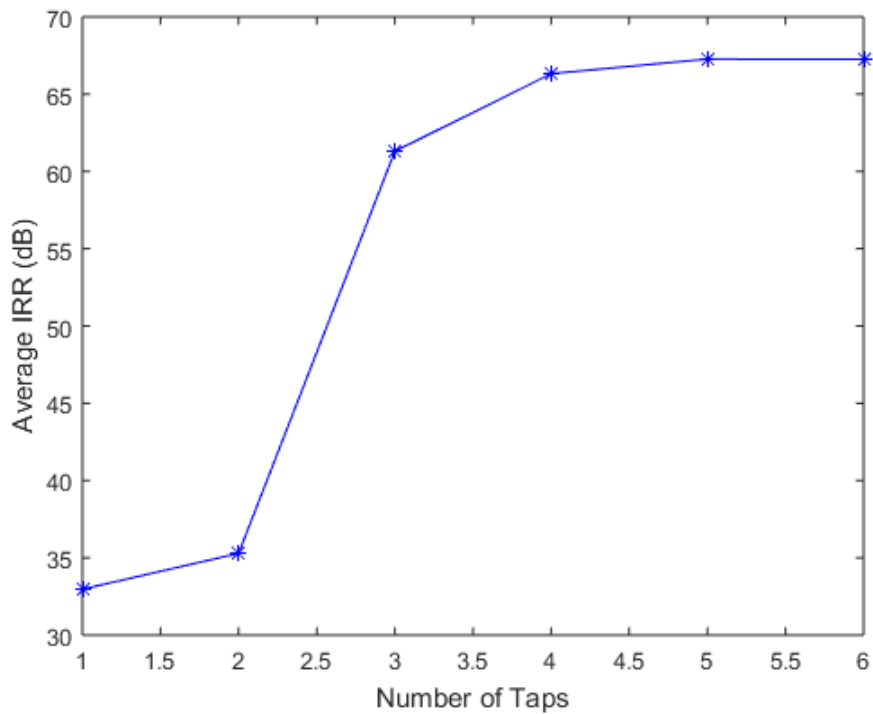


Figure 6-31. Average IRR vs Number of Taps

From Fig. 6-31, it can be observed that 5-tap and 6-tap adaptive filters give the best image suppression. The performance with 5-tap and 6-tap adaptive IQIC filters is similar in terms of flatness and amount of image suppression. It can be observed that using more than five taps does not bring any additional benefit and instead adds complexity, so we can conclude that five is the optimal number of taps required which is equal to the number of significant coefficients in the unit pulse response of the optimal filter. The unit pulse response is obtained by using the knowledge of the I/Q impairments that were introduced (Fig. 6-28).

$H_I(z) = 0.98 + 0.09z^{-1} - 0.007z^{-2} + 0.005z^{-3}$ and $H_Q(z) = 1 - 0.07z^{-1} + 0.009z^{-2} - 0.007z^{-3}$ are considered for the I/Q filter imbalances along with a gain imbalance of 3% and a phase imbalance of 3° to quantify the impact of the number of adaptive filter taps on SER performance. With these impairments the optimal IIR filter has five significant coefficients. By using the 16-QAM signal shown in Fig. 6-3 for 3-tap and 5-tap adaptive IQI compensators the SER performance is as shown in Fig. 6-32.

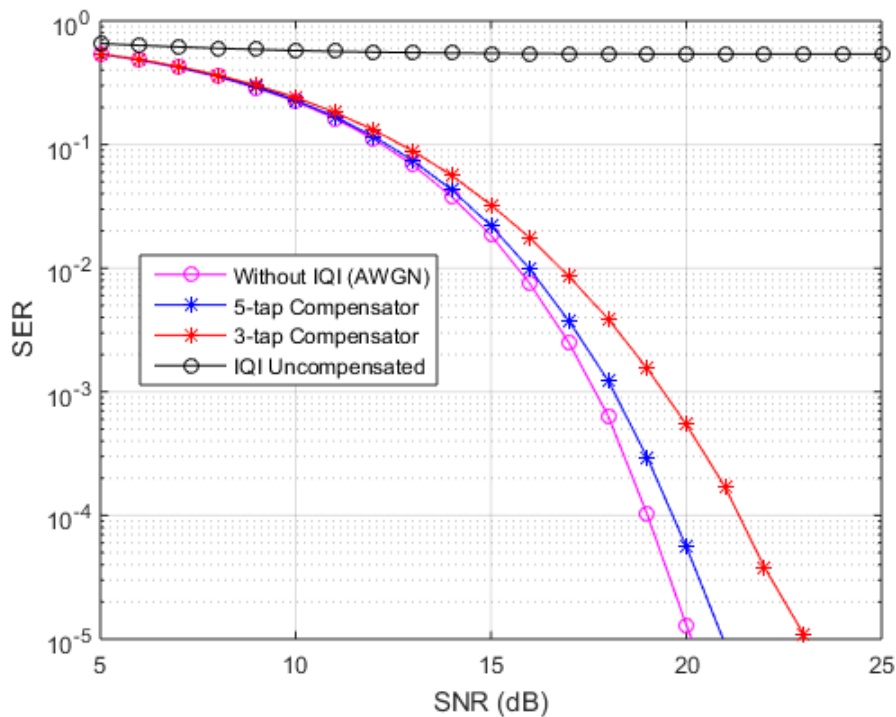


Figure 6-32. 16-QAM SER with 3-tap and 5-tap Adaptive IQI Compensators

Figure 6-32 shows an SER performance comparison for 3-tap and 5-tap adaptive IQI compensators with distortion compensation. As expected, the IQI compensator with the optimal number of taps, i.e. the 5-tap adaptive IQIC performed better than its 3-tap counterpart, which can also be correlated to the better IRR values obtained in the case of the 5-tap IQIC (Fig. 6-33).

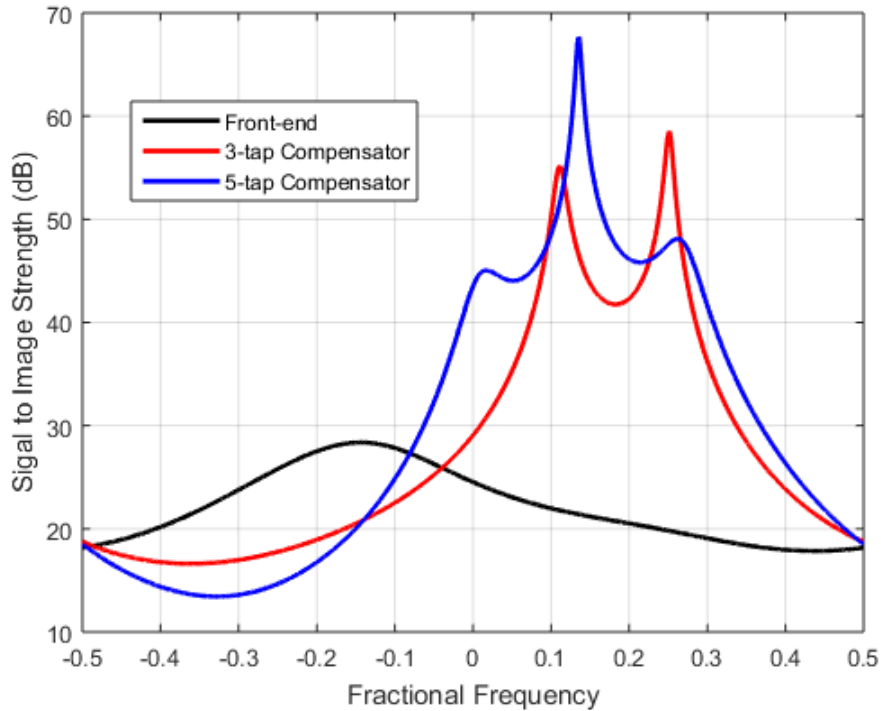


Figure 6-33. IRR after 3-tap and 5-tap Adaptive IQI Compensators

The 5-tap IQI compensator provides higher values of IRR over a broader range by effectively covering the band edges, which enables it to perform better for higher order modulation schemes. So, it can be imagined that the difference between SER performance of 5-tap and 3-tap IQI compensators increases for higher order modulation schemes like 64-QAM.

6.11 Illustration using Impulse Invariant Filter Models

The claim that the optimal number of taps leads to the best possible performance is further validated in Matlab with practical filter models. The impulse invariant method is used to create discrete versions of 5th order analog I/Q Butterworth filters that are reasonably free of aliasing effects. As illustrated in Fig. 6-34, this is accomplished by producing an input signal at twice the intended rate, passing that through the discrete I/Q imbalance filters and then low-pass filter with a sharp cutoff linear phase digital FIR filter before down-sampling to the intended rate. The latter signal is now the input to the adaptive IQI compensator.

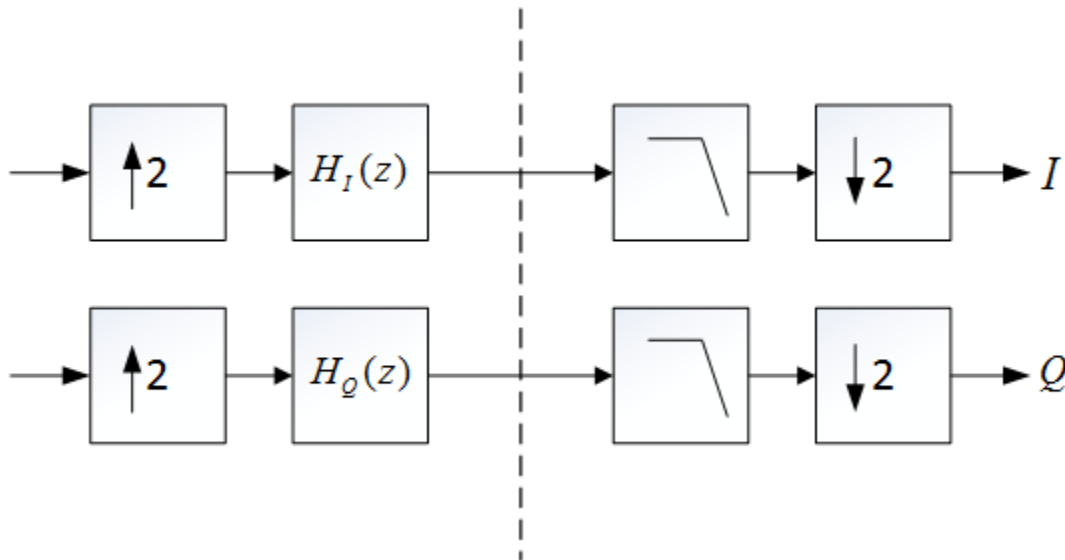


Figure 6-34. I/Q Imbalance Filters Using Impulse Invariant Method

In Fig. 6-34, $H_I(z)$ and $H_Q(z)$ present I/Q imbalance filters derived through Impulse Invariant Method. Considering identical Butterworth filters corresponds to frequency independent IQI and a 1-tap adaptive compensator is sufficient; the image rejection provided is around 65 dB (Fig. 6-35).

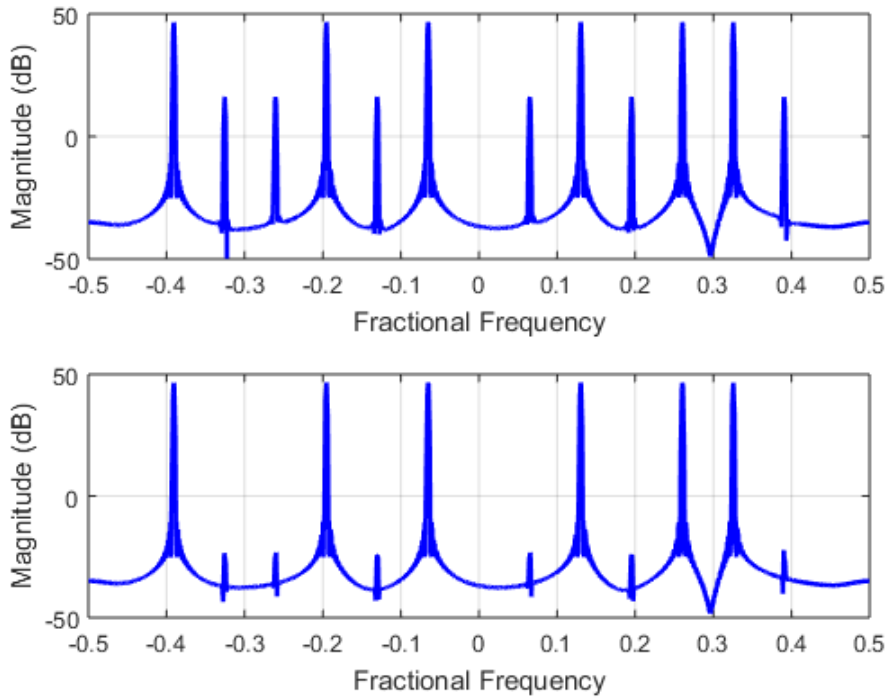


Figure 6-35. Sinusoids after IQI (top) and after 1-tap FI IQI Compensator (bottom)

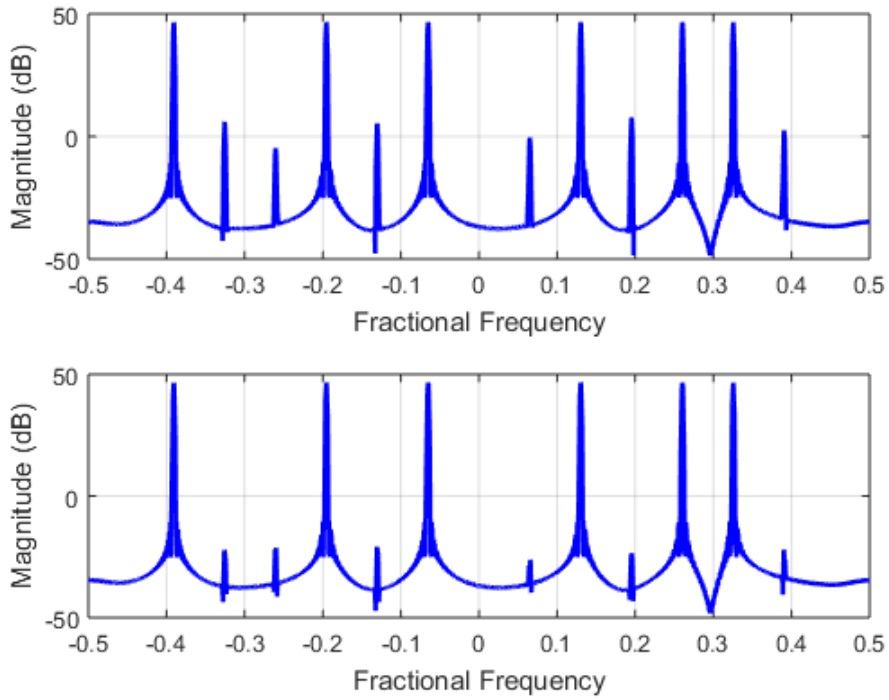


Figure 6-36. Sinusoids after 3-tap (top) and after 6-tap FD IQI Compensators (bottom)

By introducing a change of 0.15% in the cut off frequency of the Q-path lowpass filter with respect to the I-path filter, image suppression of around 65 dB for all the sinusoids (Fig. 6-36) is achieved only with the adaptive filter having six taps or more.

In the earlier experiment, the IRR values are evaluated only at the fractional frequencies where the images of the input sinusoidal signal are present. However, it will be interesting to observe the image rejection achieved across the Nyquist range of interest by using the filter coefficients obtained with an input signal having six equally spaced sinusoids, not centered at DC (so that their images fall in between input sinusoids). The red color vertical lines in Fig. 6-37 show the fractional frequencies of the images formed from input sinusoids due to IQI. 6-tap adaptive filter coefficients are obtained by adapting on this IQI impaired signal and the corresponding IRR values achieved across the Nyquist range are shown in red as well. The blue vertical lines and blue IRR show the image frequencies and result of a similar experiment in which the input sinusoids are the mirror images (flipped) of the sinusoids present in the original input (red).

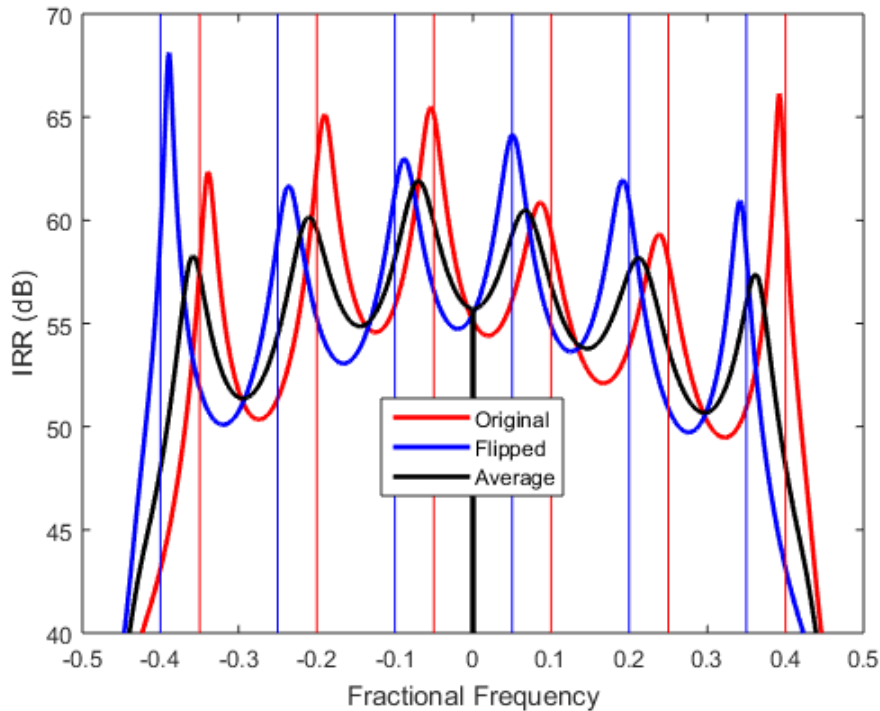


Figure 6-37. IRR Values with Adaptation on 6-Sinusoidal Input

The image rejection depicted in black in Fig. 6-37 is with the averaged filter coefficients obtained in the “red” and “blue” cases.

From Fig. 6-37, it can be observed that in the red and blue cases, the adaptive IQIC maximizes the IRR values around the frequencies where the images are present and results in relatively lower values at other frequencies. However with averaged filter coefficients (black), the performance is better in terms of approaching a maximization of the minimum IRR achieved, this can be attributed to the fact that the averaged filter coefficients cause the peaks to be less but also the valleys to be higher. The peaks of the “red” case pull up the valleys of the “blue” case and vice versa, resulting in improved IRR performance at the image frequencies where the original and flipped cases did not contribute to the error signal used for adaptation.

In Fig. 6-37, the IRR values at fractional frequencies ranging from about -0.4 to 0.4 are usually of interest in wideband receivers, as this range constitutes 80% of the Nyquist range. At DC, the IRR value is zero dB because the signal and its image lie at the same fractional frequency of zero, so that their measurement cannot be distinguished.

Till now, the impulse invariant model simulations are analyzed for the image rejection, however as discussed in Section 6.6 the IQI compensator introduces distortion on top of the signal of interest. Magnitude and phase responses of the IQI compensator thereby quantifies the magnitude and phase distortion on the signal interest.

Figure 6-38 shows the magnitude response of IQI compensators. Figure 6-39 shows the zoomed version of the magnitude response which clearly depicts the differences in the distortions caused by the different sets of adapted coefficients realized based on the input signal to the compensator.

Similarly, Figs. 6-40 and 6-41 show the phase response and zoomed version of the phase response of the IQI compensators.

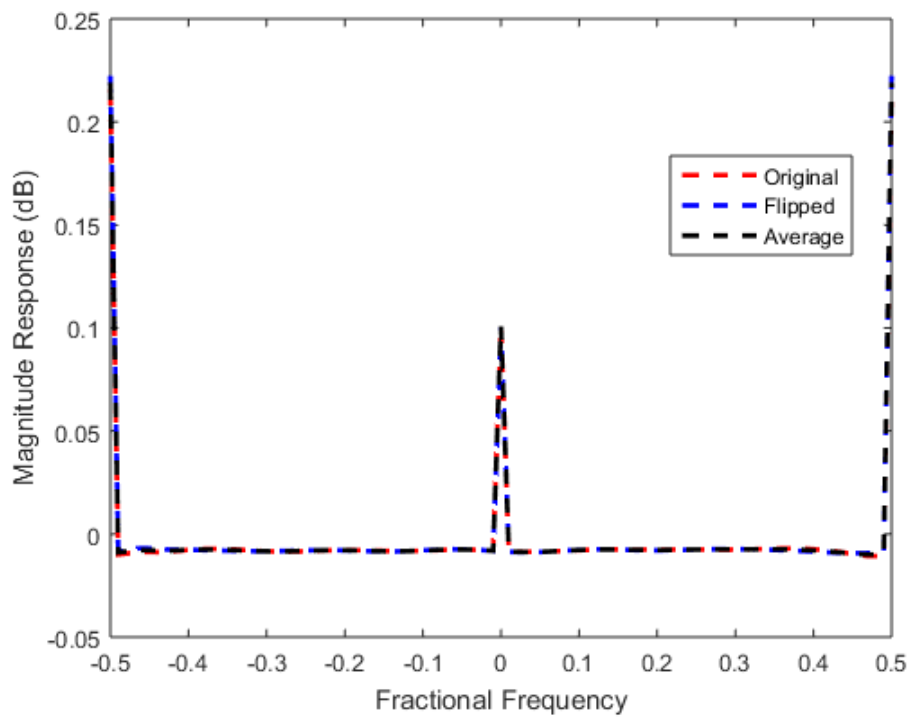


Figure 6-38. Magnitude Response of IQI Compensator

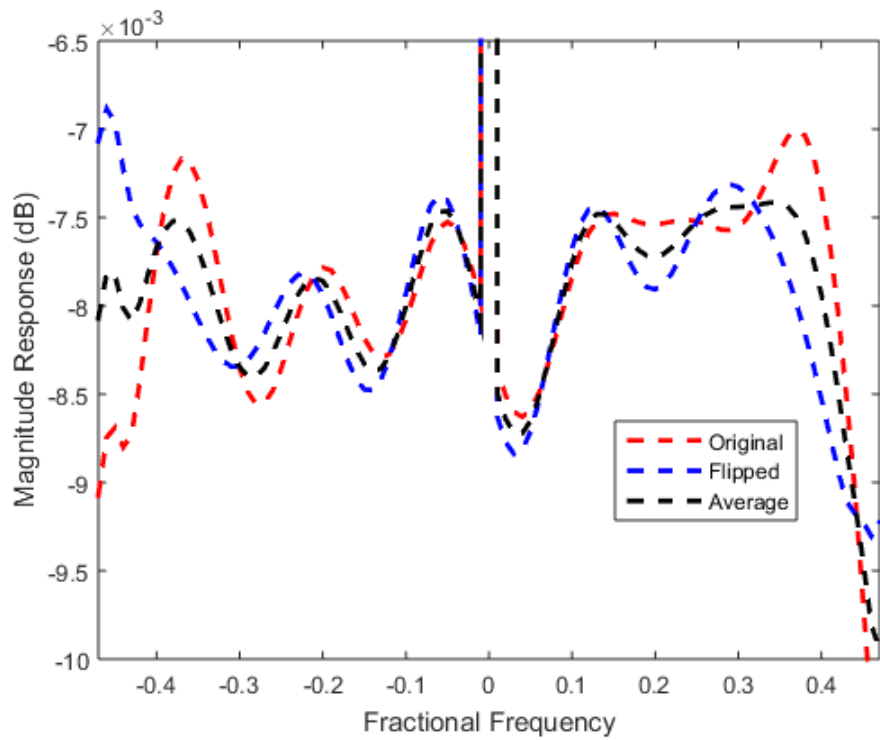


Figure 6-39. Zoomed Magnitude Response of IQI Compensator

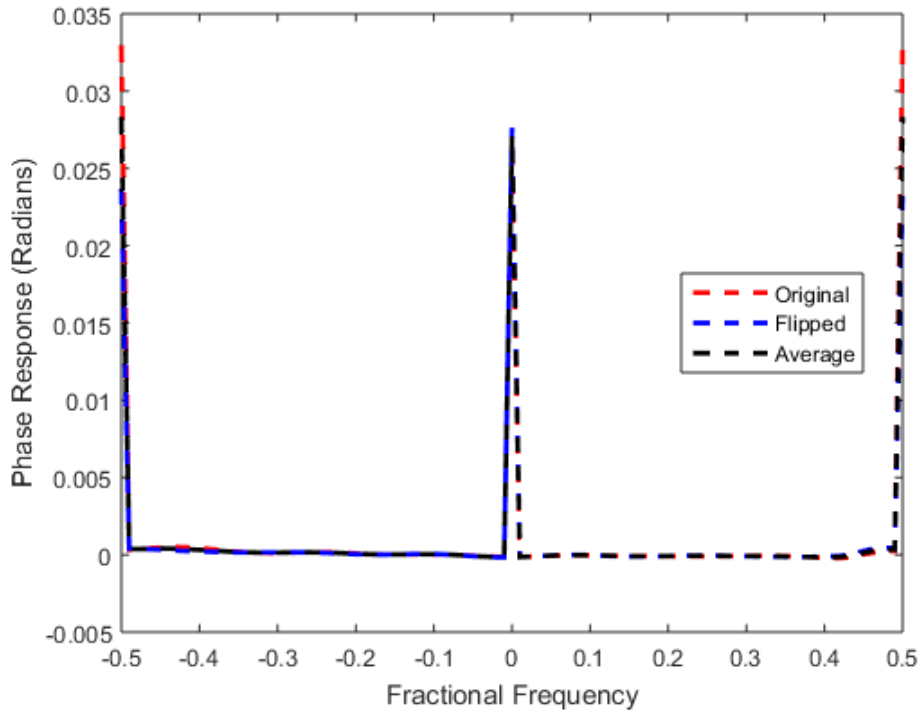


Figure 6-40. Phase Response of IQI Compensator

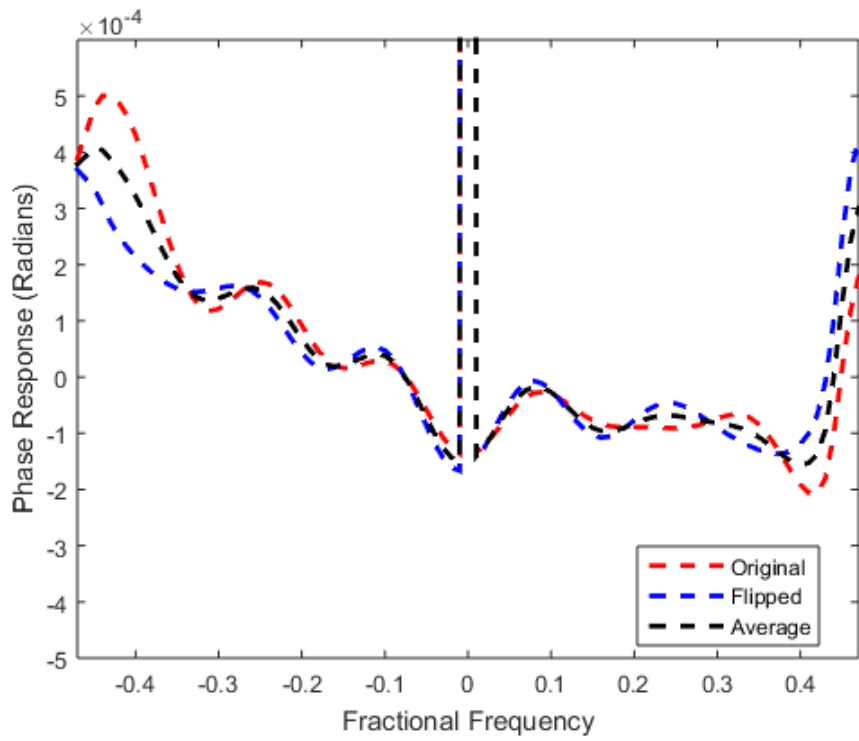


Figure 6-41. Zoomed Phase Response of IQI Compensator

It can be observed from Figures 6-39 through 6-41 that the distortions introduced are minimal for practical IQ imbalance values.

In addition to the distortion introduced by the IQI compensators, the non-linear phase of the I/Q analog lowpass filters also distorts the signal. So, it is interesting to quantify the overall magnitude and phase response of the system including mixers, filters, and IQI compensator.

Figure 6-42 shows the magnitude response of the entire impulse invariant model including the IQI compensator.

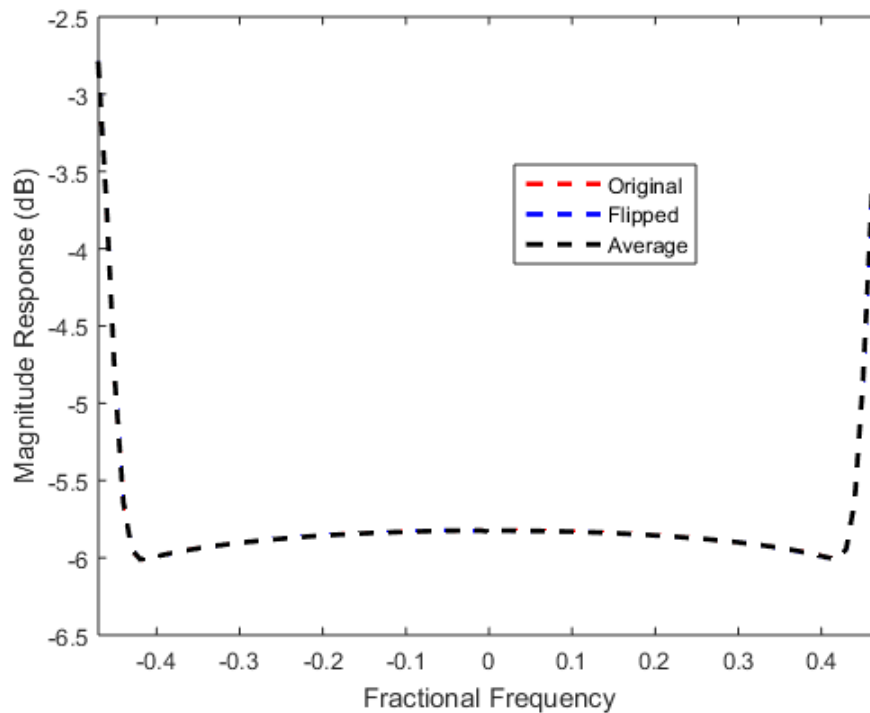


Figure 6-42. Magnitude Response of Impulse Invariant System

Figure 6-43 shows the zoomed version of the magnitude response of the entire system, highlighting the region of interest.

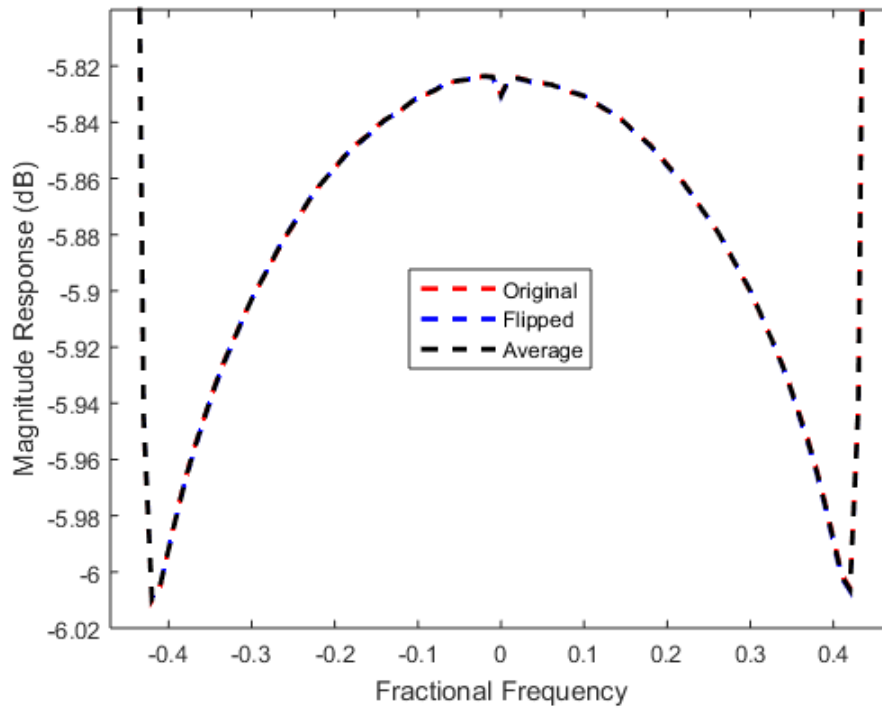


Figure 6-43. Zoomed Magnitude Response of Impulse Invariant System

The relatively flat magnitude response (Fig. 6-43) over the region of interest represents the monotone pass band behavior of the Butterworth I/Q filters.

Figure 6-44 shows the phase response of the entire system.

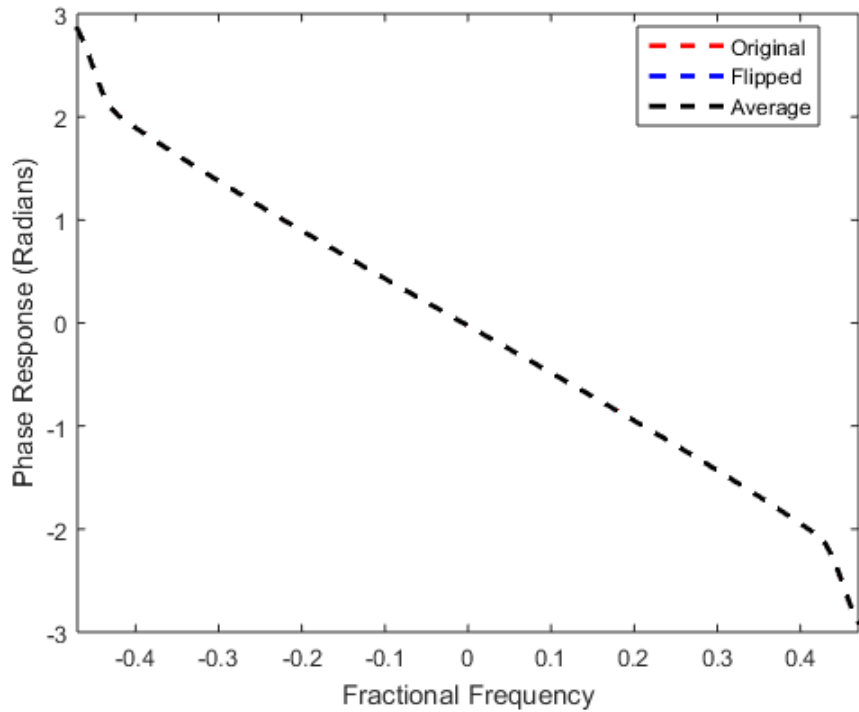


Figure 6-44. Phase Response of Impulse Invariant System

The mostly linear phase seen in Fig. 6-44 can be correlated to the passband phase of the Butterworth I/Q lowpass filters used in the model.

In summary, in this chapter the performance analysis of the various aspects of the introduced IQI estimation and compensation technique is presented. In conclusion, it can be stated that by using the optimal number of taps depending on the impairments that are in effect, the performance of the blind-adaptive technique will be enhanced.

The summary of the results and scope of future work is presented in the next chapter.

CHAPTER 7 SUMMARY AND SCOPE OF FUTURE WORK

In this thesis, a blind-adaptive technique for addressing time-varying and frequency selective IQ Imbalance is investigated and its performance is thoroughly validated under various real-time operating scenarios. In conclusion, this technique is best suited for generic transceivers or software defined radio kind of hardware. In addition, the ability to track the time-varying IQI due to temperature and aging effects of RF hardware makes it a perfect solution for wireless transceivers operating continuously, for an extended number of hours not facilitating recalibration.

The complexity of the solution is very similar to that of the LMS algorithm, requiring a minimal number of multiplications and additions for every update cycle. As time-varying changes of IQI are very slow, the coefficient update need not be done for every sample and the update can be done at regular intervals making the process even more power efficient. A simple sinusoidal test can be used to identify the optimal number of taps required and further initializing the filter taps with the steady state values achieved with a sinusoidal test at start-up reduces the time required for initial convergence.

There is a potential scope for formulating IQI compensation algorithms that provide better image rejection and flatness across the band by exploring high order cyclic statistics and block estimation methods. Properness/Circularity properties can be used to correct dynamic DC offset. The possibility of a variable step size algorithm providing better adaptation and steady state performance is worth exploring.

REFERENCES

- [1] A. Gupta and R. K. Jha, "A Survey of 5G Network: Architecture and Emerging Technologies," *IEEE Access*, vol. 3, pp. 1206-1232, 2015.
- [2] B. Razavi, *RF microelectronics*. Upper Saddle River, NJ: Prentice Hall, 2012.
- [3] J. Thompson *et al.*, "5G wireless communication systems: prospects and challenges [Guest Editorial]," *IEEE Communications Magazine*, vol. 52, no. 2, pp. 62-64, 2014.
- [4] M. A. M. Albreem, "5G wireless communication systems: Vision and challenges," in *2015 International Conference on Computer, Communications, and Control Technology (I4CT)*, 2015, pp. 493-497.
- [5] C. H. Doan, S. Emami, A. M. Niknejad, and R. W. Brodersen, "Millimeter-wave CMOS design," *IEEE Journal of Solid-State Circuits*, vol. 40, no. 1, pp. 144-155, 2005.
- [6] T. Ulversoy, "Software Defined Radio: Challenges and Opportunities," *IEEE Communications Surveys & Tutorials*, vol. 12, no. 4, pp. 531-550, 2010.
- [7] G. Fettweis, M. Lohning, D. Petrovic, M. Windisch, P. Zillmann, and W. Rave, "Dirty RF: a new paradigm," in *2005 IEEE 16th International Symposium on Personal, Indoor and Mobile Radio Communications*, 2005, vol. 4, pp. 2347-2355 Vol. 4.
- [8] S. Mirabbasi and K. Martin, "Classical and modern receiver architectures," *IEEE Communications Magazine*, vol. 38, no. 11, pp. 132-139, 2000.
- [9] W. H. W. Tuttlebee, *Wiley Series in Software Radio Ser: Software Defined Radio: Enabling Technologies (1)*. John Wiley & Sons, Incorporated, 2003.
- [10] L. Xiaopeng and M. Ismail, "A single-chip CMOS front-end receiver architecture for multi-standard wireless applications," in *ISCAS 2001. The 2001 IEEE International Symposium on Circuits and Systems (Cat. No.01CH37196)*, 2001, vol. 4, pp. 374-377 vol. 4.
- [11] A. A. Abidi, "Direct-conversion radio transceivers for digital communications," in *Solid-State Circuits Conference, 1995. Digest of Technical Papers. 41st ISSCC, 1995 IEEE International*, 1995, pp. 186-187.
- [12] B. Razavi, "Design considerations for direct-conversion receivers," *IEEE Transactions on Circuits and Systems II: Analog and Digital Signal Processing*, vol. 44, no. 6, pp. 428-435, 1997.
- [13] M. Faulkner, "DC offset and IM2 removal in direct conversion receivers," *IEE Proceedings - Communications*, vol. 149, no. 3, pp. 179-184, 2002.
- [14] G. T. Gil, "Nondata-Aided I/Q Mismatch and DC Offset Compensation for Direct-Conversion Receivers," *IEEE Transactions on Signal Processing*, vol. 56, no. 7, pp. 2662-2668, 2008.
- [15] P. Cruz, H. Gomes, and N. Carvalho, *Receiver Front-End Architectures - Analysis and Evaluation*. INTECH Open Access Publisher, 2010.

- [16] L. Smaini and I. Books24x, *RF analog impairments modeling for communication systems simulation: application to OFDM-based transceivers*. Chichester, West Sussex, United Kingdom: Wiley, 2012.
- [17] R. Svitek and S. Raman, "DC offsets in direct-conversion receivers: characterization and implications," *IEEE Microwave Magazine*, vol. 6, no. 3, pp. 76-86, 2005.
- [18] D. M. Akos, M. Stockmaster, J. B. Y. Tsui, and J. Caschera, "Direct bandpass sampling of multiple distinct RF signals," *IEEE Transactions on Communications*, vol. 47, no. 7, pp. 983-988, 1999.
- [19] B. Junghwa and P. Jinwoo, "An efficient algorithm for bandpass sampling of multiple RF signals," *IEEE Signal Processing Letters*, vol. 13, no. 4, pp. 193-196, 2006.
- [20] L. Kull *et al.*, "22.1 A 90GS/s 64x; interleaved SAR ADC in 32nm digital SOI CMOS," in *2014 IEEE International Solid-State Circuits Conference Digest of Technical Papers (ISSCC)*, 2014, pp. 378-379.
- [21] M. Valkama, "Advanced IQ signal processing for wideband receivers: Models and algorithms," *Tampereen teknillinen yliopisto. Julkaisu-Tampere University of Technology. Publication; 350*, 2001.
- [22] M. Windisch, *Estimation and Compensation of IQ Imbalance in Broadband Communications Receivers*. Vogt, 2007.
- [23] L. Anttila, M. Valkama, and M. Renfors, "Blind Compensation of Frequency-Selective I/Q Imbalances in Quadrature Radio Receivers: Circularity -Based Approach," in *2007 IEEE International Conference on Acoustics, Speech and Signal Processing - ICASSP '07*, 2007, vol. 3, pp. III-245-III-248.
- [24] L. Anttila, M. Valkama, and M. Renfors, "Circularity-Based I/Q Imbalance Compensation in Wideband Direct-Conversion Receivers," *IEEE Transactions on Vehicular Technology*, vol. 57, no. 4, pp. 2099-2113, 2008.
- [25] A. M. Schoonen, P. Baltus, J. van Sinderen, and R. van Veldhoven, *Estimation Methods for IQ Imbalance in Multi-Standard (Near) Zero IF Receivers*.
- [26] J. Liu *et al.*, "OFDM-MIMO WLAN AP front-end gain and phase mismatch calibration," in *Proceedings. 2004 IEEE Radio and Wireless Conference (IEEE Cat. No.04TH8746)*, 2004, pp. 151-154.
- [27] K. Maeda, W. Hioe, Y. Kimura, and S. Tanaka, "Wideband Image-Rejection Circuit for Low-IF Receivers," in *2006 IEEE International Solid State Circuits Conference - Digest of Technical Papers*, 2006, pp. 1912-1921.
- [28] A. Tarighat, R. Bagheri, and A. H. Sayed, "Compensation schemes and performance analysis of IQ imbalances in OFDM receivers," *IEEE Transactions on Signal Processing*, vol. 53, no. 8, pp. 3257-3268, 2005.
- [29] J. H. Deng and K. T. Feng, "Time-frequency multiplex estimator design of joint Tx IQ imbalance, CFO, channel estimation, and compensation for OFDM systems," in *2015 38th International Conference on Telecommunications and Signal Processing (TSP)*, 2015, pp. 1-5.
- [30] I. Elahi, K. Muhammad, and P. T. Balsara, "I/Q mismatch compensation using adaptive decorrelation in a low-IF receiver in 90-nm CMOS process," *IEEE Journal of Solid-State Circuits*, vol. 41, no. 2, pp. 395-404, 2006.

- [31] L. Anttila, "Digital front-end signal processing with widely-linear signal models in radio devices," *PhD, Tampere University of Technology, Department of Communications Engineering*, 2011.
- [32] B. Picinbono and P. Bondon, "Second-order statistics of complex signals," *IEEE Transactions on Signal Processing*, vol. 45, no. 2, pp. 411-420, 1997.
- [33] H. Stark and J. W. Woods, *Probability and Random Processes with Applications to Signal Processing*. Prentice Hall, 2002.
- [34] B. Picinbono, "On circularity," *IEEE Transactions on Signal Processing*, vol. 42, no. 12, pp. 3473-3482, 1994.
- [35] E. A. Lee and D. G. Messerschmitt, *Digital communication*. Boston: Kluwer Academic Publishers, 1994.
- [36] P. J. Schreier and L. L. Scharf, "Second-order analysis of improper complex random vectors and processes," *IEEE Transactions on Signal Processing*, vol. 51, no. 3, pp. 714-725, 2003.
- [37] T. Adali, P. J. Schreier, and L. L. Scharf, "Complex-Valued Signal Processing: The Proper Way to Deal With Impropriety," *IEEE Transactions on Signal Processing*, vol. 59, no. 11, pp. 5101-5125, 2011.
- [38] L. Anttila and M. Valkama, "On Circularity of Receiver Front-end Signals Under RF Impairments," in *17th European Wireless 2011 - Sustainable Wireless Technologies*, 2011, pp. 1-8.
- [39] W. Brown and R. Crane, "Conjugate linear filtering," *IEEE Transactions on Information Theory*, vol. 15, no. 4, pp. 462-465, 1969.
- [40] B. Picinbono and P. Chevalier, "Widely linear estimation with complex data," *IEEE Transactions on Signal Processing*, vol. 43, no. 8, pp. 2030-2033, 1995.
- [41] P. J. Schreier and L. L. Scharf, *Statistical Signal Processing of Complex-Valued Data: The Theory of Improper and Noncircular Signals*. Cambridge University Press, 2010.
- [42] J. Tubbax *et al.*, "Compensation of IQ imbalance and phase noise in OFDM systems," *IEEE Transactions on Wireless Communications*, vol. 4, no. 3, pp. 872-877, 2005.
- [43] R. Harris, D. Chabries, and F. Bishop, "A variable step (VS) adaptive filter algorithm," *IEEE Transactions on Acoustics, Speech, and Signal Processing*, vol. 34, no. 2, pp. 309-316, 1986.
- [44] D. Bismor, K. Czyz, and Z. Ogonowski, "Review and comparison of variable step-size LMS algorithms," *International Journal of Acoustics and Vibration*, vol. 21, no. 1, pp. 24-39, 2016.
- [45] L. Zhang, J. Zhou, Z. Yu, X. Zhou, and R. Zhang, "Design of the high-performance RF transmitter for IEEE 802.11ac system," in *2016 IEEE International Conference on Ubiquitous Wireless Broadband (ICUWB)*, 2016, pp. 1-3.